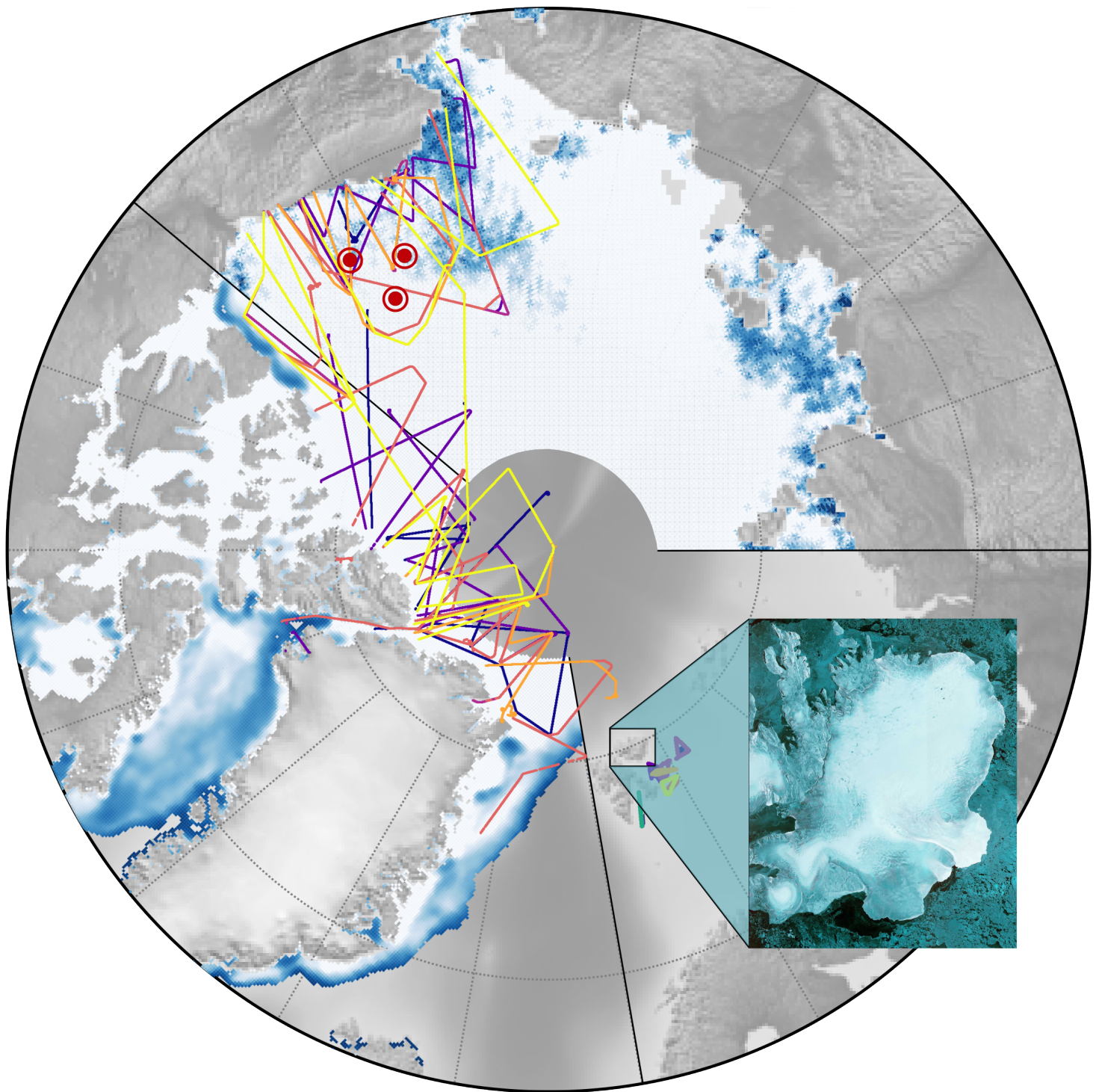


Faculty of Science and Technology
Department of Physics and Technology

Thin Sea Ice Detection with CryoSat-2

Trym Fjeldstad Varland
FYS-3931 Master's Thesis in Space Physics, 30 SP
May 2025



The cover figure displays sea ice thickness from the SMOS AWI product (left) and the CryoSat UiT product (top). Also shown are the flight paths of NASA's OIB mission and the SMOSice campaign, along with the locations of the BGEP moorings. The zoomed-in section presents a SAR image of the Austfonna Ice Cap in Svalbard, captured by the ICEYE satellite constellation.

Abstract

Arctic sea ice plays a vital role in the climate system, influencing atmospheric circulation, oceanic processes, and Arctic ecosystems. Thin sea ice is particularly important, as it governs seasonal transitions and contributes to feedback mechanisms such as Arctic amplification. Reliable estimates of sea ice thickness (SIT), especially within the thin ice regimes (less than 1 m), are essential for improving forecasting systems and reducing associated biases. This thesis investigates the performance of altimetry-based SIT retrievals from CryoSat-2 below 1 m, with a focus on the performance of the CryoSat-2 UiT product created by the Earth Observation Group at UiT. That incorporates a physical retracking algorithm known as LARM and a snow accumulation model called SnowModel-LG. The analysis includes an intercomparison with established CryoSat-2 SIT products from AWI, CPOM, and a Warren 1999 climatology configuration with LARM, using the Soil Moisture and Ocean Salinity (SMOS) AWI product as reference. The intercomparison highlights the influence of waveform retracking methods and snow climatology inputs, with the UiT product demonstrating the closest alignment with the SMOS AWI product. Validation against independent measurement from Operation IceBridge, the BGEP moorings, and the SMOSice campaign confirms that the UiT product provides reliable SIT estimates down to approximately 0.4-0.5 m. SMOS, in contrast, captures thin ice more consistently below 0.4 m but tends to saturate at thicknesses above approximately 0.5 m. These findings support the inclusion of CryoSat-2 thin-ice returns in data assimilation and the floe classification algorithm to improve model accuracy and enhance sea ice monitoring. The results also highlight the value of a complementary approach, where SMOS data is suited for early freeze-up periods and marginal ice zones, while CryoSat-2 products are preferred in thicker or mixed ice regimes. A tentative lower threshold of approximately 0.4 m is proposed for standalone use of CryoSat-2 data, guiding future data assimilation methods in sea ice forecasting.

Acknowledgements

First and foremost, I would like to express my sincere gratitude to my supervisor, Jack Christopher Landy, for his unwavering support and guidance throughout this thesis. From the very beginning of the project, you welcomed me with open arms. Your patience, insight, and expertise have been truly invaluable, and without your mentorship, this work would not have been possible.

The sea ice thickness product, developed using the Lognormal Altimeter Retracking Model (LARM) and the Lagrangian snow-evolution model (SnowModel-LG), was kindly provided by the Earth Observation Group at UiT – The Arctic University of Norway.

I would also like to acknowledge the institutions and data providers that made this research possible: The Alfred Wegener Institute for Polar and Marine Research and the German Society of Polar Research for the SMOS sea ice thickness product (AWI), available at <https://www.meereisportal.de> (funding: REKLIM-2013-04). The Centre for Polar Observation and Modelling (CPOM) for the CryoSat-2 sea ice thickness dataset. The National Aeronautics and Space Administration (NASA) for providing the Operation IceBridge (OIB) airborne sea ice thickness data. Woods Hole Oceanographic Institution for the Beaufort Gyre Exploration Project, upward-looking sonar mooring data. The European Space Agency (ESA) for data from the SMOSice campaign.

I extend heartfelt thanks to the people who have supported me during my thesis and academic journey. To my partner, Frid Festø; thank you for your endless patience, love, and encouragement, whether I was building rockets or writing this thesis. To my fellow master's students, Håkon Silseth and Truls Larsen; thank you for five years of hard classes, great discussions, and even better memories. To my Family, Belinda, Hans, and Sindre; thank you for your support, including when I suddenly decided to move to Tromsø. I have always cherished our conversations, from cars and motorbikes to music.

Finally, I would like to acknowledge the use of ChatGPT, which assisted with grammar refinement, helping to make the text more fluid and natural. Its use was conducted responsibly and transparently.

List of Figures

2.1	passive and active remote sensing	6
2.2	The electromagnetic spectrum	7
2.3	SAR image geometry	9
2.4	Main scattering mechanisms	10
2.5	Complex SAR image components	11
2.6	MW emission modeling	13
2.7	SMOS modeled TB with corresponding SIT	14
2.8	Principle of satellite altimetry	15
2.9	Beam-limited and pulse-limited altimetry	17
2.10	Returned altimetry waveform	18
2.11	Principle of SAR altimetry	19
2.12	Arctic sea ice photo	20
2.13	Key components of sea ice monitoring	22
2.14	SAR sea ice image	23
3.1	CryoSat-2 in orbit	28
3.2	Operational Geographical Mode Mask for SIRAL	30
3.3	SMOS in orbit	31
3.4	OIB mission flight paths	35
3.5	BGEP mooring locations	36
3.6	HEM and ALS flight paths	37
4.1	OIB observation sea ice thickness histogram	45
4.2	Sea ice draft histogram at BGEP mooring A	46
5.1	HEM and ALS SIT distribution	55
6.1	Product comparison map SIT difference	58
6.2	Product comparison bar and distribution figure	59
6.3	Product comparison SIT difference heat map	60
6.4	Product comparison of SIT estimates using box scatter plot .	61

6.5	OIB validation bar and distribution plot	63
6.6	OIB validation box scatter figure	64
6.7	BGEP validation bar and distribution plot	65
6.8	BGEP validation time series	66
6.9	BGEP validation raw and seasonal anomalies pair scatter plot	68
6.10	SMOSice validation map of HEM tSIT estimates	70
6.11	SMOSice validation HEM tSIT distribution	71
6.12	SMOSice validation comparison of ALS tFB and UiT tFB	72
6.13	SMOSice validation images from the ALS flight on 26 March	73
6.14	SMOSice validation comparison of ALS SIT and SMOS SIT	74
6.15	SMOSice validation images from the ALS flight on 24 March	74
A.1	Monthly product comparison bar and distribution figure	97
A.2	Monthly product comparison of SIT estimates using box scatter plot	98
A.3	Monthly product comparison SIT difference heat map	98
A.4	OIB validation bar and distribution plot without filtering	100
A.5	BGEP validation bar and distribution plot without filtering	102
A.6	BGEP validation raw SID pair scatter plot at mooring locations	103
A.7	BGEP validation SID seasonal anomalies pair scatter plot at mooring locations	103
A.8	SMOSice validation map of raw HEM tSIT estimates	104
A.9	SMOSice validation of raw HEM tSIT distribution	105

List of Tables

6.1	Statistical product comparison metrics	62
6.2	Statistical OIB validation metrics	64
6.3	Statistical BGEP validation metrics	69
6.4	Statistical SMOSice HEM tSIT validation metrics	71
6.5	Statistical SMOSice ALS tFB validation metric	73
6.6	Statistical SMOSice ALS SIT validation metric	75
A.1	Monthly statistical CryoSat products comparison metrics . . .	99
A.2	Full statistical OIB validation metrics	101
A.3	Full statistical BGEP validation metrics	104
A.4	Full statistical SMOSice HEM tsIT validation metrics	105
A.5	Full statistical SMOSice ALS tFB validation metrics	106

Contents

Abstract	iii
Acknowledgements	v
List of Figures	vii
List of Tables	ix
List of acronyms	xvi
1 Introduction	1
1.0.1 Structure of Thesis	3
2 Background	5
2.1 Basics of Remote Sensing	5
2.1.1 Electromagnetic Radiation	6
2.1.2 Radar	7
2.1.3 Resolutions	8
2.2 Synthetic Aperture Radar (SAR)	8
2.2.1 SAR Theory	9
2.3 Passive Microwave Sensing	11
2.3.1 Basic Passive Microwave Theory	12
2.3.2 Real-World Applications	12
2.4 Altimetry	14
2.4.1 Radar Altimetry	15
2.4.2 Laser Altimetry	18
2.4.3 SAR Altimetry	19
2.5 Sea Ice Monitoring	20
2.5.1 Sea Ice Theory	21
2.5.2 Techniques of Monitoring Sea Ice	21
2.5.3 Sea Ice Thickness Estimation	23

2.5.4 Data Assimilation	24
2.6 Previous work	25
3 Satellites & Campaigns	27
3.1 CryoSat-2	28
3.1.1 SIRAL	29
3.1.2 Processing Levels	30
3.2 SMOS	31
3.2.1 MIRAS	32
3.3 Operation IceBridge	34
3.4 Beaufort Gyre Exploration Project	35
3.5 SMOSice Campaign	36
4 Data sets & Processing	39
4.1 Sea Ice Thickness Satellite Products	39
4.1.1 SMOS AWI Product	39
4.1.2 CryoSat-2 UiT Product	40
4.1.3 CryoSat-2 CPOM Product	42
4.1.4 CryoSat-2 AWI Product	43
4.2 Validation data sets	44
4.2.1 Operation IceBridge	44
4.2.2 Beaufort Gyre Exploration Project	45
4.2.3 SMOSice Campaign	46
5 Method	49
5.1 Resampling	49
5.2 Statistical Methods for Assessment	50
5.3 Comparison of CryoSat Products Against SMOS AWI	51
5.4 Validation Against OIB Airborne Observations	52
5.5 Validation Against BGEP Mooring Data	53
5.6 Validation Against SMOSice Campaign Measurements	54
6 Results	57
6.1 Comparison of CryoSat Products Against SMOS AWI	57
6.2 Validation Against OIB Airborne Observations	62
6.3 Validation Against BGEP Mooring Data	64
6.4 Validation Against SMOSice Campaign Measurements	69
7 Summary & Discussion	77
8 Conclusion & Future Work	83

9 Data & Code Availability	85
Bibliography	87
Appendix A: Complete Analysis Results and Supporting Data	97
A.1 Comparison of CryoSat Products Against SMOS AWI	97
A.2 Validation Against OIB Airborne Observations	100
A.3 Validation Against BGEP Mooring Data	102
A.4 Validation Against SMOSice Campaign Measurements	104

List of Acronyms

CryoSat	CryoSat-2
SMOS	Soil Moisture and Ocean Salinity
OIB	Operation IceBridge
BGEP	Beaufort Gyre Exploration Project
CPOM	Centre for Polar Observations and Modelling
AWI	Alfred Wegener Institute
SAR	Synthetic Aperture Radar
PM	Passive Microwave
EM	Electromagnetic
LARM	Lognormal Altimeter Retracker Model
SnowModel-LG	Lagrangian Snow-Evolution Model
TFMRA	Threshold First-Maximum Retracker Algorithm
FYI	First-Year Ice
MYI	Multi-Year Ice
SIT	Sea Ice Thickness
tSIT	Total Sea Ice Thickness

SID	Sea Ice Draft
SIC	Sea Ice Concentration
SD	Snow Depth
tFB	Total Freeboard
iFB	Ice Freeboard
rFB	Radar Freeboard
SSH	Sea Surface Height
ESA	European Space Agency
NASA	National Aeronautics and Space Administration

1

Introduction

Over the past two decades, sea ice in the Arctic basin has shifted from predominantly thick, old multi-year ice to thinner, younger first-year ice types (Polyak et al., 2010), driven by a rapid warming of the northern polar climate, occurring at a rate three to four times faster than the global average (Rantanen et al., 2022). Arctic sea ice serves as a sensitive indicator of climate change, and its decline impacts global weather patterns, ocean circulation, Arctic ecosystems, and heat exchange due to the ice-albedo feedback mechanism. This reduction in ice cover enhances maritime access to the Arctic Ocean, increasing opportunities and challenges for navigation in polar regions (Polyak et al., 2010). For communities in Arctic regions such as around Svalbard, sea ice thickness remains a critical factor for the safe navigation of vessels and human activities in ice-covered waters, making it a high priority for services like the Norwegian Ice Service.

One of the key indicators of changes in the sea ice cover is sea ice thickness. Due to the remote location and harsh conditions of the Arctic environment, various methods have been developed to measure sea ice thickness, including drill holes, upward-looking sonars, and airborne observations using laser and radar altimetry (Krishfield and Proshutinsky, 2006; MacGregor et al., 2021; Hendricks et al., 2015). However, these methods are generally limited to certain periods and specific regions, lacking the capability for consistent Arctic-wide

spatiotemporal coverage. This underscores the importance of satellite remote sensing, which enables comprehensive spatial and temporal monitoring with high resolution and long-term observation records. In this context, several satellite missions have been launched, including CryoSat-2, equipped with a synthetic aperture radar altimeter and operational since 2010 (Parrinello et al., 2018), and the Soil Moisture and Ocean Salinity mission, which employs passive microwave sensing, launched in 2009 (Mecklenburg et al., 2016).

Several CryoSat sea ice thickness products have been developed (e.g, Laxon et al. (2013); Kurtz et al. (2014); Tilling et al. (2018); Landy et al. (2020); Hendricks et al. (2021)). The derivation of sea ice thickness from altimetry requires assumptions related to snow loading and hydrostatic equilibrium (Giles et al., 2008), particularly in the retracking methods applied to the CryoSat waveforms. However, studies have indicated that CryoSat-derived sea ice thickness carries large uncertainties for sea ice thinner than 1 m (Ricker et al., 2017). This poses a challenge, especially as Arctic sea ice increasingly transitions toward thinner first-year ice and is more sensitive to climate change. During winter months, thin sea ice contributes a net heat flux to the atmosphere that is one to two orders of magnitude greater than that of thicker multi-year ice (Maykut, 1978). Furthermore, in data assimilation applications for model-based forecasting systems, CryoSat data below 1 m is often assigned large uncertainties (e.g, Mignac et al. (2022)). Enhancing the accuracy of these CryoSat-derived thickness estimates could therefore contribute to reducing biases and improving the prediction of future ice extent and ice edge location. An alternative approach is the use of passive microwave radiometry, such as the SMOS satellite, which has demonstrated lower uncertainties for ice thinner than 1 m. However, the uncertainty increases exponentially beyond approximately 0.5 m, and SMOS products are generally limited to a maximum thickness of 1 m (Tian-Kunze et al., 2014; Huntemann et al., 2014).

While the CryoSat products generally align in their spatial distribution and basin-scale gradients of sea ice thickness, this agreement is largely due to the shared use of empirical retracking algorithms, usually a modified threshold first-maximum retracking algorithm, and a modified snow climatology of Warren et al. (1999), which is originally designed for mature, multi-year sea ice (Tilling et al., 2018; Hendricks et al., 2021; Laxon et al., 2013). However, these approaches tend to overestimate snow when applied to young, thinner sea ice, introducing overestimation of freeboard retrieval.

This forms the basis of this study, which aims to re-evaluate the lower detection limit of CryoSat to determine whether reliable sea ice thickness estimates can

be retrieved down to a few tens of centimeters, within the sub-1 m range. The analysis is based on a physical retracking algorithm called LARM (Landy et al., 2020) and a snow accumulation model called SnowModel-LG (Liston et al., 2020), provided as a sea ice thickness product by the Earth Observation Group at UiT - The Arctic University of Norway. To additionally assess whether it is reasonable to include CryoSat-derived sea ice thickness data below 1 m in downstream applications, and to evaluate what a practical cutoff might be. In addition to providing insight into the conditions and scenarios in which the SMOS AWI sea ice thickness product could be used independently, and when it is more appropriate to rely solely on altimetry-based estimates or a combination of both. To address these objectives, the UiT product is compared to other publicly available CryoSat products, by Tilling et al. (2018) and Hendricks et al. (2021), using the SMOS AWI product as reference. Further analysis investigates the lower-limit performance of the UiT product through validation against upward-looking sonars and airborne campaign measurements, with SMOS AWI data for comparison.

1.0.1 Structure of Thesis

Chapter 2 introduces the theoretical background relevant to the thesis, including remote sensing principles, sea ice properties, and Earth observation techniques. It covers passive remote sensing, synthetic aperture imaging, and various altimetry methods used for sea ice thickness estimations, along with a summary of relevant previous work.

Chapter 3 presents the two satellite missions, CryoSat-2 and SMOS, as well as the validation campaigns, OIB, BGEP, and SMOSice. With their technical background for retrieving sea ice thickness.

Chapter 4 describes the datasets used in this study, including the satellite sea ice thickness products and the validation datasets. It outlines the preprocessing steps applied to the data and the procedures used for sea ice thickness retrieval.

Chapter 5 outlines the methodology applied in the study, including the resampling of observational grids, the statistical metrics used for evaluation, and a description of how the four main analyses are conducted.

Chapter 6 presents the results obtained from the different analyses, with supporting visualizations and statistical assessment.

Chapter 7 provides a discussion and interpretation of the results, highlighting key findings and their implications.

Chapter 8 summarizes the study outcomes and offers concluding remarks, along with suggestions for future work.

/2

Background

The following sections provide the relevant background for the satellite missions and validation campaigns. All figures in this chapter were produced by the author unless otherwise stated.

2.1 Basics of Remote Sensing

Remote sensing refers to the acquisition of information about Earth's surface without direct contact, typically via instruments mounted on satellites or aircraft. It operates by detecting the interaction of electromagnetic radiation with surface features, as different materials reflect, absorb, or transmit energy at varying wavelengths (Elachi and Van Zyl, 2021), a process further detailed in Section 2.1.1. Remote sensing systems can be categorized as either passive or active. Passive remote sensing relies on naturally available electromagnetic emissions, primarily solar radiation, and measures the reflected EM waves from Earth's surface, as illustrated in Figure 2.1 to the right. In contrast, active remote sensing emits its own EM signal and detects the signal reflected from the surface, as shown in Figure 2.1 to the left. Multispectral, hyperspectral, and microwave radiometry are examples of passive remote sensing systems, whereas synthetic aperture radar, lidar, and radar altimetry represent common

types of active remote sensing systems (Awange et al., 2013; Elachi and Van Zyl, 2021). A different remote sensing method, known as multimodal remote sensing, employs multiple instruments or acquisition techniques. A common future for most of the active remote sensing systems is the use of radar, which emits EM signals at selected wavelengths depending on the observational objective, as further detailed in Section 2.1.2. Section 2.1.3 briefly outlines the four main resolutions applied in remote sensing.

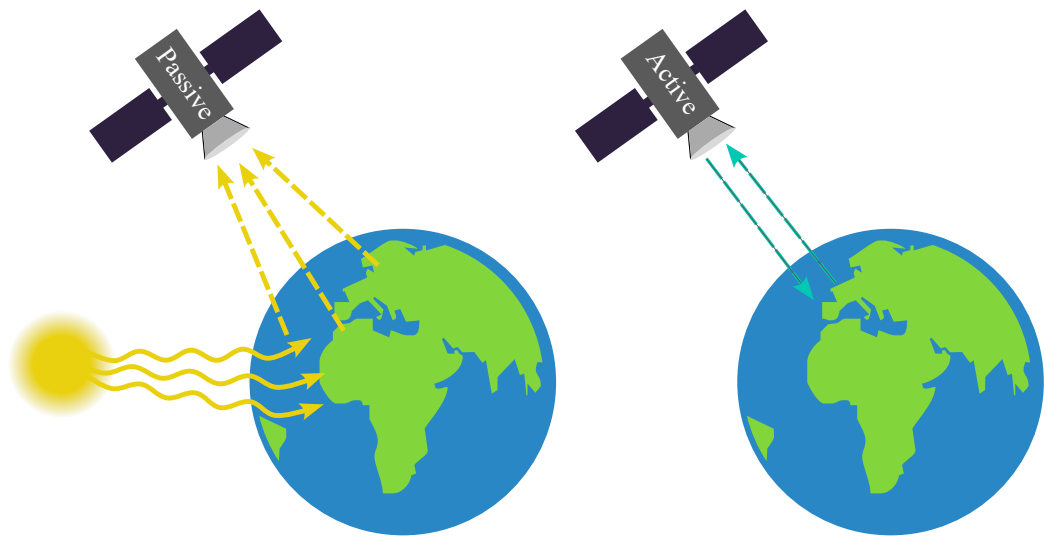


Figure 2.1: Illustration of passive (left) and active (right) remote sensing principles.

2.1.1 Electromagnetic Radiation

Remote sensing instruments, whether passive or active, depend on EM radiation. The EM energy is propagated by the EM radiation traveling at the speed of light, either directly through free space or indirectly via reflection, scattering, or reradiation before reaching the instrument. The EM energy carries the information that the instrument detects, which can be contained in its frequency, intensity, or polarization of the EM wave. The EM wave interaction with surfaces and the atmosphere is strongly influenced by the wave frequency. As a result, instruments are designed to operate at frequencies suited to their specific observational task (Elachi and Van Zyl, 2021). Figure 2.2 shows the frequency ranges and wavelengths used by active instruments (top) and passive instruments (bottom).

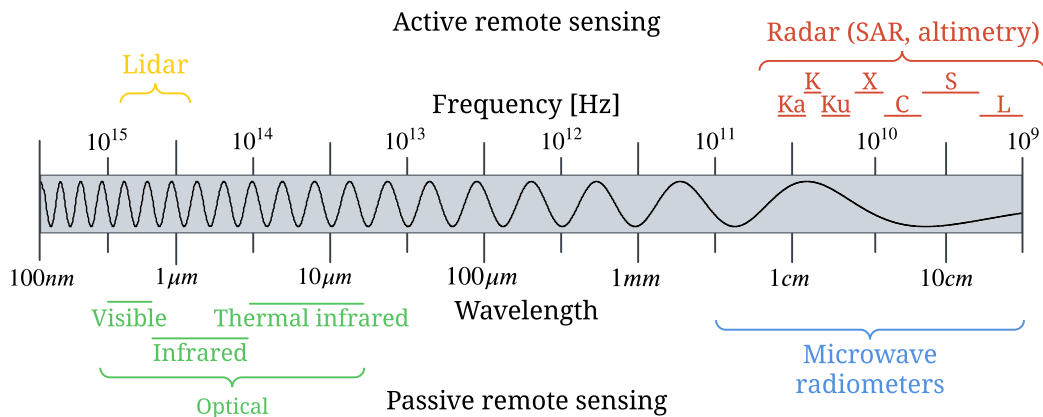


Figure 2.2: Visualization of the electromagnetic spectrum, indicating wavelength and frequency bands commonly used in remote sensing. Active imagery is shown in the upper half, and passive imagery in the lower half.

The observed target emits or reflects EM waves, and remote sensing instruments utilize different components of the wave equation solution, seen in Equation (2.1), to extract information about the target properties.

$$\vec{E} = \vec{A} e^{i(kr - \omega t + \phi)} = \vec{A} e^{i\Phi} \quad (2.1)$$

Where \vec{E} denotes the electric field vector, \vec{A} is the wave amplitude, k is the wave vector defined within the propagation medium, r is the position vector, ω is the angular frequency, t is time, and ϕ is the phase. k is given by $k = 2\pi\sqrt{\epsilon_r}/\lambda$, where ϵ_r is the relative permittivity, $\lambda = 2\pi c/\omega$ is the wavelength defined with the speed of light c . The term $kr - \omega t + \phi$ denoted Φ in Equation 2.1 represents the phase of the wave, which increases by 2π as the wave propagates a distance equal to the wavelength λ (Elachi and Van Zyl, 2021).

2.1.2 Radar

Radar systems operate by emitting EM waves, where the return signal is typically received by the same antenna. The behavior and performance of the radar system are described using the radar range equation defined as:

$$P_r = \frac{P_t G_t}{4\pi R_t^2} \frac{\sigma}{4\pi R_r^2} A_e \quad (2.2)$$

where P_r is the received power, P_t is the transmitted power, G_t is the transmitted antenna gain, R_t is the transmitter to target distance, σ is the radar cross section or it can be handled as the scatter coefficient of the target, R_r is the target to receiver distance, and A_r is receiver effective area. Most radars transmit and receive linearly polarized signals, direction of the polarization is either horizontal (H) or vertical (V) to the incident plane, while the return signal is usually H and V polarized. The combination of transmit and receive polarizations is denoted by four polarization codes: VV, VH, HV, and HH. Polarization is another radar characteristic that can enhance target discrimination and surface analysis (Quegan and Atkinson, 2008; Elachi and Van Zyl, 2021).

2.1.3 Resolutions

In remote sensing, four key resolutions are commonly used to characterize data: spatial, temporal, spectral, and radiometric resolution. Spatial resolution defines the size of a pixel within an image and the area of Earth's surface. Temporal resolution defines the time a satellite needs to revisit the same observation area, this highly depends on the satellite orbit and the instrument. Spectral resolution is used in the context of an optical system, where it defines the system's ability to distinguish between finer wavelengths. Radiometric resolution refers to the amount of information within one pixel and its sensitivity for differentiating between energy levels (NASA, 2021).

2.2 Synthetic Aperture Radar (SAR)

The basic principle behind synthetic aperture radar is to simulate a larger antenna to achieve higher spatial resolution, where it transmits and receives EM signals. Constructing such a large real aperture antenna to have an equal resolution as the SAR, would not be physically possible due to limitations of the satellite bus and launch vehicle. Instead, SAR exploits the satellite's forward motion (along-track) to synthesize a longer antenna, combined with a side-looking geometry. This allows the system to distinguish between signals returned from near-range (closer to the sensor) and far-range (further from the sensor). The region observed by the satellite is referred to as the line of sight (LOS), which is defined by the angle at which the sensor observes the ground surface. As SAR systems operate in the EM spectrum, from the microwave to the radio region, it enables the system to be daylight and weather

independent (Odh, 2024; Elachi and Van Zyl, 2021). SAR imaging geometry can be seen in Figure 2.3. Section 2.2.1 will cover the theory and further details behind SAR imaging.

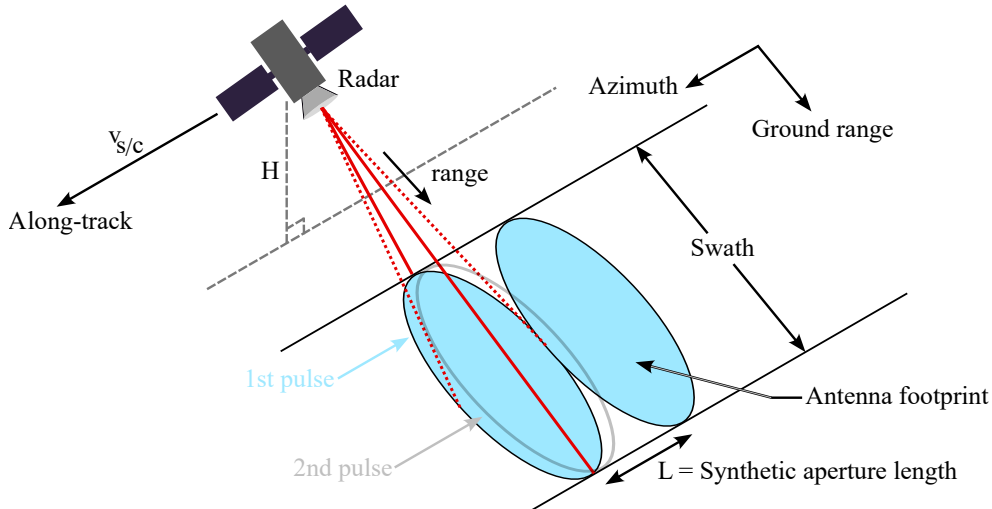


Figure 2.3: SAR imaging geometry moving along-track, highlighting key parameters and visualization of the 1st and 2nd pulse overlap.

2.2.1 SAR Theory

The spatial resolution of SAR is typically characterized by two components, ground range resolution and azimuth resolution. The ground range resolution X_r refers to the ability of the sensor to distinguish between two targets in the range (across-track) direction on the ground. Notably, it is independent of the sensor's altitude, and is defined by:

$$X_r = \frac{c}{2B\sin\theta} \quad (2.3)$$

where B is the bandwidth of the transmitted signal (equal to the frequency span Δf), and θ is the incidence angle between the radar beam and the surface at the point of interaction (Elachi and Van Zyl, 2021). The azimuth resolution X_a , describes the ability of the system to distinguish between two targets in the azimuth (along-track) direction and is given by:

$$X_a = \frac{L}{2} \quad (2.4)$$

where L is the physical length of the radar antenna. In general, a wider spatial resolution leads to a coarser resolution (Elachi and Van Zyl, 2021).

SAR relies on surface scattering mechanisms to return the signal (backscatter), which plays a crucial role in both signal strength and the extraction of surface properties, especially for applications such as sea ice monitoring. The main scattering mechanisms are surface scattering, volume scattering, and double bounce, as illustrated in Figure 2.4. The dielectric constant (k), also known as relative permittivity (ϵ_r), underlies all scattering mechanisms, as it defines the capacity of a material to store and transmit electric energy in the presence of an electromagnetic field (Elachi and Van Zyl, 2021).

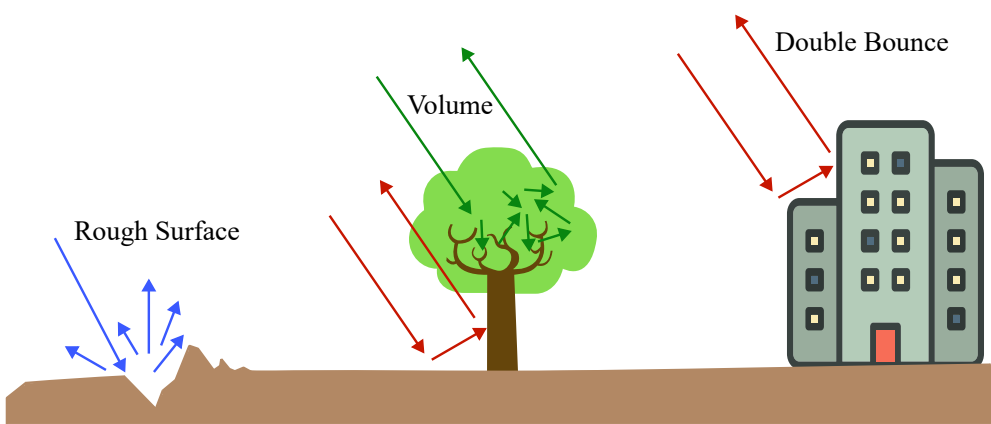


Figure 2.4: Main scattering mechanisms: surface scattering, volume scattering, and double bounce.

Surface scattering is controlled by the medium's dielectric properties and the surface's roughness, which is categorized as smooth, slightly rough, and very rough. The roughness of the surface is defined relative to the wavelength of the incoming signal, with different roughness criteria. Volume scattering occurs as the energy is transmitted into the medium and is scattered by dielectric discontinuities within the medium. These discontinuities arise from layered structures (e.g., snow on sea ice) or irregularities as ice crystals or air pockets, where the wavelength and the dielectric properties of the medium govern the penetration depth of the signal. Changes of the surface dielectric properties will also affect the penetration depth, these changes are often governed by changes in the liquid water content (e.g., snow melt). Double bounce scattering arises when the signal reflects between large, vertical structures and the ground surface, resulting in a high return signal to the sensor (Elachi and Van Zyl, 2021; Awange et al., 2013).

SAR data is represented as a complex image, where each pixel in the 2D array

contains a complex number composed of amplitude and phase. The amplitude corresponds to the backscatter intensity from the surface, whereas the phase reveals the time delay between transmission and reception, influenced by atmospheric propagation and surface reflectance (ICEYE, 2020; NISAR, 2020). The amplitude and phase components of a single look complex (SLC) SAR image is displayed in Figure 2.5. On its own, the phase information from a single SLC image is not directly interpretable. However, when combined with a second phase image from the same region, it can reveal surface changes of the observed target. This approach forms the basis for interferometric SAR (InSAR) processing.

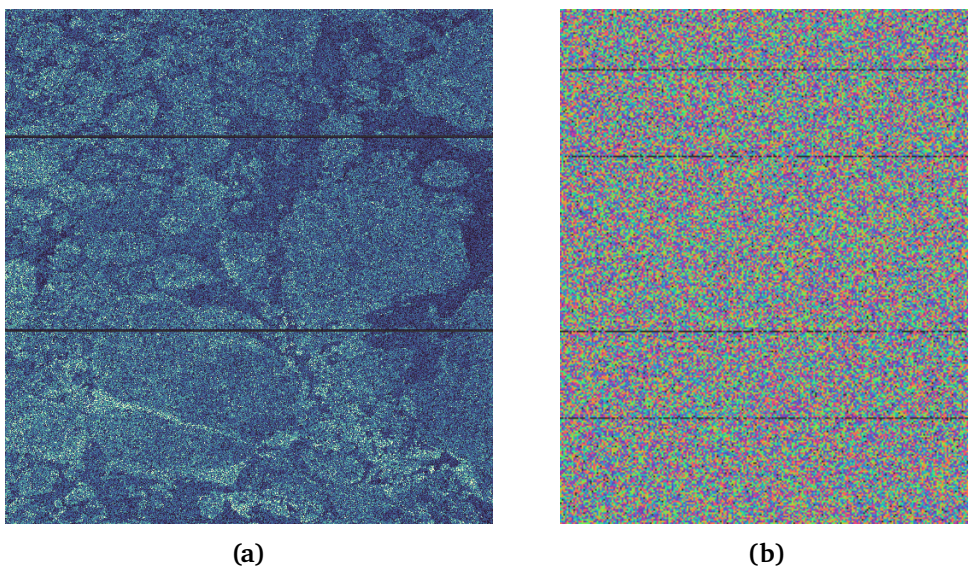


Figure 2.5: SAR complex image components: (a) shows the amplitude, and (b) shows the phase. The data is acquired by Sentinel-1 C-band SAR over the sea ice region north of Svalbard in April 2025.

2.3 Passive Microwave Sensing

Passive microwave sensing operates within the microwave region of the electromagnetic spectrum, as illustrated in Figure 2.2, and is implemented through instruments known as microwave radiometers. These sensors are inherently weather- and daylight-independent, making them particularly valuable for observing polar regions, where cloud cover and seasonal darkness limit optical methods. The satellite sensor measures naturally emitted microwave radiation (radiance), based on principles similar to thermal remote sensing, with

the observed signal being dependent on surface temperature, emissivity, and material properties. Due to its sensitivity to variations in surface emissivity, PM sensing is widely applied in sea ice monitoring, soil moisture retrieval, and sea surface temperature estimation (Elachi and Van Zyl, 2021).

2.3.1 Basic Passive Microwave Theory

Passive microwave sensing relies on the basic principle that all objects with a temperature above absolute zero emit thermal radiation, which is based on the idealized black body (BB) radiation curve. As for longer wavelengths ($\lambda \gg \lambda_{max}$) in the BB radiation curve, the relationship between spectral radiance and wavelength can be approximated by a linear function. This linear relationship is described by the Rayleigh-Jeans approximation, which expresses spectral radiance as a linear function of kinetic temperature. This simplification allows for the definition of brightness temperature T_B , which is the quantity measured by a PM sensor. Brightness temperature encapsulates both the kinetic temperature T of the emitting surface and its emissivity ϵ , and is expressed as:

$$T_B = \epsilon T = \frac{\lambda^4}{2hc} L_\lambda \quad (2.5)$$

where h is Planck's constant, and L_λ is the spectral radiance. The emissivity $\epsilon(\lambda)$ describes the efficiency with which an object emits energy compared to a BB at the same temperature. In addition, polarization and scattering mechanisms play a significant role in the detected radiance. While most naturally emitted microwave radiation is essentially unpolarized, transmission through or scattering by materials can induce polarization, typically resulting in elliptically polarized waves. The polarization state of reflected, scattered, or emitted radiation can be used to infer physical properties of the surface or medium, including composition, structure, and roughness (Elachi and Van Zyl, 2021).

2.3.2 Real-World Applications

Microwave emission models are essential for interpreting brightness temperatures measured by microwave radiometers. These models incorporate surface emissivity, influenced by the material's dielectric properties and surface roughness of the observed material, along with sensing geometry parameters such as incident angle, polarization, and frequency. They also decompose the to-

tal observed signal into contributions from volume scattering, atmospheric emission, reflected atmospheric emission, and reflected space emission (Elachi and Van Zyl, 2021). These models are typically expressed as functions of the material properties and the sensing geometry. For example, a model for layered snowpack may include a radiative transfer approach to represent volume scattering and absorption processes within the snow (Mätzler and Wiesmann, 1999). A simplified brightness temperature model that considers only surface and volume emissions can be expressed as:

$$T_{Bp} = \epsilon_{1p} T_{vol} + \epsilon_{2p} T_{surf} e^{k_e h / \cos(\theta)} \quad (2.6)$$

where ϵ_{1p} and ϵ_{2p} is the emissivity of a half-space with rough surface boundary from the volume and surface, respectively, T_{vol} and T_{surf} are the corresponding kinetic temperature, k_e is the extinction coefficient (absorption), h is the physical depth, and θ is the incidence angle of the observed emission (Fung and Chen, 2010). An illustration of the key parameters in this modeling framework is seen in Figure 2.6.

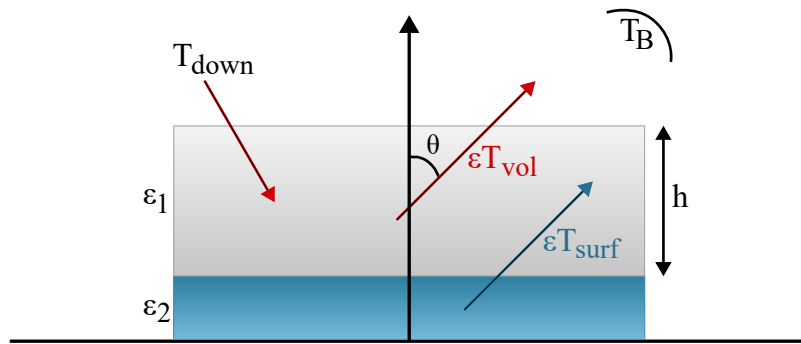


Figure 2.6: Illustration of a medium with parameters relevant for microwave emission modeling.

Such models are crucial in retrieving geophysical parameters, including sea ice coverage and thickness, by exploiting the significant emissivity contrast between sea ice and open water. At L-band frequencies, microwaves can penetrate thin sea ice, a feature utilized by the SMOS mission, which is described in more detail in Section 3.2. In this context, a semi-empirical regression model is used to relate SMOS brightness temperature tie points to sea ice thickness (d), and is defined as:

$$T_B = T_{B1} - (T_{B1} - T_{B0}) e^{-kd} \quad (2.7)$$

where T_{B_0} is the tie points for open water, T_{B_1} is the tie points for thick sea ice, and $k \sim \epsilon(S_{ice}, T_{ice})$ is from an microwave emission model, where S_{ice} is the bulk salinity and T_{ice} is the sea ice brightness temperature. This formulation allows the modeled and observed brightness temperature from SMOS to be associated with a corresponding sea ice thickness value (Kaleschke et al., 2012). This relationship is seen in Figure 2.7 based on the Equation (2.7).

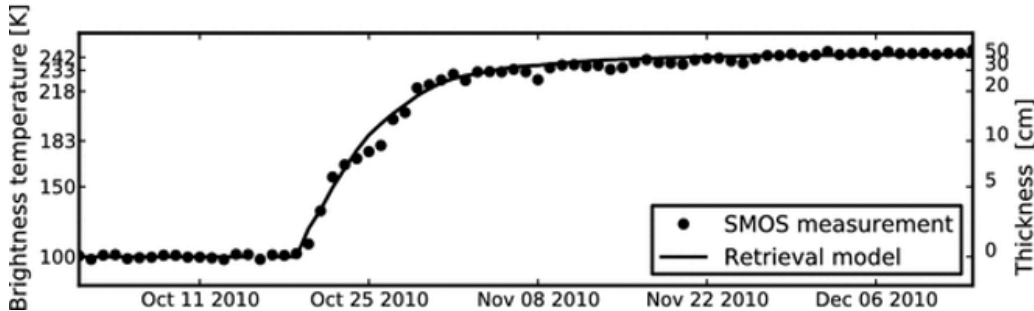


Figure 2.7: Observed and modeled SMOS brightness temperature with corresponding sea ice thickness, based on Equation (2.7). The sea ice thickness values from Lebedev's growth parameterization. From Kaleschke et al. (2012).

The currently used algorithm is a lot more involved than this, which is covered in Section 3.2 and 4.1.1.

2.4 Altimetry

Altimetry is primarily used to measure the surface topographic profile and provides high-precision global data of sea level and sea ice height. A satellite- or airborne-mounted altimeter transmits pulses of EM radiation, which are reflected or scattered by the target surface or volume. The receiver then detects the returning pulse (echo), and the pulse travel time t is recorded. This round-trip travel time is used to calculate the distance h_{obs} between the sensor and surface, defined as (Elachi and Van Zyl, 2021; Bašić, 2023):

$$h_{obs} = \frac{c \cdot t}{2} \quad (2.8)$$

This outlines the basic principle of altimetry, without corrections for signal propagation and geophysical parameters. The following sections provide further detail, with radar altimetry in Section 2.4.1, laser altimetry in Section 2.4.2, and SAR altimetry in Section 2.4.3.

2.4.1 Radar Altimetry

Radar altimeters operate in the K-band region of the electromagnetic spectrum, as shown in Figure 2.2, making them independent of daylight and weather conditions, and exhibiting low sensitivity to atmospheric and ionospheric disturbances. The height of a surface is determined relative to a defined geodetic reference frame, typically either a reference ellipsoid or the geoid. The reference ellipsoid (e.g., WGS84) is a mathematical approximation of Earth's shape, while the geoid reflects the ocean surface shaped solely by Earth's gravitational field. To accurately determine surface height, the position of the satellite must be known relative to a defined geodetic reference system. This position is typically obtained using GNSS or GPS, combined with ground-based measurements from DORIS (Doppler Orbitography and Radiopositioning Integrated by Satellite) and SLR (Satellite Laser Ranging). Figure 2.8 illustrates the altimetry system, including the reference ellipsoid, the geoid, and a GNSS satellite tracking the altimeter position. It also highlights the key parameters such as altimetric range and sea surface height (Bašić, 2023; Elachi and Van Zyl, 2021).

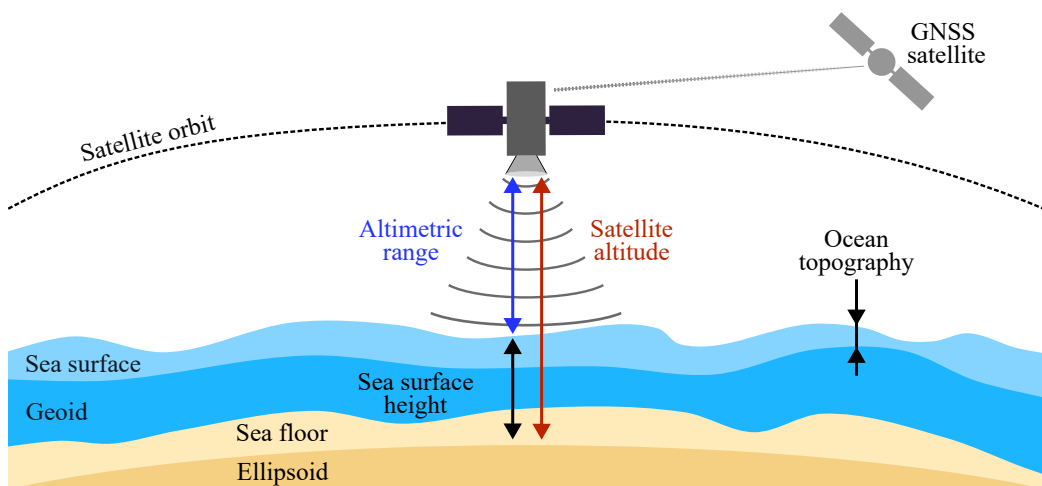


Figure 2.8: Principle of satellite altimetry, illustrating tracking of the satellite altimeter relative to the geodetic reference frames, ellipsoid, and the geoid. Key parameters such as satellite altitude, altimetric range, and sea surface height (SSH), along with the ocean topography.

In addition, a series of corrections is required, which may vary depending on the altimetry mission. These corrections account for signal propagation effects through the atmosphere and the geophysical properties of the surface, such as

water, snow, or ice. By including these corrections, the basic distance Equation (2.8) can be modified to the following form:

$$h = h_{obs} - \sum_i \Delta h_i = h_{obs} - (\Delta h_{tdry} + \Delta h_{twet} + \Delta h_{iono} + \Delta h_{dyn} + \dots) \quad (2.9)$$

where Δh_i , $i = 1 \dots$ represents the corrections, Δh_{tdry} and Δh_{twet} is the dry and wet components of the troposphere, Δh_{iono} represents the influence of the ionosphere, and Δh_{dyn} describes the dynamic components of the sea surface (Bašić, 2023). SSH is a key application of satellite altimetry and is essential for accurate retrievals of variables like sea ice thickness. The SSH is approximated as:

$$SSH = h_{OR} - h = h_{OR} - h_{obs} + \sum_i \Delta h_i \quad (2.10)$$

where h_{OR} is the satellite altitude. Additional corrections are also applied to account for tidal oscillations, derived from global tide models (Bašić, 2023). Altimeters can be classified as either beam-limited or pulse-limited, with pulse-limited altimeters being more frequently employed. Beam-limited altimeters utilize narrow radar beams, with the return pulse shaped by the beam width, illustrated in Figure 2.9. The footprint radius r_p is proportional to the sensor altitude h and the beam divergence θ , and is defined as:

$$r_p = h \tan\left(\frac{\theta}{2}\right) \quad (2.11)$$

This relationship highlights why beam-limited systems require very large antennas and is highly sensitive to pointing error, which influences both the amplitude and the measured range (Elachi and Van Zyl, 2021). In contrast, pulse-limited altimeters transmit pulses of duration t_p , where the shape of the return signal is governed by the pulse length. The footprint radius is proportional to the sensor altitude and inversely related to the bandwidth B , and is defined by:

$$r_p = \sqrt{h c t_p} = \sqrt{h \frac{c}{B}} \quad (2.12)$$

In this case, the footprint increases until the point of peak illumination (leading edge of the return waveform), after which the illuminated area remains constant (Elachi and Van Zyl, 2021). This behavior is illustrated in the second panel to the right in Figure 2.9.

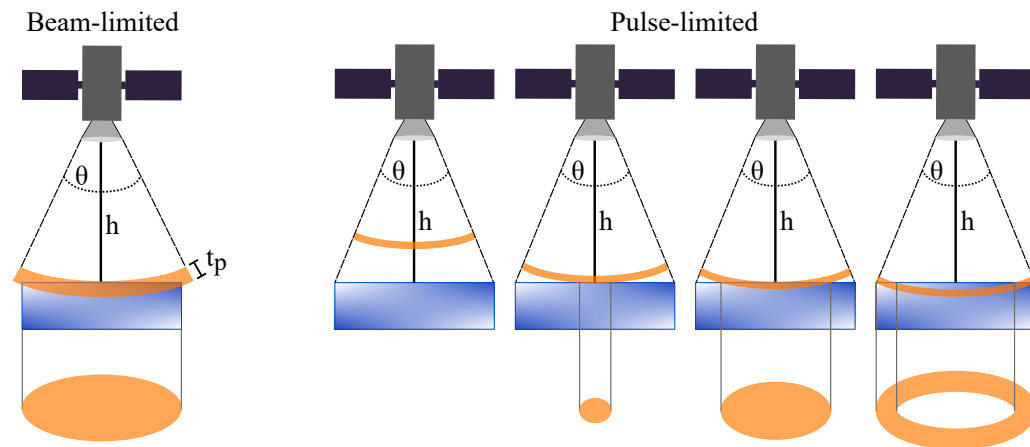


Figure 2.9: Illustration of beam-limited and pulse-limited altimetry, with beam divergence θ , observed height h , and pulse duration t_p .

The altimeter records the return power from the backscattered signal over the footprint, resulting in a waveform that represents power as a function of time, as illustrated in Figure 2.10. As shown right in Figure 2.10, the waveform is characterized by its leading edge, skewness, trailing edge, tracking point, useful signal amplitude P , and thermal noise P_0 . The slope of the leading edge reflects surface roughness, with a smoother surface producing steeper slopes. Skewness quantifies this slope. The trailing edge is shaped by the type of scattering, where surface scattering results in a fast decay, while volume scattering produces a more gradual decline. The tracking point indicates the radar signal time delay and is estimated via a tracking algorithm (Rosmorduc et al., 2011; Brown, 1977).

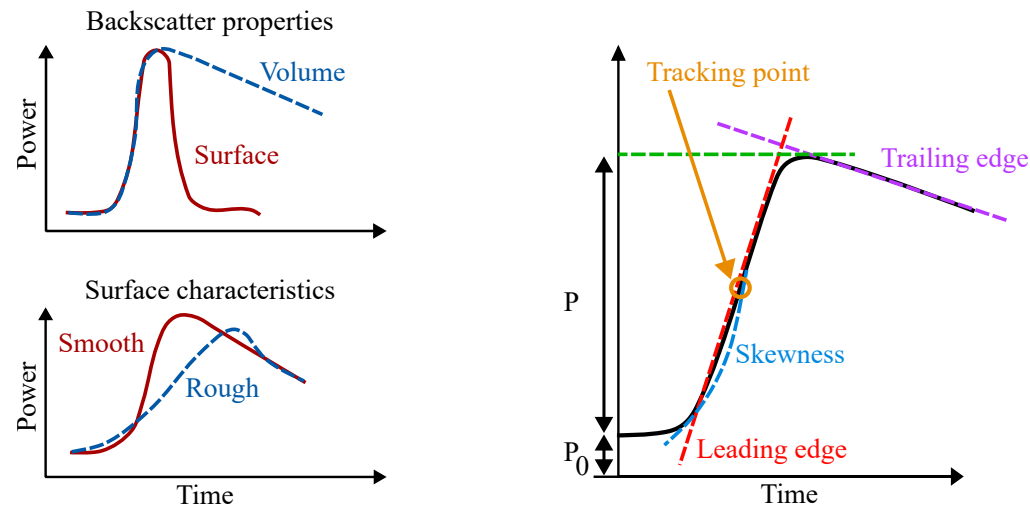


Figure 2.10: Illustration of a returned altimetry waveform, highlighting key waveform parameters on the right. The lower left panel demonstrates the influence of surface roughness on the leading edge, while the upper left panel shows the effect of backscatter properties and subsurface penetration on the trailing edge.

To relate waveform shape parameters to physical surface properties, one can apply either empirical or physical modeling approaches. Retracking is the ground-processing technique used to identify the point on the leading edge of the waveform (see tracking point in Figure 2.10) that corresponds to the true mean surface height. The empirical retracking approach involves deriving statistical relationships between waveform features and geophysical variables (e.g., mean sea ice elevation). A well-known example is the threshold first maximum retracking algorithm. In contrast, physical retracking simulates the backscattered radar echo using a forward model, with surface parameters retrieved through model inversion by determining the optimal tracking point or threshold (SentiWiki, 2025; Shi et al., 2024).

2.4.2 Laser Altimetry

Laser altimetry operates by emitting short pulses of laser radiation, typically at a wavelength around 530 nm, and detecting the portion reflected from the surface. The return radiation is captured by a photon-counting laser diode detection array, which detects, counts, and records the arrival time of individual photons. This method provides high spatial resolution due to its small footprint

(approximately 10-70 m). However, it requires clear-sky conditions, as cloud cover can attenuate the laser signal through photon absorption. Surface height is derived by analyzing the distribution of return photons over a distance and time (Zhou et al., 2017; Chambers, 2007).

2.4.3 SAR Altimetry

Another type of radar altimetry is SAR altimetry, often referred to as Delay-Doppler altimetry. It employs SAR techniques to sharpen the footprint in the along-track direction by exploiting the Doppler effect introduced by the satellite motion, similar to the principle used in SAR imaging. In this approach, the radar typically transmits bursts of 64 pulses. The Doppler beams from multiple bursts observe the same surface target and is subsequently stacked, known as multilooking (illustrated in the left panel of Figure 2.11). This stacking improves the signal-to-noise ratio and reduces the along-track footprint (e.g., 300 m rather than 2 km) via Doppler processing. Based on the phase shift, the footprint can be subdivided into Doppler beams, as shown in the right panel of Figure 2.11 (Chambers, 2007; Elachi and Van Zyl, 2021).

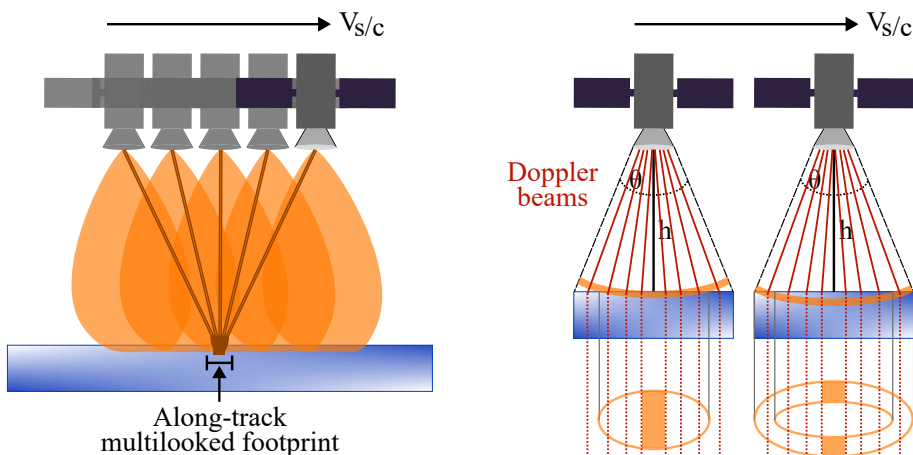


Figure 2.11: Principle of SAR altimetry: the left panel shows the along-track multilooked footprint resulting from Doppler beam stacking, while the right panel displays the subdivision of the footprint into Doppler beams based on the phase shifts.

2.5 Sea Ice Monitoring



Figure 2.12: Captured image of the Arctic sea ice conditions. Image credit: NOAA.

Monitoring Arctic sea ice is of critical importance for several reasons. It serves as a key indicator of climate change, and its variations have effects on global weather patterns, ocean circulation, and maritime navigation (eoPortal, 2025). The observed decline in sea ice is a direct consequence of the rapid climate warming and, in turn, contributes to further warming through several mechanisms. These include a reduction in surface albedo, increased oceanic heat loss, enhanced water vapor and cloud radiative feedbacks, and the influence of the stratified boundary layer's low heat capacity (Vihma, 2014). As a result of climate change, a greater portion of thin first-year ice is now present in the Arctic, playing a central role in seasonal sea ice variability (Polyak et al., 2010). Thin sea ice forms and spreads rapidly across large areas each autumn as the ocean refreezes and is the first to melt in spring, dominating changes in ice extent at the marginal ice zones. It also plays a significant role in the large-scale heat and mass balance at the surface of the polar oceans (Maykut, 1978).

Satellite monitoring plays a central role in tracking these changes, enabling the observations of essential sea ice parameters such as extent, concentration, drift, type, thickness, snow cover, and melt onset (eoPortal, 2025). Among these, sea ice thickness information is particularly important for forecasting systems, which predict how the ice will grow, move, or melt under changing

weather. Accurate sea ice thickness data improves the model's initial conditions, leading to a more reliable forecast of sea ice extent and edge location. However, satellite-based sea ice monitoring still faces challenges, particularly due to the influence of snow cover and the dynamic nature of sea ice (Jaklin, 2025).

The following sections present an overview of sea ice theory (Section 2.5.1), monitoring techniques (Section 2.5.2), methods used to estimate SIT (Section 2.5.3) and the use of satellite-derived SIT data assimilation for forecasting systems (Section 2.5.4).

2.5.1 Sea Ice Theory

Sea ice is commonly categorized into two main types, first-year ice and multi-year ice. FYI refers to ice thicker than 30 cm and has not survived a summer melt season. In contrast, multi-year ice has typically persisted through one or more summer melt seasons and usually ranges in thickness from 2-4 m. Additional classification of sea ice includes new ice, nilas, and young ice, each distinguished by its age, thickness, and formation characteristics. Due to the dynamic nature of sea ice, features such as melt ponds, polynyas, and leads often form. During summer, melt ponds can accumulate lower than average floe height. Polynyas are larger open water areas within the ice pack, while leads are narrow openings between ice floes (WMO, 2025). The formation and structure of sea ice are complex, but several fundamental physical parameters define its characteristics. These include temperature, salinity, crystal structure (which incorporates brine pockets and air inclusions), surface roughness, snow cover, and the presence of water on its surface. These factors are strongly influenced by seasonal variations and the age of the sea ice, where, for example, salinity decreases as the ice matures (Sandven and Johannessen, 2006).

2.5.2 Techniques of Monitoring Sea Ice

Over the past decades, various remote sensing techniques have been employed for monitoring sea ice, including SAR, PM radiometry, and laser and radar altimetry. Each of these techniques offers unique capabilities for detecting and monitoring sea ice parameters, primarily due to the difference in wavelength and penetration properties, as illustrated in Figure 2.13. The figure provides an overview of the fundamental sea ice structure and highlights key geophysical parameters such as snow depth, sea ice thickness, ice freeboard, and sea ice draft. It also indicates the relative penetration depths of different sensors, as

laser altimeters observe the snow surface, radars typically penetrate to the snow-ice interface, and passive microwave radiometers measure the brightness temperature emitted from the surface or subsurface layers. Furthermore, the diagram displays standard assumptions regarding the physical properties of snow (ρ_s), ice (ρ_{si}), and sea water (ρ_{sw}) in sea ice remote sensing.

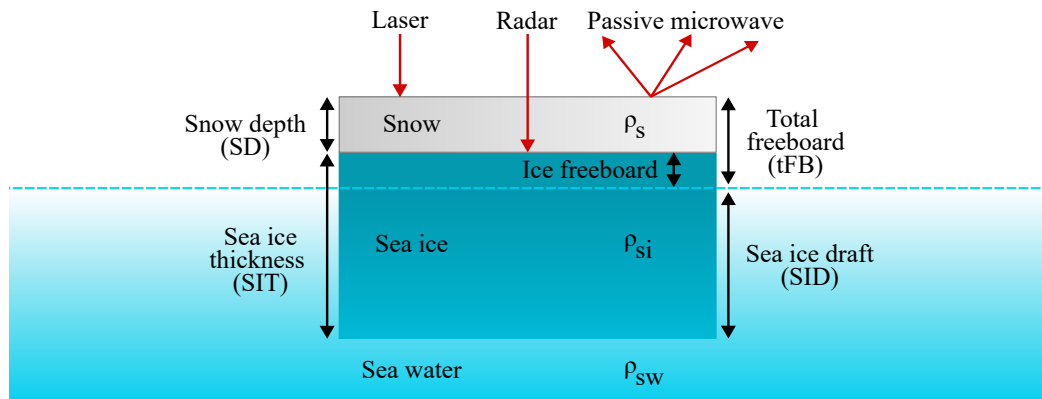


Figure 2.13: Figure illustrating the key components of sea ice monitoring. Showing the vertical structure of the sea ice system, including snow depth (SD), total freeboard (tFB), ice freeboard, and sea ice draft (SID). It indicates the different layers and what different sensors observe.

Sea ice monitoring using SAR is primarily applied to retrieve parameters such as sea ice concentration, classification, and drift. This is achieved by analyzing the backscatter characteristics of sea ice and open water, which are influenced by several sea ice properties, including salinity (affecting the dielectric constant and penetration depth), layering, and surface roughness. Figure 2.14 presents a SAR image capturing the structure and extent of sea ice. PM radiometry supports a range of sea ice applications, notably the estimation of sea ice extent and thin sea ice thickness when using L-band frequencies. PM radiometry relies on variations in surface and subsurface emissivity, with a particularly strong contrast between the emissivity of sea ice and open water. A key property influencing this contrast is the brine content within the sea ice. As sea ice ages and undergoes deformation, changes in salinity and roughness alter its dielectric properties, which allow PM radiometers to distinguish between different ice types and infer thickness. Laser and radar altimetry are mainly used for estimating sea ice thickness, with laser altimetry offering a higher spatial resolution and more precise thickness estimates, especially in the detection of freeboard and surface elevation. Where more precisely the radar altimeter measures the radar freeboard, (Sandven et al.,

2023; Sandven and Johannessen, 2006).

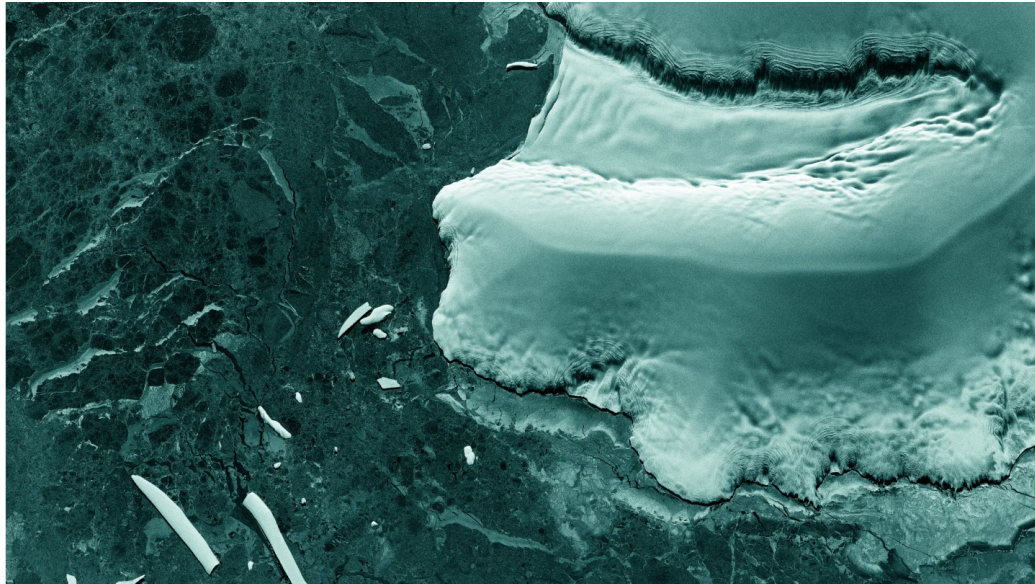


Figure 2.14: SAR image capturing sea ice and grounded ice formations in Antarctica, acquired by the ICEYE satellite constellation. Image credit: ICEYE

2.5.3 Sea Ice Thickness Estimation

Due to the complex structure and variability of sea ice, different parameters must be assumed or approximated to enable sea ice thickness retrieval. One common approach involves the use of snow and ice climatology models. For SIT retrieval using PM radiometry, the method typically assumes a negligible impact of snow cover on the emission and assumes thermal equilibrium between the sea ice surface temperature and the near-surface air temperature. In addition, the retrieval process relies on auxiliary datasets, including atmospheric reanalysis data (e.g., Japanese 55-year Reanalysis, JRA55) and sea surface salinity climatology model (e.g., MIT General Circulation Model, MITgcm). The observed brightness temperature is then related to the SIT through a semi-empirical model (Tian-Kunze et al., 2014)¹, as described in Section 2.3.2. These assumptions and geophysical parameters used in these models introduce uncertainties into the final SIT estimates.

For SIT retrieval using altimeters, the method is based on measuring freeboard,

1. The description of SIT retrieval from PM radiometry follows the methodology used in the SMOS SIT retrieval algorithm.

specifically the radar freeboard. This is converted to ice freeboard by applying corrections for the delayed radar signal propagation through the snow layer. The conversion from ice freeboard to SIT depends on approximations of several geophysical parameters, including snow depth and density, sea ice, and sea water density. Snow depth and density are typically obtained from snow climatology models, such as the Warren 1999 climatology, often applied in a modified form. Sea ice density may be estimated through assimilation techniques that relate it to SIT and snow depth or by applying a bimodal distribution that distinguishes between FYI and MYI (Sievers et al., 2024). The derivation of SIT assumes that the ice is in hydrostatic equilibrium, for radar altimetry, this is expressed by the following equation.

$$SIT = \frac{h_{iFB}\rho_{sw}}{(\rho_{sw} - \rho_{si})} + \frac{SD\rho_s}{(\rho_{sw} - \rho_{si})} \quad (2.13)$$

where h_{iFB} is the observed ice freeboard in Figure 2.13. For laser altimetry, the retrieval uses the total freeboard (h_{tFB}) (Zygmuntowska, 2014), expressed by:

$$SIT = \frac{h_{tFB}\rho_{sw}}{(\rho_{sw} - \rho_{si})} + \frac{SD(\rho_s - \rho_{sw})}{(\rho_{sw} - \rho_{si})} \quad (2.14)$$

An essential step in radar-based SIT retrieval is the application of a retracking correction to accurately estimate the surface elevation, as detailed in Section 2.4.1.

2.5.4 Data Assimilation

One of the key applications of satellite-derived SIT data is its use in forecasting systems through data assimilation techniques. These systems blend satellite observations with model outputs to produce an optimized representation of sea ice conditions. Assimilating SIT data from satellites, such as CryoSat and SMOS, helps to correct model biases and improve forecasts of sea ice extent and ice edge localization (Mignac et al., 2022; Lee and Ham, 2023). In recent years, several studies have demonstrated that assimilating CryoSat and SMOS SIT data yields a significant improvement of sea ice forecasts (e.g, Mu et al. (2020); Mignac et al. (2022); Lee and Ham (2022, 2023)).

Currently, it is common practice to use SMOS data for thin ice regimes and CryoSat data for thicker ice. This approach often excludes altimetry-derived estimates of thin ice or assigns them large uncertainties (Mu et al., 2020; Mignac et al., 2022), based on that CryoSat products exhibit increased uncertainty towards thinner ice of 1 m (Ricker et al., 2017). Conversely, while

SMOS is considered reliable for SIT up to 1 m, it also exhibits exponentially increasing uncertainty for ice thicker than approximately 0.5 m (Tian-Kunze et al., 2014). Underscoring the importance of improving SIT retrieval across the full thickness range, especially in the context of the Arctic's continued shift toward thinner FYI (Maykut, 1978).

2.6 Previous work

A range of previous studies have conducted assessments and intercomparisons of satellite sea ice thickness products, either spanning the full thickness range or focusing on thinner ice regions. However, none of these studies have yet included the newer CryoSat UiT product.

A notable example is the study by Sallila et al. (2019), which utilizes eight years of SIT observations from multiple CryoSat products, including CPOM and AWI, as well as the merged CryoSat and SMOS product (CS2SMOS from Ricker et al. (2017)). The analysis incorporated data from the eight years to calculate statistical metrics across different Arctic regions, covering the full SIT range. Validation was conducted using datasets from the BGEP ULS moorings and the OIB campaign. The study concluded that CryoSat products are capable of reliably retrieving SIT within the approximate range of 0.5 to 4 m, with CS2SMOS performing best in the thin ice regime.

In another study, Zhang et al. (2024) focused on Arctic regions with a mean SIT below 1 m, using data from CryoSat AWI, SMOS AWI, and the CS2SMOS product. Validation was performed using several reference datasets, including OIB and CryoVEx campaigns. The findings indicated that the CryoSat AWI product exhibited the highest multi-year mean SIT from 2011 to 2022 and showed optimal agreement with reference datasets. Between 2018 and 2022, it was found to outperform the other products overall. It is important to note that even in this study targeting thin ice, regional SIT values can exceed 1 m, and the validation datasets are biased toward thicker ice (e.g., the OIB campaign).

Additionally, Wang et al. (2016) compared SIT estimates from various satellite and airborne missions, including CryoSat AWI and SMOS products from the University of Hamburg (later maintained by AWI). Using data from 2011 to 2013, they reported a mean SIT difference of 0.13 m in March and -0.24 m in October within the 0 to 1 m thickness range.

Another relevant study is presented by Sievers et al. (2024), which investigates the influence of key geophysical parameters, such as snow thickness, snow density, sea ice density, and water density, on CryoSat-derived sea ice thickness

estimates. The analysis includes a comparison across several existing CryoSat SIT products and highlights the sensitivity of retrievals to variations in these parameters.

These studies share an agreement that CryoSat is capable of providing SIT estimates for thin FYI ice, with a resolution limit around 0.5 m (Sallila et al., 2019), and SIT estimates below 1 m are associated with large uncertainties (Ricker et al., 2017).

/3

Satellites & Campaigns

In this study, sea ice thickness data are obtained from two satellite missions: CryoSat-2 and SMOS. An overview of the CryoSat-2 mission is provided in Section 3.1, with details on its radar altimeter, SIRAL, in Section 3.1.1. The relevant data processing levels for sea ice thickness products, including those delivered by ESA, are presented in Section 3.1.2. The SMOS mission, which provides complementary comparison data, is introduced in Section 3.2, and its instrument, MIRAS, is described in Section 3.2.1.

3.1 CryoSat-2



Figure 3.1: Artist's impression of CryoSat-2 in orbit. Image credit: ESA / P. Carril

CryoSat-2 was launched in April 2010, as part of the Earth Explorer Opportunity missions of the ESA Living Planet Program. It replaced CryoSat-1, which was lost due to a launch failure. CryoSat operates in a polar, retrograde, non-sun-synchronous orbit at an altitude of 720 km, with a 369-day repeat cycle and a 30-day sub-cycle. This enables high-density spatial coverage of the polar regions and reliable measurements down to the south of Greenland with a general spatial resolution of 25 km (Parrinello et al., 2018). CryoSat has two primary scientific objectives: first, to determine regional and basin-scale trends in Arctic sea ice thickness and mass, and second, to quantify the regional and total contributions of the Arctic and Greenland ice sheets to global sea level rise. In addition to these main goals, secondary objectives include monitoring the seasonal cycle and inter-annual variability of sea ice thickness and mass in both the Arctic and Antarctic, as well as assessing changes in the thickness of the world's ice caps and glaciers (Parrinello et al., 2018). The Synthetic Aperture Radar and Interferometric Radar Altimeter (SIRAL) serves as the principal instrument onboard CryoSat. It measures the ice freeboard, also known as radar freeboard, the ice surface above the sea level from which sea ice thickness is derived. Since the launch of CryoSat, a range of products have been developed utilizing different approaches to radar altimeter waveform retracking to estimate sea ice thickness and volume, each employing different approaches (e.g. Laxon et al. (2013); Kurtz et al. (2014); Tilling et al. (2018);

Landy et al. (2020); Hendricks et al. (2021)). These methods generally show good agreement in terms of regional distribution and basin-scale trends of the Arctic sea ice thickness (Sallila et al., 2019; Ricker et al., 2017). While the products align well in some of their objectives, they diverge in the absolute sea ice thickness estimates (Sallila et al., 2019). CryoSat has demonstrated the capability to measure both MYI thickness, as it was originally designed for, and FYI thickness. However, estimates of thin FYI thickness are associated with significantly higher uncertainties (Ricker et al., 2017; Müller et al., 2023).

3.1.1 SIRAL

The radar altimeter SIRAL is a single-frequency Ku-band radar (13.575 GHz, 2.2 cm wavelength) that differs from conventional pulse-limited altimeters by utilizing the phase coherence of the radar echo, made possible through the high-resolution waveforms acquired in SAR and SARIn modes. SIRAL operates in three different modes, Low Resolution mode (LRM), Synthetic Aperture Radar mode (SARM), and Synthetic Aperture Radar interferometric mode (SARInM) (Wingham et al., 2006; Parrinello et al., 2018). The LRM operates as a conventional pulse-limited altimeter, utilizing a single antenna for both transmission and reception of radar signals. At an altitude of approximately 730 km, this configuration yields a footprint of about 1.7 km, which corresponds to the pulse-limited footprint (PLF) of the SIRAL instrument. It is mainly operated over flat ice surfaces such as the interiors of Antarctica and Greenland, as well as ice-free ocean regions (Tilling et al., 2018; Parrinello et al., 2018). Additionally, LRM contributes to the continuity of ice sheet and basin-scale data with earlier satellite altimetry missions, such as ERS and ENVISAT, as demonstrated in previous studies (Sandberg Sørensen et al., 2018). SARM functions using along-track aperture synthesis with a single antenna, which enhances the ability to distinguish between open water and leads. This is achieved by emitting rapid, coherent bursts of radar pulses at a high interval rate. This enables the decomposition of the illuminated surface into 64 narrow strips, enhancing along-track resolution. Each surface location is observed multiple times within overlapping bursts, allowing for the construction of multi-looked stacks to reduce speckle noise. The along-track sampling resolution for each strip is around 250 m wide, while the antenna's limitations determine the across-track footprint in SARM and can reach up to 15 km, depending on the altitude (ESA, 2013; Tilling et al., 2018). SARM is generally utilized in regions with sea ice coverage (Parrinello et al., 2018). SARInM builds upon SAR capabilities by incorporating two identical antennas positioned side by side, enabling across-track interferometry. This configuration allows the

system to estimate the angle of arrival of radar echoes in the across-track direction, thereby improving the accuracy of the echo location. As a result, SARInM is particularly suited for use along the margins of major ice sheets (Wingham et al., 2006; Parrinello et al., 2018). For SIT retrieval, the primary operational modes used are SARM and SARInM. The spatial distribution of these modes is illustrated in Figure 3.2, where LRM is shown in red, SARInM in pink, and SARM in green. SIT retrieval products are generally limited to the winter months, typically from October to April. Meltwater ponds formed during the summer can make it difficult to separate radar returns from leads, thereby reducing the accuracy of freeboard measurement. However, recent studies have explored the use of SAR imagery to distinguish leads from melt ponds, enabling the estimation of sea ice thickness during the melt season (Dawson et al., 2022).

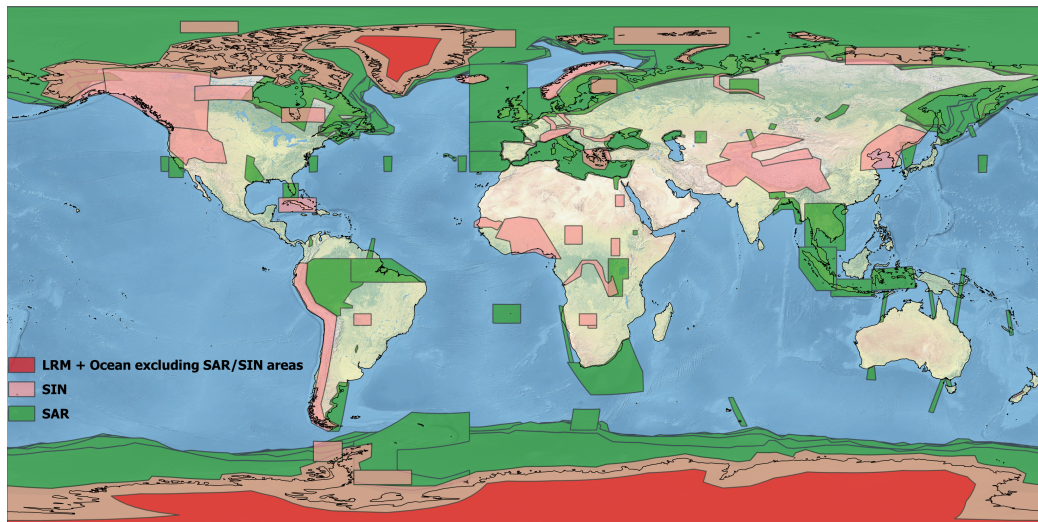


Figure 3.2: LRM in red, SARInM (SIN) in pink, and SARM (SAR) in green, Operational Geographical Mode Mask v5.0. Image plot credit: ESA.

3.1.2 Processing Levels

CryoSat products are structured according to processing levels, each with corresponding sub-levels (e.g., L1A, L2P, L3C) that indicate the specific processing steps applied within a given level. These classifications typically follow the ESA naming convention¹. Higher processing levels generally provide more

1. From CCI Data Standards v2.2, ESA Document CCI-PRGM-EOPS-TN-13-0009, published by the ESA Climate Office

user-friendly and application-ready data products. Level 0 (L0) refers to the raw sensor data in its unprocessed form, while Level 1 (L1) consists of data that has undergone initial processing, such as time referencing (L1A), conversion to physical units (L1B), and correcting radiance (L1C). These two levels are primarily provided directly by ESA to researchers for further processing, while the higher-level products are developed by external research institutes for specific scientific applications. Level 2 (L2) contains geophysical variables derived from L1 data, such as temperature, radar freeboard, or ice sheet elevation (Wingham et al., 2006), at the original resolution and observation location, and is formatted for easier handling (L2P). Level 3 (L3) represents L2 data that has been mapped to a consistent spatial or temporal grid, either by gridding individual observations (L3U, uncollated), merging multiple overpasses (L3C, collated), or combining data from different instruments or platforms (L3S, super-collated). Level 4 (L4) provides fully processed, gap-free datasets that often include mode-based interpolation and are the most user-friendly for scientific analysis. This description follows the ESA CCI Data Standards. However, the specific naming conventions and processing definitions may vary slightly between missions and external CryoSat products.

3.2 SMOS



Figure 3.3: Artist's impression of SMOS in orbit. Image credit: ESA/AOES Medialab.

The Soil Moisture and Ocean Salinity mission, launched in November 2009, is the second Earth Explorer Opportunity mission under the ESA Living Planet program, following CryoSat, which was selected earlier but launched later (Mecklenburg et al., 2016; Drinkwater et al., 2004). With a polar, frozen, sun-synchronous orbit at 758 km and an inclination of 98.44°, SMOS maintains a 149-day repeat cycle and an 18-day sub-cycle. This configuration allows for daily monitoring of Arctic sea ice, reaching latitudes as far north as 87°N. It is the first mission to provide global measurements of L-band brightness temperatures, enabling the retrieval of both soil moisture and ocean salinity data (Barre et al., 2008; Mecklenburg et al., 2016). To achieve these objectives, the mission is equipped with the Microwave Imaging Radiometer using Aperture Synthesis (MIRAS), which measures L-band brightness temperature. SMOS has two primary scientific objectives: to provide global estimates of volumetric soil moisture and global measurements of ocean salinity. In addition to these goals, SMOS data also offer valuable insights into vegetation dynamics, drought and flood risk assessment, surface ocean winds during storms, and sea ice conditions (Mecklenburg et al., 2016). Although not originally designed for sea ice monitoring, SMOS has proven capable of retrieving thin sea ice thickness estimates, primarily due to the deep penetration capability of the L-band (Kaleschke et al., 2010; Tian-Kunze et al., 2014). Two established SMOS sea ice thickness products have been developed, one by the University of Bremen (Huntemann et al., 2014), and the other by the Alfred Wegener Institute (Tian-Kunze et al., 2014), which was originally created at the University of Hamburg. The Bremen product is based on an empirically trained model that emphasizes high-incidence-angle observations (Huntemann et al., 2014), whereas the AWI product adopts a model-driven approach that explicitly incorporates the physical properties of sea ice (Tian-Kunze et al., 2014). A known limitation of SMOS-based retrievals is the exponential increase in uncertainty for sea ice thickness exceeding approximately 0.5 m. As a result, the University of Bremen product excludes any values exceeding this threshold, whereas the AWI product allows estimates up to 1 m, despite the higher associated uncertainty (Huntemann et al., 2014; Tian-Kunze et al., 2014; Kaleschke et al., 2010). The SMOS products, along with the Level 1 and Level 2 processing steps primarily provided by ESA, follow the same naming convention established by ESA¹, as outlined in Section 3.1.2.

3.2.1 MIRAS

The MIRAS instrument is a passive microwave two-dimensional interferometric radiometer that operates in the L-band (1.413 GHz, 21 cm wavelength),

within the protected 1400 - 1425 MHz frequency range to minimize radio frequency interference (RFI) (Mecklenburg et al., 2016). Despite operating within a protected frequency range, the mission experienced significant radio frequency interference during its early phase, which remains detectable to this day (Huntemann et al., 2014). The MIRAS instrument is designed with a central hub and three arms arranged in a Y-shape configuration, each housing 69 individual antenna receivers (Mecklenburg et al., 2016; Kaleschke et al., 2010). Together, these receivers operate using aperture synthesis to achieve a spatial resolution equivalent to a much larger real-aperture radar antenna (McMullan et al., 2008; Huntemann et al., 2014). The measured radiance signals are cross-correlated to capture the spatial coherence of the incoming radiation. A Fourier-like inverse transform is then applied to the correlated data, synthesizing a two-dimensional field of brightness temperature (Corbella et al., 2004; Huntemann et al., 2014). Each resulting image, referred to as a "snapshot", has a hexagonal footprint and consists of 100×100 brightness temperature pixels (Kaleschke et al., 2010). This represents a key innovation of MIRAS, enabling two-dimensional imaging without mechanical antenna scanning, a distinct advantage over traditional scanning or push-broom radiometers (Martín-Neira et al., 2016). From each snapshot, the instrument captures brightness temperatures at incident angles ranging from 0° to 55° , covering a swath width of approximately 1000 km, which allows for a spatial resolution between 35 km and 50 km, depending on the incident angle (McMullan et al., 2008; Mecklenburg et al., 2016). Additionally, MIRAS is capable of operating in both dual and full polarization modes, with full polarization being the standard operational mode currently in use (Mecklenburg et al., 2016). As previously mentioned, the use of L-band allows for a significant penetration depth into sea ice, typically between 0.5 m and 1.5 m, depending on the salinity of the ice. In addition, the brightness temperature contrast between sea ice and open water exceeds 100 K across all incident angles and polarization configurations, with sea ice consistently exhibiting higher brightness temperatures. These properties highlight the capability of the MIRAS instrument to effectively detect and estimate thin sea ice thickness. The processed sea ice products derived from MIRAS observations are gridded into a 12.5 km spatial resolution using the National Snow and Ice Data Center (NSIDC) polar stereographic projection, downscaling from the instrument's native resolution of approximately 35 km to 50 km (Kaleschke et al., 2010; Huntemann et al., 2014; Mecklenburg et al., 2016).

3.3 Operation IceBridge

The airborne campaign Operation IceBridge, led by the National Aeronautics and Space Administration, conducted its first flight in the spring of 2009. The campaign was initially launched to bridge the temporal data gap between the decommissioning Ice, Cloud, and Land Elevation Satellite (ICESat) in 2009 and the launch of ICESat-2 in 2018 (Lemmens, 2015). For the estimation of sea ice thickness, which depends on the accurate retrieval of sea ice freeboard and snow depth, the OIB mission is equipped with the Airborne Topographic Mapper (ATM) laser altimeter, a Ku-band radar altimeter, a Digital Mapping System (DMS) for aerial imagery, a snow radar, and a KT-19 infrared pyrometer for surface temperature measurements. The ATM is a scanning laser altimeter operating at a wavelength of 532 nm. It provides accurate measurements of total sea ice freeboard, defined as the combined height of the sea ice surface above water level and overlying snow, with an elevation accuracy of approximately 10 cm or better and has a nominal spatial resolution of 1 m. The snow radar determines the snow depth by detecting both the snow-air and snow-ice interface, providing measurements at a nominal spatial resolution of 15 m. The DMS is employed to classify sea ice surface types and leads, which play a crucial role in the sea ice freeboard retrieval processes. However, during the 2009 campaign, the DMS was not available, and the Continuous Airborne Mapping By Optical Translator (C�BOT) imaging system was used as an alternative. The final processed OIB product, IDCS14, provides sea ice freeboard, snow depth, and sea ice thickness at a spatial resolution of 40 m (Kurtz et al., 2013). From the launch of the campaign until 2013, the public release of OIB data typically required more than one year, encompassing data collection, processing, and distribution. A quick-look (QL) product, involving substantially less processing than the fully processed dataset, was introduced in 2012 to support time-sensitive applications such as the initialization of seasonal forecast models and sea ice forecasting. The QL product delivers 40 m along-track estimates of snow depth and sea ice properties, containing the same core variables as the one-year processed OIB data, but released within about one month after data collection (King et al., 2015). After 2013 and until 2019, the QL product became the primary source for these estimates. The OIB mission primarily covers regions dominated by multi-year sea ice, as illustrated by the flight paths used for this study shown in Figure 3.4, which include the March flight tracks from 2014 to 2017 used for the QL data.

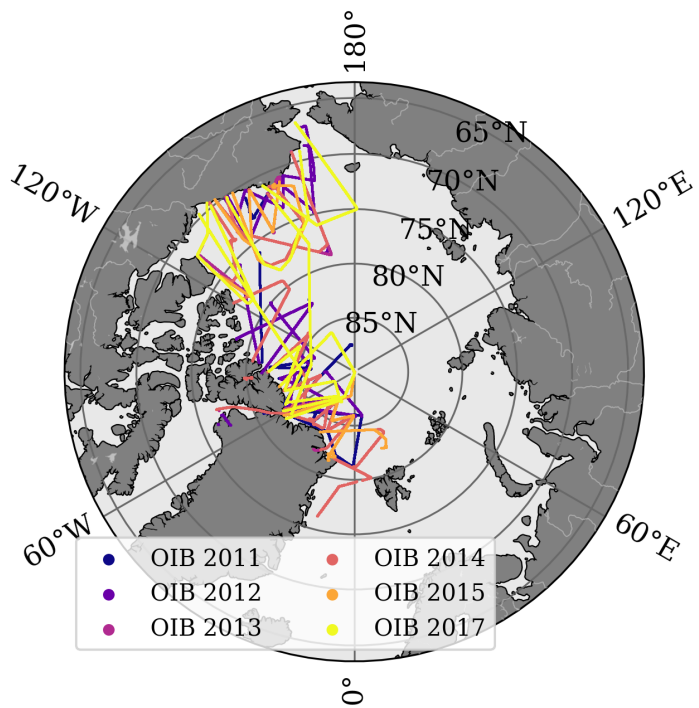


Figure 3.4: March flight paths from NASA’s Operation IceBridge (OIB) missions from 2011 to 2017, excluding 2016. From 2014 to 2017 flight paths indicate where the quick look (QL) data were collected.

3.4 Baufort Gyre Exploration Project

The Beaufort Gyre Exploration Project has deployed a series of moorings equipped with upward-looking sonars (ULS), operating at 420 kHz and directed upward to sample a footprint of approximately 2 m from a depth of around 50 m beneath the Artic ice pack in the Beaufort Gyre ocean current, beginning in 2003. The moorings were deployed in waters exceeding 3500 m in depth, with ULS positioned between 50 and 85 m beneath the sea ice cover. These ULS instruments provide range measurements at two-second intervals, which in the processed data yield estimates of the sea ice draft. Over the course of a year, each mooring generates more than 15 million observations, producing a high-resolution SID time series with daily coverage. The movement of sea ice allows the instrument to sample a wide range of ice conditions over time, providing a representative overview of regional sea ice thickness distributions (Krishfield and Proshutinsky, 2006; Sallila et al.,

2019). The locations of the three moorings utilized in this study, positioned at distinct sites (A, B, and D) within the Beaufort Gyre ocean current, are shown in Figure 3.5.

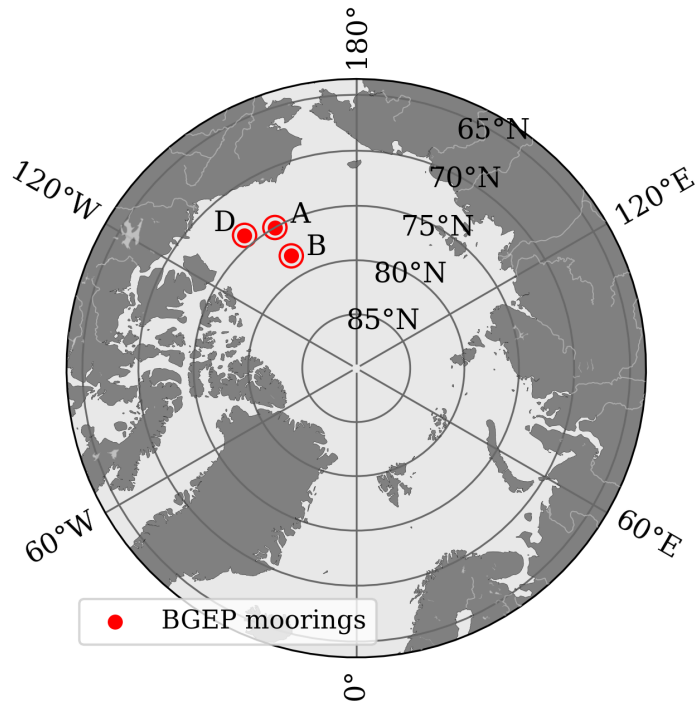


Figure 3.5: Beaufort Gyre Exploration Project (BGEP) mooring A, B, and C locations.

3.5 SMOSice Campaign

SMOSice was an airborne and ship-based field campaign conducted by the European Space Agency from the 23rd to 26th March 2014 in the Barents Sea, aimed at collecting snow and sea ice data over thin sea ice. The primary objective of the Campaign was to improve the SMOS SIT retrieval algorithm. A range of instruments were deployed, including an airborne laser scanner (ALS), a helicopter-borne electromagnetic bird (EM-bird), a radiometer, and a snow radar, although the latter experienced a malfunction during the campaign. The ALS, mounted on the Polar-5 aircraft, performs linear scans in the near-infrared spectrum, providing sea ice freeboard and surface roughness estimates with a ground resolution of approximately 30 cm (at 60 meters altitude) and a vertical accuracy of 2.5 cm. The ALS was flown twice on 20 March, aligning

with the CryoSat ground tracks (Hendricks et al., 2015). The helicopter-borne EM-bird (HEM), equipped with an additional laser altimeter, estimates SIT by exploiting the contrast in electrical conductivity between sea ice and sea water. The HEM system was operated at an altitude of approximately 15 m above the sea ice surface, providing SIT measurements every 3 to 4 m along the flight path, with a footprint of roughly 50 m. In total, eight flights were conducted using the HEM system. Over level ice, the SIT retrieval accuracy is approximately ± 0.1 m (Haas et al., 2009; Hendricks et al., 2015). The flight paths conducted with the ALS and HEM system can be seen in Figure 3.6.

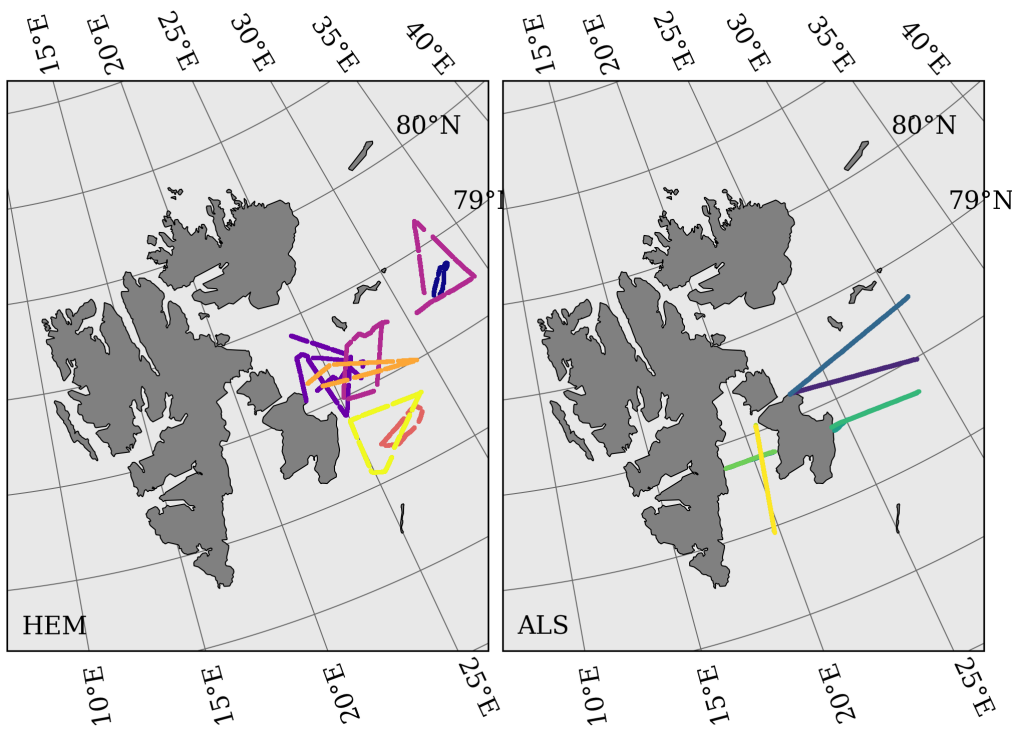


Figure 3.6: Left figure shows the flight paths of the helicopter-borne EM-bird (HEM), while the right figure presents the flight paths conducted using the Airborne laser scanner (ALS).

4

Data sets & Processing

4.1 Sea Ice Thickness Satellite Products

4.1.1 SMOS AWI Product

SMOS AWI product, developed by the Alfred Wegener Institute Helmholtz Center for Polar and Marine Research. This product utilizes the L-band (1.4 GHz) brightness temperatures measured by the SMOS satellite to derive the thickness of thin sea ice, typically up to 0.5 m or 1 m under ideal cold conditions (Tian-Kunze et al., 2014; Ricker et al., 2017). The dataset provides daily temporal resolution with a spatial resolution of 12.5 km, with operational production beginning in 2010. It covers the months from October to April each year (Zhang et al., 2024; Tian-Kunze et al., 2014).

The retrieval of SIT in the Level 3c processing of the SMOS AWI product begins with the input of SMOS v724 Level 1c brightness temperature data, which includes all four Stokes parameters (Tian-Kunze et al., 2014). In the processing, the ice cover is assumed to be homogeneous (i.e., 100% coverage), such that sea ice emissivity becomes primarily a function of ice thickness, temperature, and salinity. The so-called Sea Ice Thickness Algorithm II is employed to perform the retrieval. This algorithm is based on a thermodynamic sea ice model with a three-layer radiative transfer model, allowing it to account for variations in both ice temperature and salinity (Tian-Kunze et al., 2014, 2023).

The algorithm estimates sea ice thickness iteratively by calculating ice temperature and salinity for each thickness estimate using thermodynamic models and Sea Surface Salinity (SSS) climatology. A radiative transfer model then calculates the corresponding brightness temperature, which is compared to the SMOS observations and refined until convergence is reached, defined by a brightness temperature difference below 0.1 K or an ice thickness difference below 1 cm (Tian-Kunze et al., 2014; Wang et al., 2016). To account for SIT variations and the presence of open water within the SMOS spatial resolution, a correction is applied using a statistical thickness distribution function derived from high-resolution measurements from NASA OIB QL data. This enhanced processing approach is referred to as Algorithm II* (Tian-Kunze et al., 2014, 2023).

Under ideal conditions, the maximum retrievable SIT is estimated to be approximately 1 m. The average uncertainty introduced by the thickness distribution function is less than 10 cm and is combined with the additional uncertainties arising from brightness temperature, ice temperature, and salinity (Tian-Kunze et al., 2014). SMOS SIT retrieval shows lower uncertainty for ice thickness below 0.5 m, with increasing uncertainty for thickness between 0.5 and 1 m. For ice thicker than 0.5-1 m, uncertainty increases exponentially (Tian-Kunze et al., 2014; Ricker et al., 2017). For the purpose of this study, version 3.3 of the daily SMOS SIT dataset, released in 2021, was utilized (Tian-Kunze et al., 2023). Undefined sea ice thickness estimates are represented by a placeholder value of -999.0, and a binary land mask is used to exclude land areas from the dataset.

4.1.2 CryoSat-2 UiT Product

The CryoSat UiT product, developed by the Earth Observation Group at UiT, the Arctic University of Norway, incorporates a new retracking algorithm, the Lognormal Altimeter Retracker Model (Landy et al., 2020), along with a refined snow model, the Lagrangian snow-evolution model (Liston et al., 2020), aimed to enhance the accuracy of sea ice thickness estimates. The product offers monthly data coverage from October to April, with archived records available from October 2010 onward. It includes a range of geophysical variables such as sea ice thickness, freeboard, and volume, along with various snow-related parameters, each accompanied by corresponding uncertainty estimates. In addition, the product provides sea ice variables using the LARM algorithm in combination with a modified Warren 1999 climatology (modified to reduce snow depth by 50% over FYI, which is now a standard practice) (Warren et al., 1999). All variables are gridded to the 25 km Equal-Area Scalable Earth (EASE)

grid.

The CryoSat CPOM (Tilling et al., 2018) and AWI (Hendricks et al., 2021) products, which apply variations of the TFMRA, the method assumes a Gaussian surface height distribution and accounts for surface variability indirectly through changes in the waveform shape. While TFMRA is computationally efficient, easy to implement, and robust against noisy real-world waveforms (Quartly et al., 2019). It has been demonstrated that variations in ice surface roughness can introduce systematic retracking-related uncertainties in sea ice thickness retrieval of up to 20% over FYI and 30% over MYI. LARM is based on a lognormal distribution of sea ice surface topography, allowing the power threshold to vary dynamically in response to local sea ice conditions, which aims to account for surface roughness in the range estimate. Although significantly slower and more complex than TFMRA, LARM may offer distinct advantages under sea ice conditions that deviate from the mean state, particularly for thin, newly forming ice with very low surface roughness (Landy et al., 2020).

The UiT product processing utilizes radar waveforms from the Baseline-E L1B data provided by ESA. LARM simulates the CryoSat waveforms with a physical model for the SAR altimeter echo backscatter. This model, described in Landy et al. (2019), creates ideal radar waveforms from prescribed rough ice surfaces for comparison against the observed CryoSat data. These surfaces can follow either a Gaussian or lognormal distribution of heights. To efficiently compare the simulated echoes with the observed waveforms, LARM uses a lookup table of 2222 simulated echoes that is built by varying roughness parameters. An optimization algorithm fits these simulated waveforms to the observed waveforms, which is done by minimizing the four free parameters, including the epoch (retracking point) and surface roughness. It has been shown that using a lognormal model results in significantly more variation in the retracted range estimate compared to simulations based on a Gaussian model. For lognormal echoes, the retracking point is expected to range from around 95% for smooth, newly formed ice to approximately 60% for heavily deformed ice with surface roughness greater than 50 cm. Leads are expected to have a retracking threshold of approximately 98%. So, for adjacent lead and ice floe sampled with no error, this corresponds to a theoretically minimum detectable freeboard of around 2.5 cm, which corresponds to an ice thickness of about 0.25 m in the absence of snow (Landy et al., 2020).

For the conversion of LARM-derived radar freeboard to sea ice thickness, the product utilizes snow depth and density information provided by SnowModel-LG. This is a snow evolution model that simulates the development of snow on sea ice using atmospheric forcing as input. In this case, snow depth and density are derived from SnowModel-LG using atmospheric reanalysis data

from both MERRA-2 (McCarty et al., 2016) and ERA-5 (Hersbach et al., 2020), which are averaged to represent the final snow depth and density. SIT is then calculated on the principle of hydrostatic equilibrium. This study utilizes the most recent version of the UiT product, Baseline-E. Undefined sea ice thickness estimates in the dataset are indicated by *Nan*.

4.1.3 CryoSat-2 CPOM Product

The Centre for Polar Observation and Modelling sea ice processing procedure has been in constant development since the 1990s and was the first publicly available estimates of arctic sea ice thickness and volume using CryoSat radar altimeter data (Tilling et al., 2018). Additionally, it provides a Near-real-time (NRT) product that is available 2, 14, and 28 days of each month with 3 days of acquisition, the percentage of sea ice covered by the NRT is dependent on the CryoSat orbit but has an average measurement within 14, 7, and 6 km of each location (Tilling et al., 2016). CPOM has a temporal range from November 2010 to the present, providing coverage of the northern hemisphere, with sea ice thickness data estimates available from October to April on a 5 km square Polar Stereographic grid (Tilling et al., 2018).

The sea ice thickness and volume processing method starts with the CryoSat waveforms from the Baseline-C L1B data delivered by ESA, for ice floe and leads identification (Tilling et al., 2018). To discriminate between ice floe and leads, the process discriminates between ocean surface and ice surface measurements by identifying which echoes are specular and which are diffuse. To identify specular and diffuse echoes, they are separated by using stacked standard deviation (SSD) and the pulse peakiness, where ice floes give diffuse echoes and are identified where the sea ice concentrations are greater than 75%, and open water is the regions with 0% concentration (Tilling et al., 2018). The CPOM algorithm also takes in the information on the sea ice edge location and the sea ice type as FYI and MYI. Here, the sea ice edge location is retrieved from the process mentioned above, and the definition of ice type is done through the use of ice type data from the Norwegian Meteorological Service (NMS) and Ocean and Sea Ice Satellite Application Facility (OSI SAF) (Tilling et al., 2018). Estimations of snow depth and density on sea ice are based on the Warren 1999 climatology (Warren et al., 1999), where the snow depth over FYI is half of the snow depth for MYI. The algorithm goes so forward to waveform retracking, where retracking of diffuse echo uses a tracking point that is defined when the leading edge of the echo rise reaches 70% of the amplitude of its initial peak hence the sea ice surface height corresponds to the 70% of the amplitude on the leading edge (Tilling

et al., 2018). The Giles retracking method (Giles et al., 2007) is applied to specular echoes from leads for lead height estimations, where a Gaussian plus exponential model is fitted to the waveforms (Tilling et al., 2016; Sallila et al., 2019). A constant offset of around 16 cm is applied to align the elevations from the leads and ice floes, retracted with the two different methods. In the calculation of sea ice and ocean elevations, the algorithm utilizes the WGS84 reference ellipsoid, and corrections given in the CryoSat L1B product are taken into account (that are dry tropospheric, wet tropospheric, inverse barometric, modeled ionospheric, ocean tide, long-period equilibrium tide, ocean loading tide, solid earth tide, and geocentric polar tide) (Tilling et al., 2018). Additionally, for sea ice freeboard calculations, the University College London 2013 (UCL13) mean sea surface (MSS) model is used to compute sea surface height anomalies and mitigate the influence of geoid slope on freeboard estimates. Missing values for sea ice thickness are represented by 0.0000, these values are identified and removed during preprocessing.

4.1.4 CryoSat-2 AWI Product

CryoSat AWI product, introduced by the Alfred Wegener Institute Helmholtz Center for Polar and Marine Research. The product provides a monthly temporal resolution spanning from October to April, and with archived data starting from October 2010. Where the data gives a range of geophysical parameters, such as sea ice thickness, ice freeboard, and snow depth, in addition to sea ice thickness and freeboard uncertainties. Where all parameters are on a 25 km grid, covering the whole Arctic (Hendricks et al., 2021).

The processing starts with the CryoSat waveforms from the Baseline-C L1B data delivered by ESA. The AWI algorithm utilizes the OSI SAF products for classifying sea ice type and concentration, identifying the ice edge where sea ice concentration surpasses 70% as a valid region for lead and sea ice detection. For the calculation of surface elevation, AWI uses an implementation of a 50% TFMRA (Ricker et al., 2014). Additionally, surface elevation calculations incorporate the geophysical range corrections from the CryoSat L1b product and reference the WGS84 ellipsoid. In sea surface height calculations, the AWI algorithm currently relies on the DTU21 MSS model to derive sea surface anomalies, whereas the CPOM product utilizes the UCL13 model for this purpose. Accurate sea ice thickness retrieval depends significantly on snow cover data. In this context, the AWI merges data from the Warren 1999 climatology with AMSR2-derived snow depth estimates over first-year sea ice provided by the Institute for Environmental Physics at the University of Bremen (IUP) (Hendricks et al., 2021). Over FYI, the values for Warren 1999 climatology are

reduced by 50%, and the snow density is a linear increasing snow depth for the corresponding month during the winter season is applied. The analysis utilizes CryoSat AWI version 2.6 product.

4.2 Validation data sets

4.2.1 Operation IceBridge

Accurate snow depth measurements are obtained using the frequency-modulated continuous-wave (FMCW) snow radar. Additionally, snow thickness over sea ice can be determined by combining data from the ATM and the Ku-band radar altimeter (Kurtz et al., 2013; Lemmens, 2015). From the snow radar, the snow thickness estimation relies on an empirical algorithm that selects the air-to-snow interface based on a combination of peak detection and threshold methods (Kwok et al., 2017). Where the sea ice freeboard is defined as the combined height of the snow layer and the sea ice surface, enabling consistency with measurements obtained from the laser altimeter ATM. For the retrieval process, surface elevation is referenced to the WGS84 ellipsoid, and local sea ice surface is determined from leads identified using aerial imagery from the DMS. Additionally, for lead identification and to correct for undersampling over thin sea ice and narrow leads, adjustments are applied using information from the Sea Ice Lead Detection algorithm using Minimal Signal (SILDAMS) (Kurtz et al., 2012). Following the retrieval of freeboard, sea ice thickness is computed based on the principle of hydrostatic equilibrium (Kurtz et al., 2013). The approach used to compute sea ice thickness in the QL product is, in many respects, similar to that of the fully processed OIB data. However, to reduce processing time, the QL product excludes the use of DMS imagery and the SILDAMS algorithm for lead identification. Instead, the KT19 surface temperature sensor is employed to identify leads. For datasets acquired after 2015, DMS data are reintroduced, using a lead detection method similar to the SILDAMS approach. In addition, the snow radar data in the QL product are processed using a waveform fitting procedure, analogous to the method used for CryoSat retrievals described in Kurtz et al. (2014), replacing the earlier empirical technique. While these modifications significantly reduce processing time, they introduce additional uncertainties in the QL product that should be taken into consideration.

Due to the flight paths of the OIB mission (see Figure 3.4), it primarily covered areas that are characterized by the presence of thick MYI, which is evident in the histogram in Figure 4.1. In this study, the OIB IDCS14 product is used for

the months of March 2011, March 2012, and March 2013, while additional data for March 2014, 2015, and 2017 are obtained from the OIB QL product. The selection of the earlier years is based on the availability of corresponding archived CryoSat data for comparative analysis. The later years from the QL product are chosen based on data availability, with preference given to periods with the most extensive spatial and temporal coverage in March. Missing values in the dataset, indicated by -99999.0, are removed during the preprocessing stage.

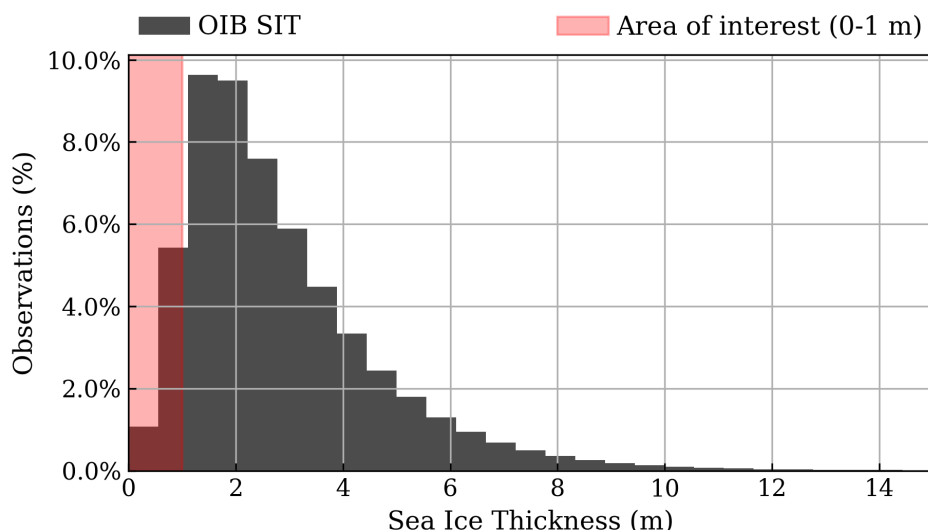


Figure 4.1: Histogram showing the percentage distribution of sea ice thickness measurements derived from the OIB IDCS14 and QL products, with observations masked to reflect the specific area of interest used in this study.

4.2.2 Beaufort Gyre Exploration Project

To accurately measure SID, the ULS instruments rely on the natural drift of ice floes and leads of the moorings to determine the local sea surface level (Krishfield and Proshutinsky, 2006; Sallila et al., 2019). SID is calculated by subtracting the range measurements (water level) recorded by the ULS from the depth obtained via the pressure transducer, with adjustments made for instrument tilt. Additionally, a beta correction is applied to account for changes in seawater temperature and salinity. This method provides SID estimates with an accuracy of approximately ± 0.5 m (Krishfield and Proshutinsky, 2006). To convert SIT to SID, this study employs the method described in Rothrock et al. (2008), which is based on the principle of hydrostatic equilibrium and incorpo-

rates the Warren 1999 climatology (Warren et al., 1999). This approach yields an average SID-to-SIT of 0.93. While this method introduces uncertainties to the converted SID values, these are considered acceptable within the context of this study. For this analysis, data from the months of October through April are used, covering the period from 2010 to 2022. These months represent the time of year with the highest occurrence of thin sea ice, as illustrated by the sea ice draft distribution for mooring A in the histogram shown in Figure 4.2.

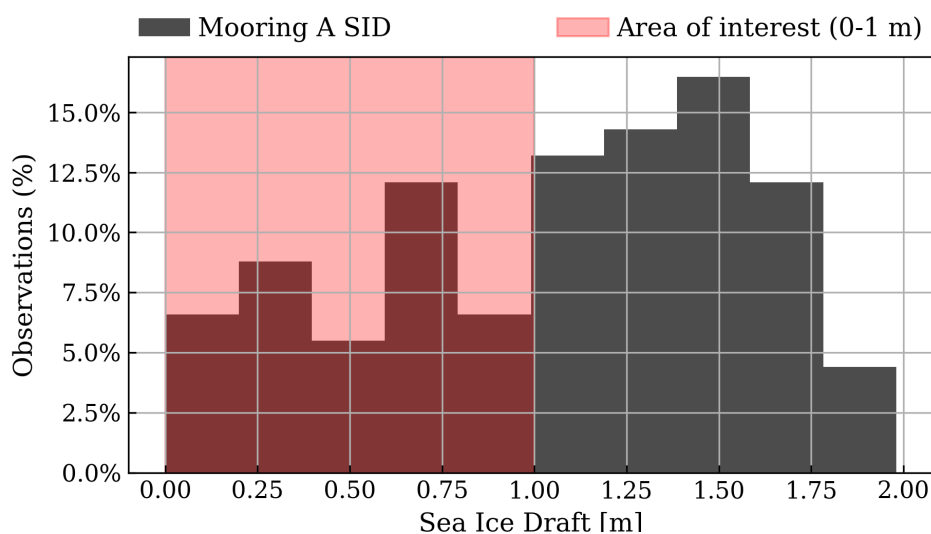


Figure 4.2: Sea ice draft distribution at BGEP mooring A for the months October to April between 2010 and 2022. The masked region highlights the area of interest in this study.

4.2.3 SMOSice Campaign

Sea ice freeboard, commonly referred to as snow freeboard or total freeboard, is defined in this context as the combined height of the snow layer and the sea ice surface, as the ALS primarily reflects off the snow surface, and is retrieved from ALS measurements through two processing steps. First, is the use of the aircraft GPS/INS data for position and attitude along with laser range measurements, to compute the surface elevations relative to the WGS84 ellipsoid. In the second step, these elevations are referenced to the local sea surface height, which is manually identified in lead and interpolated along the flight path. Total freeboard is then calculated by subtracting the SSH from the surface elevation (Hendricks et al., 2015). The total SIT, which includes both

snow and ice, is determined by utilizing the difference in electrical conductivity between sea ice and sea water measured by the HEM system. The system combines two measurements. First, the laser altimeter measures the height of the instrument above the ice surface. Second, the EM component derived the height above the sea water interface using a model curve for known sea water conductivity (Haas et al., 2009; Haas, 1998). This model represents the expected EM response over open water and serves as a reference for determining the ice underside. tSIT is calculated as the difference between the EM-derived height above the water and the laser-measured height above the ice surface, assuming negligible sea ice conductivity and known sea water conductivity. This approach retrieves the thickness of the layer between the snow surface and the sea ice underside (Haas et al., 2009).

/ 5

Method

In this study, four separate analyses are conducted. First, CryoSat products are compared against the SMOS AWI sea ice thickness product, the method is described in Section 5.3. Second, both CryoSat UiT and SMOS AWI products are evaluated against the airborne sea ice thickness estimates from the NASA OIB mission in Section 5.4. Third, the CryoSat UiT and SMOS AWI products are compared to sea ice thickness data obtained from moorings deployed as part of the BGEP in Section 5.5. Lastly, these same satellite products are assessed against sea ice thickness and sea ice draft measurements from the SMOSice field campaign, where this method is described in Section 5.6. Throughout the sections, the SMOS AWI product is referred to as the SMOS product.

5.1 Resampling

The geospatial coordinates from the datasets are projected into the North Polar Stereographic coordinate system, with the projection plane tangential to the Earth's surface at 70°N/S (Knowles, 2001). The datasets with a higher spatial resolution (e.g., SMOS AWI with a spatial resolution of 12.5 km) are resampled to a 25 km grid to match the resolution of the CryoSat UiT product. This resampling step is applied uniformly across all datasets for

consistency. The resampling procedure is based on an inverse uncertainty weighting method, where each source point i contributes to the target grid cell with a weight defined as:

$$w_i = \frac{1}{\sigma_i} \quad (5.1)$$

here, σ_i represents the uncertainty associated with the source point. The value assigned to each 25 km (from the CryoSat UiT product) grid cell is then computed as the inverse-uncertainty weighted mean of all n source points that fall within the defined grid cell size. The weighted average \bar{h} is calculated as:

$$\bar{h} = \frac{\sum_i h_i w_i}{\sum_i w_i} = \frac{\sum_i \frac{1}{\sigma_i} h_i}{\sum_i \frac{1}{\sigma_i}} \quad (5.2)$$

where h_i is the source sea ice thickness value, this ensures that data points with lower uncertainty have a greater influence on the final gridded estimate (Papasaika-Hanusch, 2012).

5.2 Statistical Methods for Assessment

Comparisons and validation efforts throughout this study rely on three standard statistical indicators: bias, root mean square error (RMSE), and the Pearson correlation coefficient (CC). Additional metrics are presented where necessary for specific analysis. Bias captures the mean difference between the satellite products and reference data. RMSE provides a measure of the overall deviation between the two, while CC evaluates how strongly and consistently the two datasets are linearly related. These statistical metrics offer valuable insight into different aspects of data quality. To provide a more comprehensive evaluation of satellite product performance relative to a reference dataset, the analysis also incorporates the Distance between Indices of Simulation and Observation (DISO). This aggregated index accounts for bias, RMSE, and the CC, offering an overall performance score where lower DISO values indicate better agreement. Each of the two component metrics is normalized to a [0, 1] scale using Equation 5.3, seen below.

$$NM_i = \frac{M_i - \min(M)}{\max(M) - \min(M)} \quad (5.3)$$

Where M represents the metric being normalized, $i = 0, 1, \dots, m$, and m is the total number of satellite products. The normalized metrics are then used to compute the DISO, defined as:

$$DISO_i = \sqrt{NBias_i^2 + NRMSE_i^2 + (CC_i - 1)^2} \quad (5.4)$$

Here, $NBias$ and $NRMSE$ denote the normalized values of bias and RMSE, respectively, while CC is not normalized due to its natural range between -1 and 1 . For the case $i = 0$, which corresponds to the comparison of a satellite product with itself, the values are $NBias = 0$, $NRMSE = 0$, and $CC = 1$ (Hu et al., 2022; Zhang et al., 2024).

5.3 Comparison of CryoSat Products Against SMOS AWI

In the intercomparison between CryoSat products and the SMOS AWI product, four CryoSat-derived sea ice thickness products named UiT, W99, CPOM, and AWI are evaluated against the SMOS AWI product. Where the W99 product refers to the UiT product combining the LARM algorithm with a modified Warren 1999 climatology. This comparison aims to highlight the influence of different snow climatology models and retrieval algorithms, particularly in the thin ice regime. For the purpose of this analysis, the SMOS AWI product is treated as the reference dataset, as it is widely acknowledged within the scientific community that SMOS provides more accurate estimates in the thin sea ice regime.

The comparison is based on data from October, November, and December of 2021, representing the early winter season, when a higher proportion of thin sea ice is typically present. From the dataset, latitude, longitude, sea ice thickness, and sea ice thickness uncertainty are loaded. In the first step of the analysis, all CryoSat products are loaded, and missing values are removed. For the UiT and W99 products, missing values are identified as NaN , while for the CPOM product, missing values are indicated by a value of 0.0000 . For the SMOS product, sea ice thickness values flagged as missing by the value -999.0 are removed, and the land mask is applied to the daily data. The SMOS mean of the daily sea ice thickness and associated uncertainty is then calculated to generate monthly coverage, which is stored in a NetCDF file while preserving the original variable dimensions. All products are subsequently resampled onto the CryoSat UiT grid (25 km) to ensure consistency, following

the approach described in Section 5.1. Four figures are presented to assess the performance in the thin sea ice range (0-1m), with the combined data of the months. These include a differential SIT map, a bar histogram plot, a scatter box plot, and a mean difference heatmap. The method involves selecting SMOS AWI grid cells with a thickness below 1 m and retrieving the corresponding values from the CryoSat values. To quantify performance, the bias, CC, and RMSE are calculated across the intervals 0.0 – 0.4 m and 0.4 – 1 m, following the methodology described in 5.2. Independent plots for each month, along with statistical metrics computed over the finer SIT intervals of 0 – 0.2 m, 0.2 – 0.4 m, 0.4 – 0.6 m, 0.6 – 0.8 m, and 0.8 – 1 m, are provided in Appendix Section A.1.

5.4 Validation Against OIB Airborne Observations

For the validation against the OIB airborne observation data, including the QL product, the dataset is collectively referred to as the OIB data. The CryoSat Ut and SMOS products are used for comparison, covering March from 2011 to 2017, excluding 2016. Due to the limited availability of thin sea ice observations and incomplete daily coverage, all OIB observations are combined after filtering out missing values indicated by -99999.0. The SMOS data is processed into a monthly dataset as outlined in Section 5.3. For validation, both sea ice thickness and uncertainty values are used, where the uncertainty is applied in the resampling procedure described in Section 5.1. A SIT range mask of 0 – 1 m is applied to the OIB data to extract corresponding SIT estimates from the Ut and SMOS datasets. Since the SMOS product is limited to a maximum SIT of 1 m, both SMOS and Ut data are constrained to this upper bound to ensure a fair comparison. The comparison is illustrated through a bar histogram, a box scatter plot, and a mean difference heatmap. Bias, RMSE, CC, and DISO are also presented across predefined SIT intervals of 0.0 – 0.4 m and 0.4 – 1 m, following the methodology described in Section 5.2. The bar histogram and box scatter plot without the SIT range constraint, along with the statistical metrics computed over the SIT intervals of 0 – 0.2 m, 0.2 – 0.4 m, 0.4 – 0.6 m, 0.6 – 0.8 m, and 0.8 – 1 m, are provided in Appendix Section A.2.

5.5 Validation Against BGEP Mooring Data

Validation against the BGEP mooring data is conducted using the CryoSat UiT and SMOS SIT products to compare their relative performance. The analysis spans the months from October to April for the years 2010 to 2022. While the BGEP data provided high-temporal-resolution measurements (approximately every 2 seconds), these are averaged first to a daily scale and then to a monthly scale to align with the temporal resolution of the satellite products. Similarly, the SMOS data is processed into monthly means, as described in Section 5.3. All datasets are projected onto the North Polar Stereographic coordinate system. However, the resampling procedure described in Section 5.1 and used in the previous method sections is not applied in this validation analysis. Since the BGEP data provides estimates of SID, the SIT products from UiT and SMOS are converted to SID for direct comparison. For the UiT product, SID is derived by subtracting the ice freeboard from the SIT, accordingly:

$$SIT - iFB = SID \quad (5.5)$$

In the case of SMOS, where iFB data is unavailable, a constant SIT-to-SID ratio of 0.93 is applied to estimate SID:

$$SIT \cdot 0.93 = SID \quad (5.6)$$

A 200 km radius is established around each mooring location to facilitate a consistent comparison, from which satellite grid cells are extracted and averaged. For the validation and comparison of the datasets, the time series of the SID are used for each of the moorings, and the corresponding SID estimates from the satellite products are used. In the case of the SMOS dataset, if more than 40% of these grid cells report SID values exceeding 1 m, the data is classified as *Saturated SMOS*, indicating limitations in the upper-range sensitivity of the SMOS SIT retrievals. A pairwise scatter plot is created using the combined dataset from all mooring locations compared with the SID estimate from the satellite products. To account for seasonal effects, these plots are reproduced using seasonal anomalies, which are derived by subtracting the monthly climatology from the original datasets. A filter is applied to include only SID values between 0 and 1 m for both mooring and satellite data. Bar histograms are presented as a comparison between the mooring and satellite SID estimates, with this range restriction. In addition, statistical metrics including bias, RMSE, CC, and DISO are computed across predefined SID intervals of 0.0 – 0.4 m and 0.4 – 1 m, following the approach detailed in Section 5.2. Appendix Section A.3 includes the pairwise scatter plot of both raw and seasonal anomalies for each mooring site, the bar distribution

plot without the 0–1 SID constraint, and the statistical metrics calculated across the SID intervals of 0 – 0.2 m, 0.2 – 0.4 m, 0.4 – 0.6 m, 0.6 – 0.8 m, and 0.8 – 1 m.

5.6 Validation Against SMOSice Campaign Measurements

The validation against the SMOSice campaign measurements is performed using the CryoSat UiT and SMOS products. ALS data from the 24th and 26th of March and HEM data collected between the 19th and 26th of March are used in the analysis. In total, four comparisons are conducted between the UiT, SMOS, and SMOSice datasets.

The first two comparisons utilize the tSIT data from the HEM system. In these comparisons, the SIT data from both the UiT and SMOS products, in addition to the HEM data, are projected onto the North Polar Stereographic coordinate system. The SMOS dataset is processed into monthly means, as outlined in Section 5.3. For both cases, raw sampled HEM tSIT measurements and resampled measurements on the UiT grid are used. The SMOS data are likewise resampled onto the same grid, following the procedure described in Section 5.1. Since the UiT and SMOS L3 datasets provide only SIT, snow depth estimates from SnowModel-LG, which are included in the UiT product, are used to compute the tSIT as follows:

$$tSIT = SIT + SD \quad (5.7)$$

The following analysis incorporates ALS tFB measurements from March 26, which align with the CryoSat ground track. Therefore, UiT L2 trajectory data Baseline E product is used, providing rFB. To convert the UiT rFB to tFB, snow depth estimates from SnowModel-LG are sampled onto the rFB locations. This follows the same procedure as outlined in Equation 5.7 for calculating tSIT. The final analysis includes ALS tFB measurements from March 24 and daily SMOS SIT data from the same day to ensure comparability with previous analysis. The conversion from tFB to SIT follows the method described in Hendricks et al. (2015), where tFB is multiplied by a factor of 5.5:

$$SIT = tFB \cdot 5.5 \quad (5.8)$$

This conversion produces SIT values comparable to those obtained from the HEM system and is considered acceptable within the context of this study, as it

does not significantly deviate from the HEM observations, as shown in Figure 5.1. Only SMOS data points overlapping with ALS measurement locations are included in the comparison.

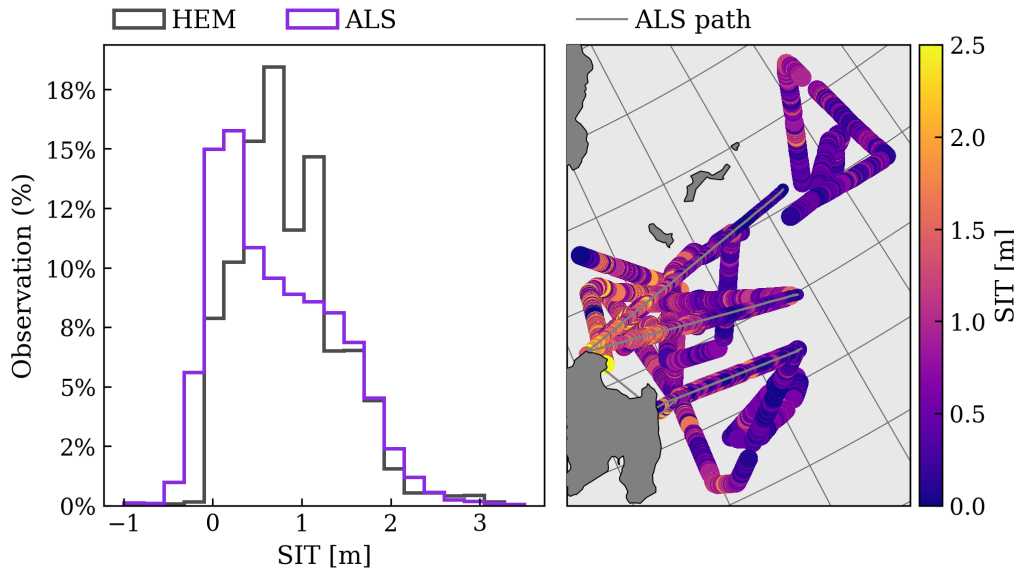


Figure 5.1: Left panel shows the distribution of SIT derived from ALS measurements compared with HEM SIT measurements. Right panel presents the spatial distribution of ALS and HEM SIT estimates in the region offshore of Svalbard.

All analyses in this comparison are based on evaluating the thickness distributions from satellite products, HEM, and ALS observations. For each case, additional statistical metrics are computed, including the mean, bias, RMSE, CC, and DISO, following the methodology described in Section 5.2. In the final analysis, statistical calculations are restricted to SIT values between 0 and 1 m for both SMOS and ALS datasets, reflecting the upper measurement limit of the SMOS product. It should be noted that using the SnowModel-LG to derive tSIT and tFB introduces its own uncertainties, which may be significant. Additionally, the spatial distribution plots and corresponding histograms of the ungridded HEM and SMOS measurements are provided, along with statistical metrics computed in 0.2 m intervals over the 0-1 m range for the HEM and ALS tFB comparisons. These supplementary materials can be found in Appendix Section A.4.

/ 6

Results

The following sections present the results from the four analyses, along with descriptions of the obtained figures. Throughout these sections, the SMOS AWI product is referred to simply as the SMOS product.

6.1 Comparison of CryoSat Products Against SMOS AWI

Figure 6.1 presents a spatial map of SIT differences (ΔSIT) between the CryoSat products and the SMOS reference product. The UiT product shows slight underestimation in the northern part of the domain, while overestimation is observed in the thin ice region near Svalbard. The W99 product, which shares the same retracking method as the UiT product but incorporates the Warren 1999 climatology, demonstrates reduced overestimation in the Svalbard region but exhibits more pronounced overestimation in the Canadian sector. The AWI product displays a more heterogeneous pattern, with both over- and underestimation across different regions, similar to the UiT product. Notably, it also shows increased overestimation in the thin sea ice area near Svalbard. The CPOM product consistently shows the largest SIT difference across the

ice sheet, with overall higher values compared to the SMOS estimates.

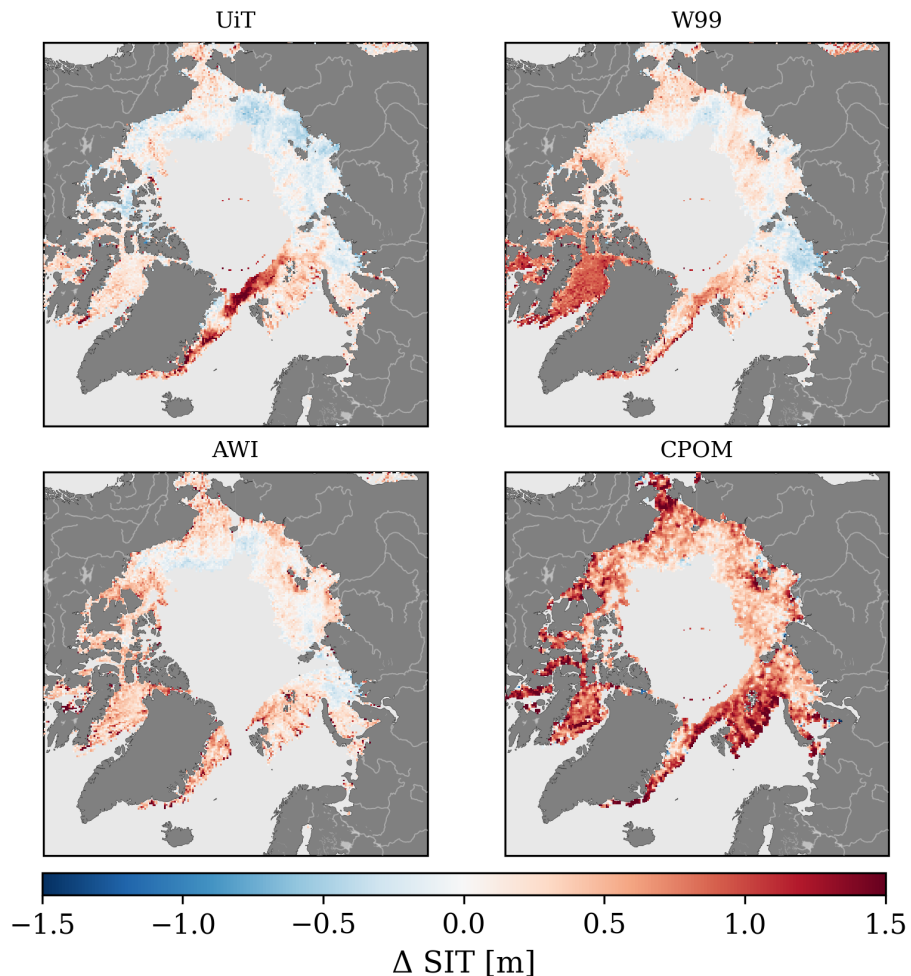


Figure 6.1: Map of sea ice thickness (SIT) difference (ΔSIT) between the CryoSat products and the SMOS AWI reference dataset.

Figure 6.2 presents the mean SIT from the CryoSat products as a function of SMOS SIT bins. The lower panels display corresponding distribution plots, with the SMOS SIT distribution shown in the background for reference. Across all products, the mean SIT exceeds the SMOS SIT value in bins up to 0.6 m. Among the products, the UiT dataset shows consistently lower mean SIT values, closer to the SMOS reference, particularly in the thinner ice regime. In contrast, the CPOM exhibits the highest overall mean SIT and deviates significantly from the SMOS reference in all bins. The W99 and AWI products

show a similar rate of increase in mean SIT with increasing SMOS bin values. In terms of distribution, the UiT product has the highest number of observations within the thin sea ice range, and its distribution closely resembles that of SMOS. Other products, including AWI, W99, and CPOM, exhibit a greater skew toward thicker ice. Notably, CPOM displays a near-linear increase in count with increasing SIT, further highlighting its bias toward higher thickness values.

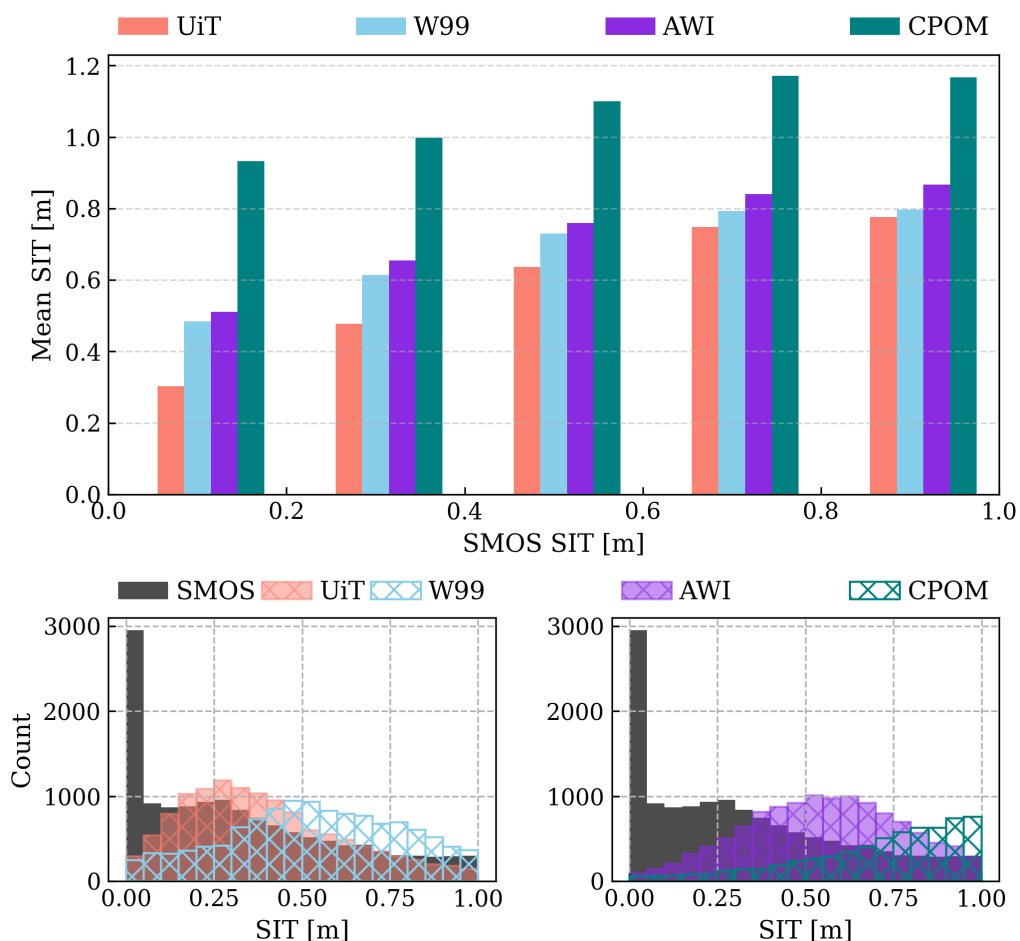


Figure 6.2: Mean sea ice thickness (SIT) bar plot and corresponding distribution plots comparing CryoSat products with the SMOS AWI product.

To facilitate a clearer comparison of the CryoSat products SIT estimates relative to the SMOS SIT values, a heat map of the mean SIT difference is presented in Figure 6.3. The UiT product shows the closest overall agreement with the SMOS

reference, particularly in the thinner ice range. As also observed in Figure 6.2, the W99 and AWI products display similar behavior, with increasing agreement as SIT values rise. In contrast, the CPOM product consistently exhibits the highest deviations from the SMOS SIT estimates across all bins. A consistent trend in all products is that the SIT difference decreases as the SMOS SIT bins increase. Among the products, the AWI dataset shows the best agreement with SMOS in the highest thickness bin, followed by the W99 product.

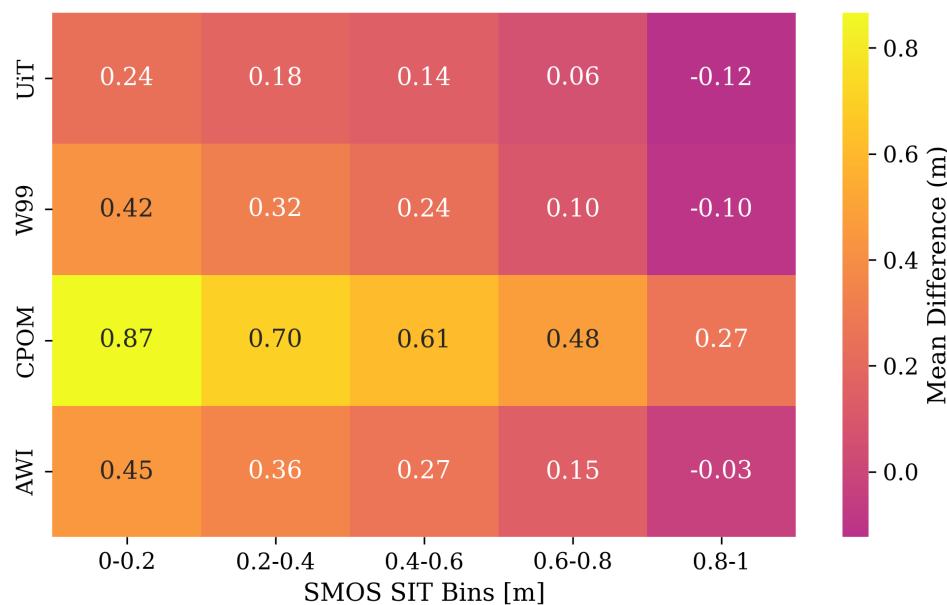


Figure 6.3: Heat map displaying the mean sea ice thickness (SIT) differences between each CryoSat product.

Figure 6.4 presents a box scatter plot comparing the CryoSat product SIT estimates as a function of binned SMOS SIT values. The products generally exhibit similar behavior to that observed in previous analyses. The UiT product demonstrates the strongest overall agreement with the SMOS SIT values, with its median falling within all SMOS SIT bins. However, in the highest thickness bin, the UiT product also shows a relatively larger interquartile range compared to the W99 and AWI, which both display a narrower spread. The W99 and AWI products only show median values within the SMOS bin range in the final two thickness bins. Specifically, the UiT product returns median SIT values of approximately 0.20 m for the 0.0-0.2 m bin, 0.38 m for the 0.2-0.4 m bin, and 0.51 m for the 0.4-0.6 m bin, falling close to the midpoints for the following SMOS SIT bins. While the W99 and AWI products also fall within the

SMOS range in the highest bins, they tend to overestimate median SIT in the intermediate bins and slightly underestimate in the highest bin. In contrast, the CPOM product consistently overestimates SIT across all SMOS bins and shows broader scatter in its distribution. W99 and AWI also demonstrate less spread in their SIT distributions within each SMOS bin compared to the wider scatter seen for UIT and particularly CPOM.

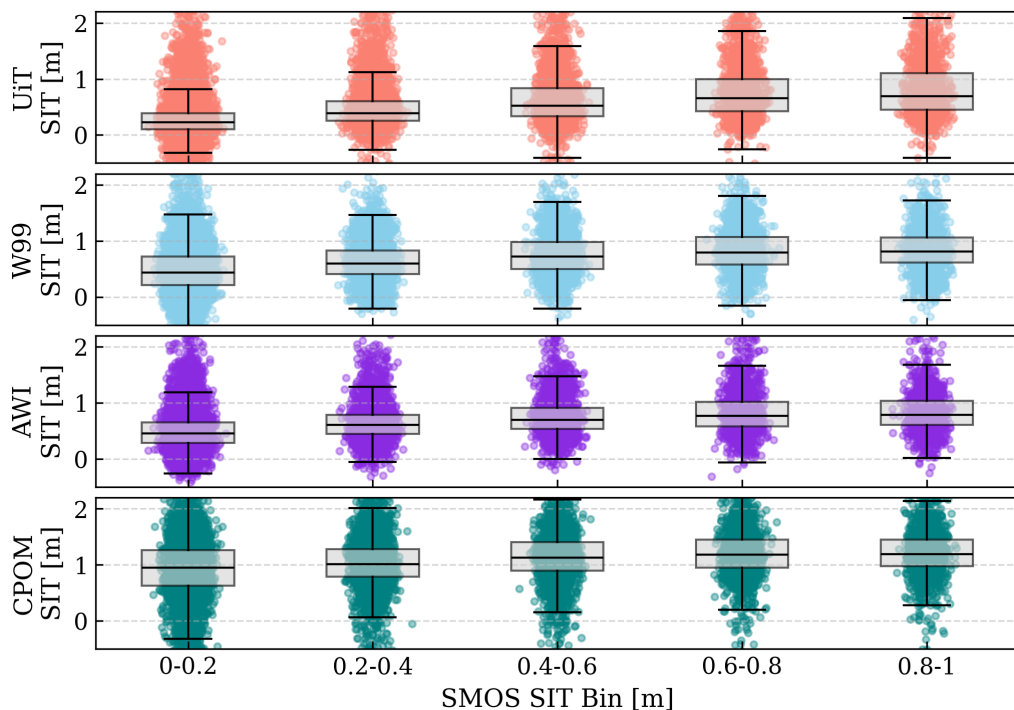


Figure 6.4: Box scatter plot illustrating CryoSat product sea ice thickness (SIT) estimates as a function of SMOS SIT values, grouped into corresponding bins.

Table 6.1 presents the statistical metrics comparing CryoSat products SIT estimates to the SMOS AWI product within two SIT intervals, 0.0-0.4 m and 0.4-1.0 m. The UIIT product shows the lowest overall bias and the lowest RMSE in the 0.0-0.4 m bin, though it exhibits a higher RMSE in the higher bin. Across all products, the CC remains consistently low. However, the UIIT product archives the lowest DISO value in the first bin and a higher DISO in the second bin. Among the other products, the W99 product performs better than AWI in the lower bin, as reflected by a lower DISO value. In Contrast, the AWI product returns a lower DISO value in the higher bin than the W99.

Table 6.1: Statistical metrics comparing CryoSat products to the SMOS AWI product within the SIT intervals 0.0-0.4 m and 0.4-1.0 m. The table includes bias, RMSE, CC, and DISO.

Product	Thickness [m]	Bias	RMSE	CC	DISO
UiT	0.0-0.4	0.216	0.377	0.318	0.682
	0.4-1.0	0.053	0.526	0.125	0.959
W99	0.0-0.4	0.381	0.507	0.201	0.872
	0.4-1.0	0.114	0.461	0.071	0.948
AWI	0.0-0.4	0.413	0.570	0.210	0.913
	0.4-1.0	0.159	0.430	0.127	0.907
CPOM	0.0-0.4	0.804	0.992	0.070	1.693
	0.4-1.0	0.487	0.674	0.070	1.693

6.2 Validation Against OIB Airborne Observations

The following results from the validation of CryoSat UiT and SMOS products against OIB airborne observations are presented briefly, as the OIB dataset contains a limited number of observations in the thin SIT range.

Figure 6.5 presents the mean SIT from the UiT and SMOS products as a function of binned OIB SIT values. The lower panels show the corresponding distribution plots, with the OIB SIT distribution included as reference. The SMOS product demonstrates closer agreement with the OIB SIT in the lower thickness bins, but significantly underestimates the OIB measurements in the highest bins (above 0.6 m). Conversely, the UiT products consistently overestimate SIT in the lower bins and begin to underestimate in the higher bins, indicating a systematic bias that shifts with SIT.

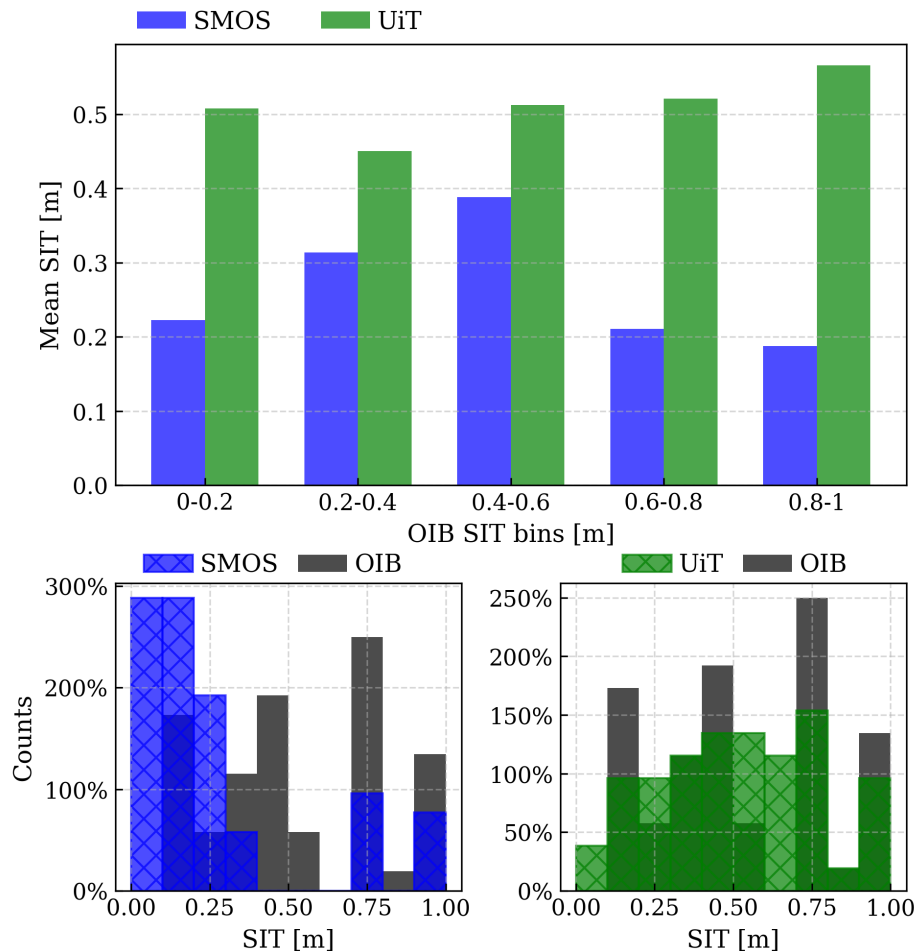


Figure 6.5: Mean sea ice thickness (SIT) bar plot and corresponding distribution plot comparing CryoSat UiT and SMOS AWI products with the OIB measurements.

Figure 6.6 presents a box scatter plot comparing SIT estimates from the UIT and SMOS products as a function of binned OIB SIT values. For each bin, both mean and median are displayed. Consistent with the results in Figure 6.5, the UiT product overestimates SIT in the lower OIB bins and underestimates it in the higher bins. In contrast, the SMOS product shows closer agreement with the OIB in the thinner ice bins, although some deviations are present. However, in the higher SIT bins, SMOS significantly underestimates the OIB values. The scatter distributions also highlight a key limitation of the analysis. Very few OIB measurements are available in this SIT regime, particularly in the lower thickness range, which introduces uncertainty in the statistical comparisons.

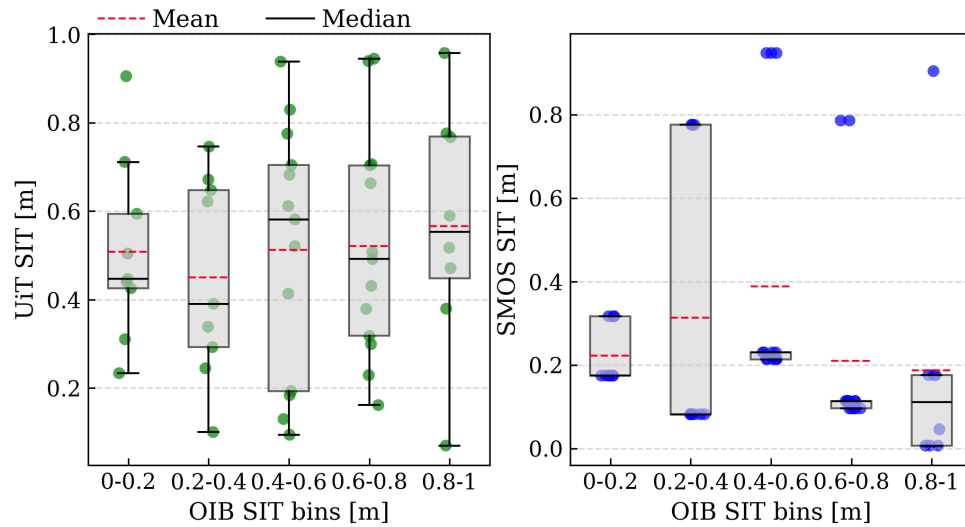


Figure 6.6: Box scatter plot illustrating CryoSat UiT and SMOS AWI sea ice thickness (SIT) estimates as a function of OIB SIT values, grouped into corresponding bins.

Consequently, both the UiT and SMOS products yield low CC values and relatively high DISO scores, as shown in Table 6.2. Among the results, SMOS demonstrates the lowest bias within the 0.0-0.4 m OIB SIT bin, while UiT exhibited the lowest bias in the higher thickness bin.

Table 6.2: Statistical metrics comparing CryoSat UiT and SMOS AWI to the OIB measurements within the SIT intervals 0.0-0.4 m and 0.4-1.0 m. The table includes bias, RMSE, CC, and DISO.

Product	Thickness Range [m]	Bias	RMSE	CC	DISO
UiT	0.0-0.4	0.228	0.332	-0.340	1.948
	0.4-1.0	-0.175	0.345	0.098	1.346
SMOS	0.0-0.4	0.017	0.269	-0.253	1.253
	0.4-1.0	-0.430	0.567	-0.211	1.571

6.3 Validation Against BGEP Mooring Data

Figure 6.7 presents the mean SID from the UiT and SMOS products as a function of binned mooring SID values. The lower panels show the corresponding distribution plots, with the mooring SID distribution included as reference.

In the lower SID bins (0.0-0.6), the SMOS product shows better alignment with the mooring observations, though some deviations are present. The UiT product tends to overestimate SID in these lower bins but remains within the range of the corresponding mooring values. At higher SID bins, the UiT product demonstrates improved agreement with the mooring data, whereas the SMOS product shows a mixed performance with both overestimation and underestimation. Despite these variations, both satellite products exhibit a consistent increase in estimated SID with increasing mooring SID bin values, reflecting a coherent overall trend.

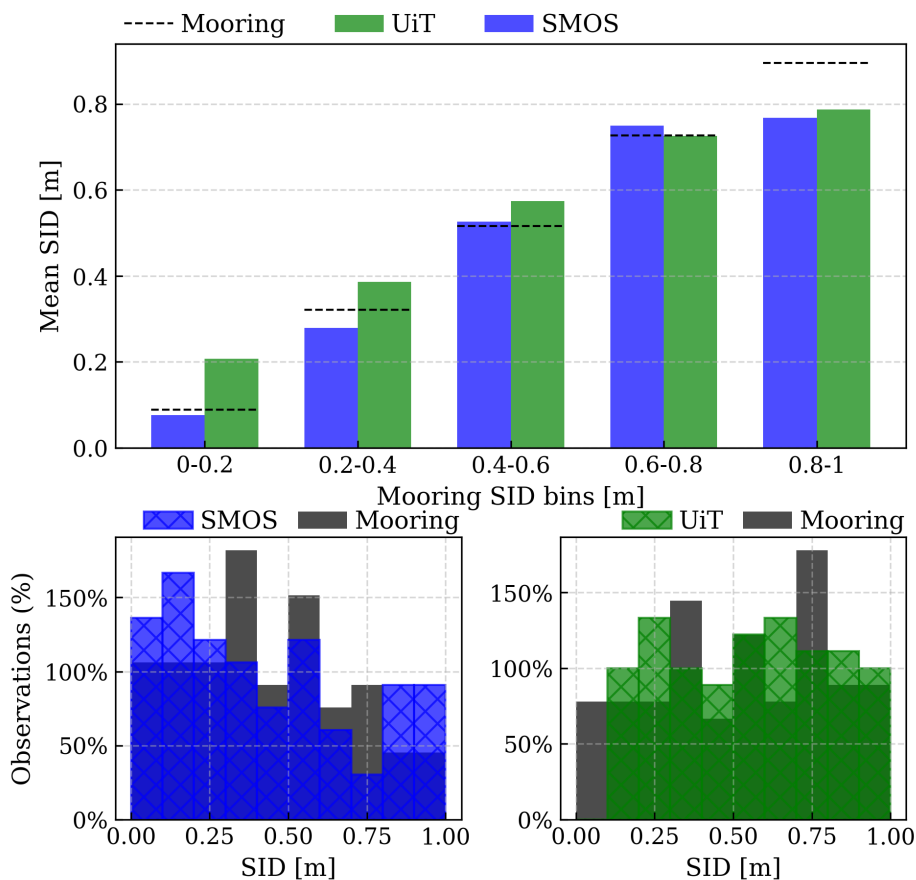


Figure 6.7: Mean sea ice draft (SID) bar plot and corresponding distribution plot comparing UiT and SMOS products with the BGEP mooring measurements.

Figure 6.8 presents a time series of SID measurements obtained from moorings A, B, and D, alongside corresponding SID estimates from the UiT and SMOS

products. SMOS estimates that exceed a predefined threshold are marked as saturated (see Section 5.5). Overall, both the UiT and SMOS estimates show good agreement with the SID measurements from the moorings, although deviations are observed. Notably, between 2012 and 2014, at all three mooring locations, the UiT and SMOS estimates exhibit similar deviations from the mooring SID values. Additionally, SMOS shows a higher frequency of saturated estimates at mooring locations A and B compared to location D. Despite these deviations, both UiT and SMOS estimates capture the seasonal variations observed by the moorings and follow similar temporal trends.

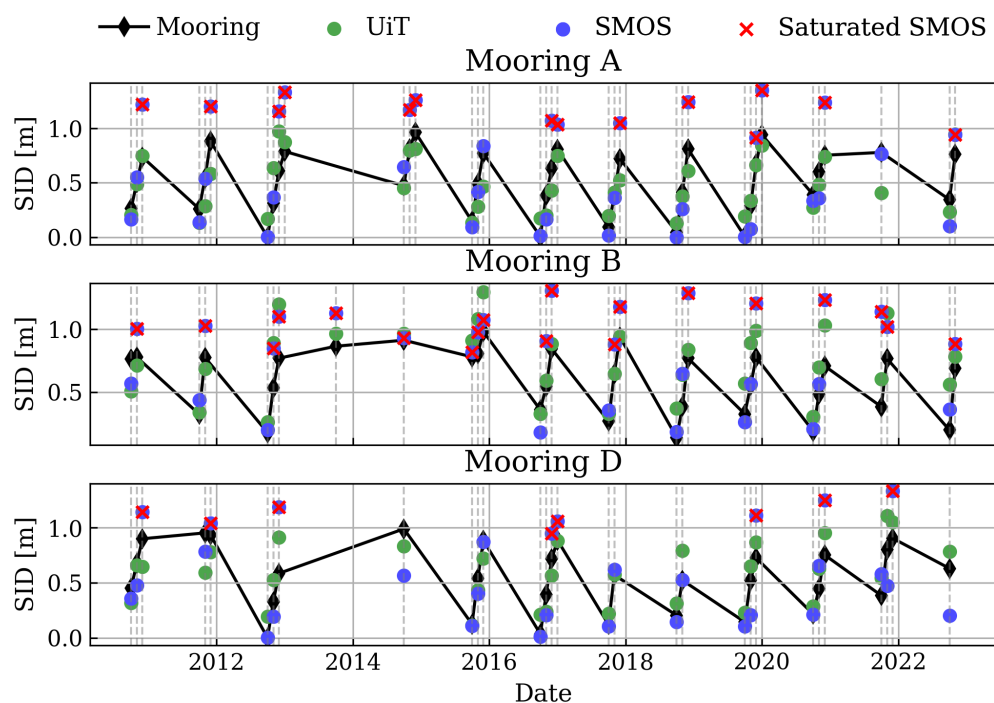


Figure 6.8: Sea ice draft (SID) measurement time series from the BGEP moorings at locations A, B, and D, shown alongside corresponding SID estimates from the CryoSat UiT and SMOS AWI products. SMOS values exceeding the predefined threshold are marked as saturated.

Figure 6.9 presents a pair scatter plot comparing SID estimates from the UiT and SMOS products with mooring observations. The top panel displays the comparisons using raw SID values, while the bottom panel shows the corresponding scatter plots based on seasonal anomalies, highlighting the correspondence in seasonal variability. Each plot includes key statistical metrics for performance evaluation.

In the raw SID comparison (Figure 6.9a), the UiT shows a good linear correlation ($r = 80$), though the slope is below one (0.74), indicating some overestimation at lower SID values, which is also visible in the plot. The SMOS product exhibits a slightly stronger correlation ($r = 84$) and slope closer to one (0.95), suggesting a better agreement with the mooring observations. While UiT has a positive bias of 0.02 m, SMOS shows an equivalent negative bias. Both products share the same RMSE, which indicates that SMOS offers a more accurate absolute SID estimate in this case. When using seasonal anomalies (Figure 6.9b), the correlation for the UiT product drops to $r = 0.63$, with the slope decreasing to 0.57, indicating reduced consistency in capturing seasonal variability. The SMOS product retains a higher correlation at $r = 0.81$ and a smaller slope drop at 0.81, reflecting a relatively stable performance even when the seasonal trend is removed.

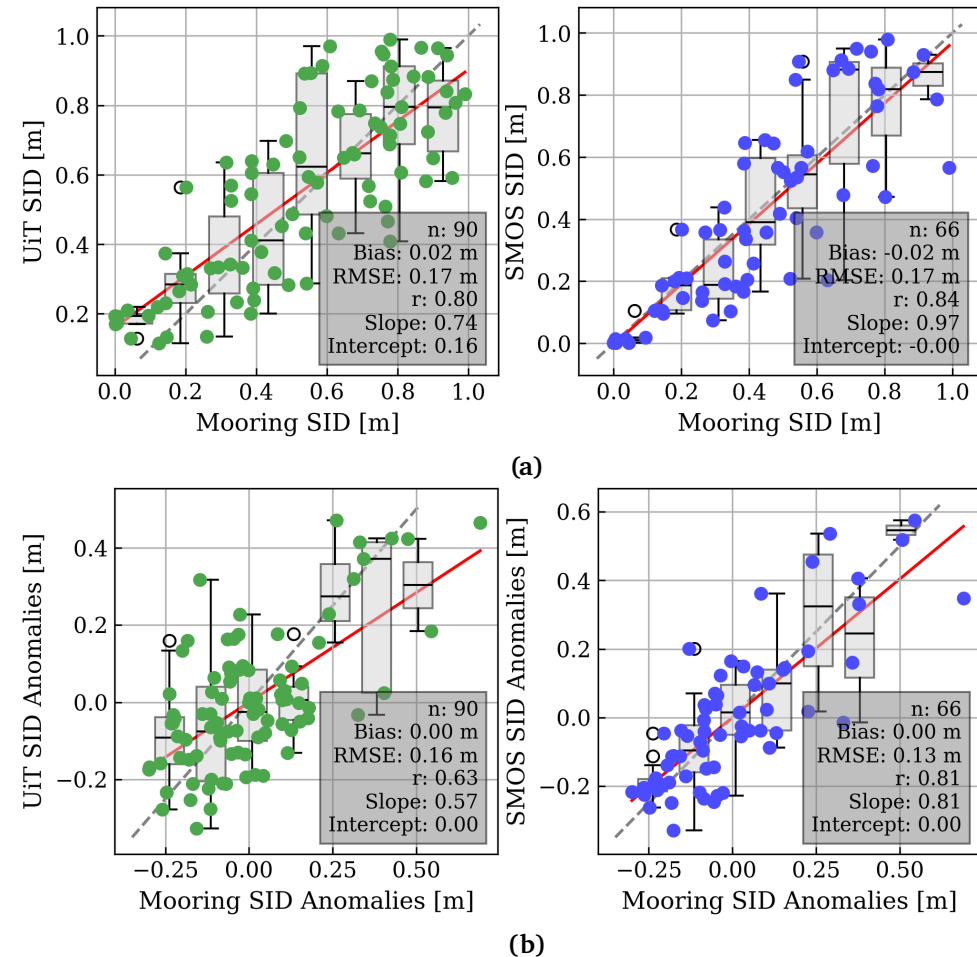


Figure 6.9: (a) Pair scatter plot of raw sea ice draft (SID) estimates from CryoSat UiT and SMOS AWI products as a function of mooring SID observations. (b) Corresponding pair scatter plot using seasonal anomalies.

The statistical metrics for the BGEP analysis are presented in Table 6.3, building on the results shown in Figure 6.9. The SMOS product consistently exhibits higher CC values than the UiT product. In terms of the DISO metric, SMOS performs better in the thin SID bin, whereas the UiT product achieves a lower DISO score (indicating better overall agreement) in the thicker SID bin.

Table 6.3: Statistical metrics comparing CryoSat UiT and SMOS AWI to the BGEP measurements within the SID intervals 0.0-0.4 m and 0.4-1.0 m. The table includes bias, RMSE, CC, and DISO.

Product	Thickness Range [m]	Bias	RMSE	CC	DISO
UiT	0.0-0.4	0.088	0.159	0.582	1.475
	0.4-1.0	-0.014	0.183	0.470	0.530
SMOS	0.0-0.4	-0.027	0.116	0.721	0.279
	0.4-1.0	-0.005	0.204	0.498	1.501

6.4 Validation Against SMOSice Campaign Measurements

Figure 6.10 shows the tSIT estimates from UiT and SMOS products, overlaid with HEM tSIT measurements. The SMOS product shows a region with consistently low to near-zero tSIT values, while the UiT product reveals greater spatial variability in tSIT. Where both products show an increase in tSIT near the coastline. The overlaid HEM tSIT estimates similarly indicate a spatially varying ice cover, aligning more closely with the range captured by the UiT product. Overall, the SMOS seems to underestimate tSIT compared to both the UiT and HEM datasets.

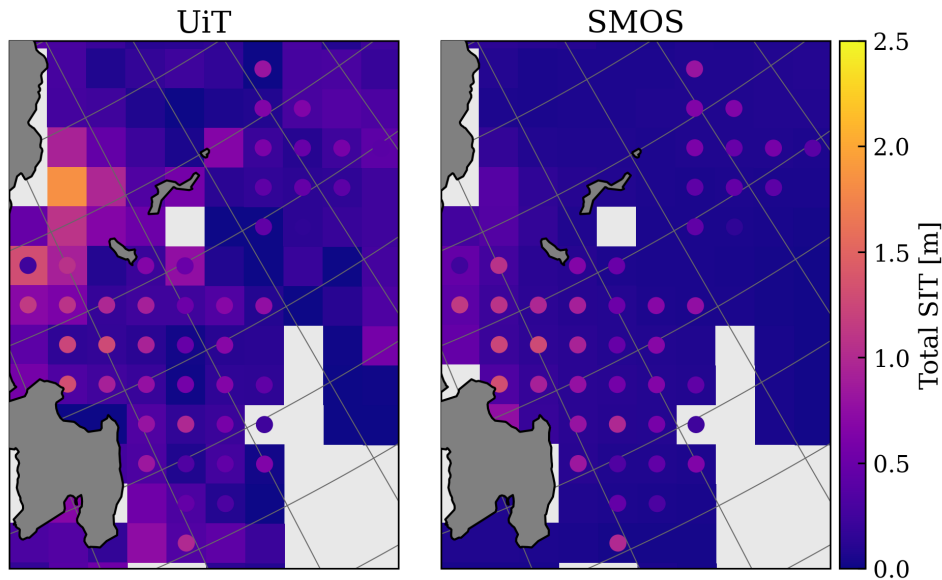


Figure 6.10: Map showing total sea ice thickness (tSIT) estimates from CryoSat UiT (left figure) and SMOS AWI (right figure) products, with overlaid HEM tSIT estimates resampled to the same spatial grid.

Figure 6.11 presents the tSIT distributions corresponding to the spatial comparison in Figure 6.10, with HEM tSIT overlaid against the distributions from the UiT and SMOS products. The SMOS distribution is sharply centered near the lower thickness range, peaking at around 0.10 m, and shows a rapid decline near 0.5 m. The UiT distribution is broader, extending up to 1.0 m, with the highest occurring tSIT around 0.20 m. The HEM distribution begins at a slightly higher thickness than both the satellite products and extends up to approximately 1.3 m, with a peak around 0.40 m. Among the satellite products, the UiT tSIT distribution aligns more closely with the HEM observations, both in spread and central tendency, whereas SMOS underrepresented thicker ice.

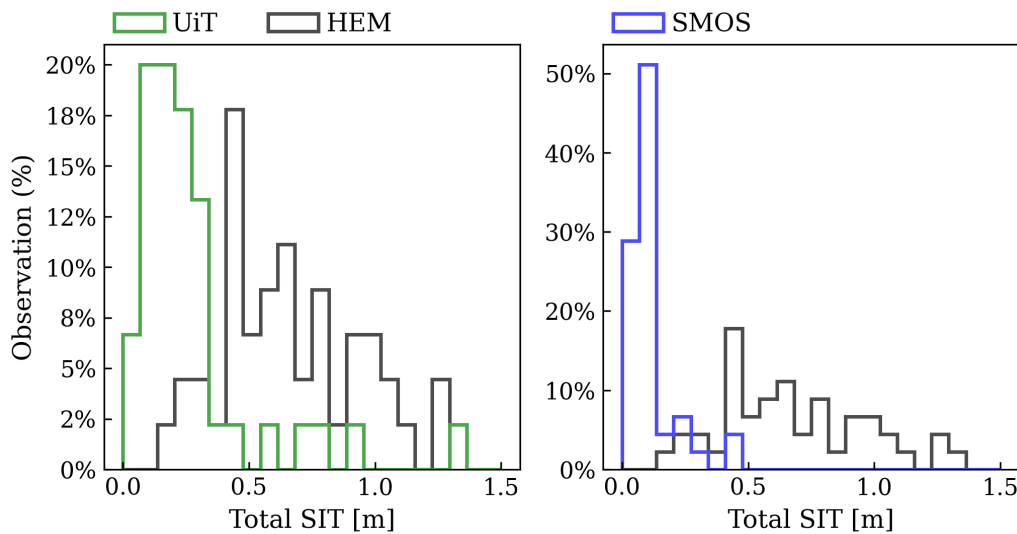


Figure 6.11: Distribution of total sea ice thickness (tSIT) derived from HEM measurements, compared with corresponding tSIT distributions from the CryoSat UiT and SMOS AWI products.

Table 6.4 presents the statistical comparison of HEM tSIT and the corresponding estimates from the UiT and SMOS products. The UiT product exhibits both the lowest bias and RMSE, indicating better agreement in terms of absolute thickness values. In contrast, the SMOS product shows a slightly higher bias and RMSE but achieves a higher CC of 0.658, compared to 0.448 for UiT, suggesting a better linear relationship with the HEM data. Despite the higher bias and RMSE, SMOS returns a slightly lower DISO score than UiT, indicating marginally better overall performance.

Table 6.4: Statistical metrics comparing CryoSat UiT and SMOS AWI to the HEM tSIT measurements. The table includes mean, bias, RMSE, CC, and DISO.

Product	Mean [m]	Bias	RMSE	CC	DISO
UiT	0.246	-0.409	0.470	0.448	1.142
SMOS	0.101	-0.554	0.589	0.658	1.057

Figure 6.12 displays a comparison between tFB distributions from ALS and UiT in the left panel, and the corresponding alignment of the CryoSat ground track with the ALS flight path in the right panel. The UiT tFB distribution shows a strong resemblance to the ALS distribution, both in shape and overall spread.

The peak of the ALS distribution occurs at 0.056 m, while the UiT distribution peaks at around 0.079 m. Given the histogram bin size of 0.03 m, both peaks overlap at the end, indicating a close match. Beyond the peak values, the UiT distribution continues to follow the general form of the ALS distribution, capturing its shape and variability to a degree of accuracy. The UiT tFB measurements, shown in the right panel, include some values exceeding 1 m. However, the majority of the observations fall within the tFB range presented in the distribution plot.

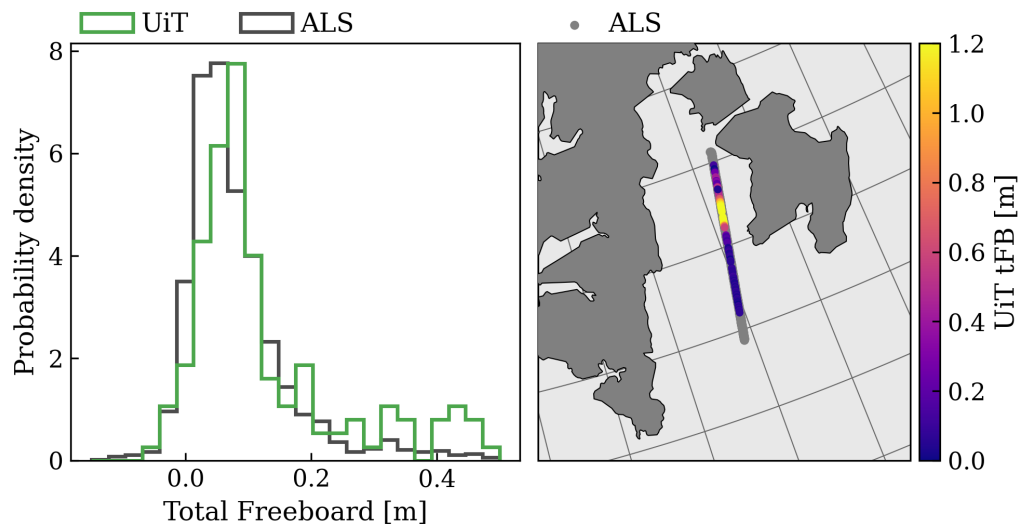


Figure 6.12: Left panel shows the total radar freeboard (tFB) distribution from ALS measurements compared with the tFB derived from the CryoSat UiT product. Right panel illustrates the CryoSat ground track aligned with the ALS flight path on 26 March 2014.

The ALS tFB measurements from the flight conducted on 26 March 2014, used in the comparison with UiT derived tFB in Figure 6.12, covered a broad area characterized by mixed stages of sea ice development. Representative images captured during the flight are shown in Figure 6.13.

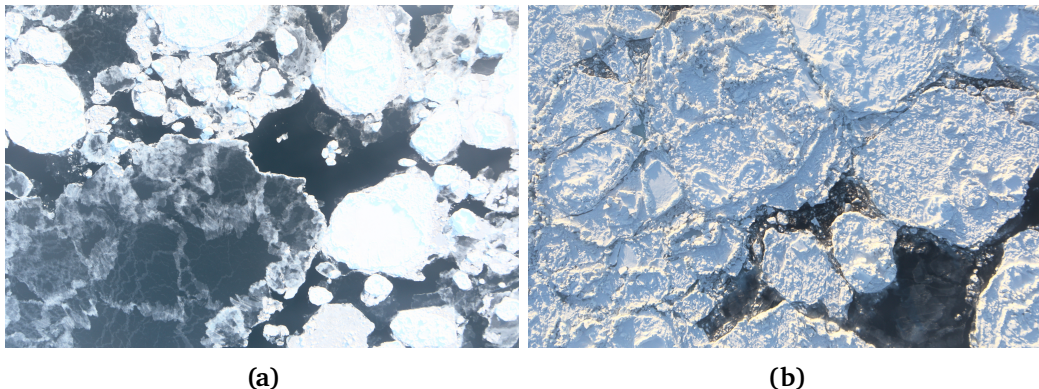


Figure 6.13: Photographs taken during the ALS flight on 26 March 2014, illustrating sea ice at various stages of development. Image credit: ESA.

Table 6.5 displays the statistical metric derived from the comparison between UiT and ALS tFB distribution shown in Figure 6.12. The UiT product yields a slightly higher mean tFB than the ALS measurements, due to the greater number of observations in the thicker freeboard range, as seen in the distribution plot. Despite this difference, the bias remains relatively low. However, the RMSE is considerably high, and the CC is relatively low. As a result, the combined effect of these metrics leads to a relatively high DISO score.

Table 6.5: Statistical metrics comparing CryoSat UiT tFB to the ALS tFB measurements. The table includes mean, bias, RMSE, CC, and DISO.

Product	Mean [m]	Bias	RMSE	CC	DISO
UiT	0.126	0.058	0.150	-0.181	1.217
ALS	0.068				

In the comparison between the ALS and daily SMOS measurements, the ALS tFB was converted to SIT. Figure 6.14 presents this comparison, with the left panel showing the SIT distribution from both SMOS and ALS, and the right panel illustrating the spatial distribution of SMOS SIT, overlaid with the corresponding ALS-derived SIT estimates. The SMOS SIT distribution is strongly skewed toward thinner ice, with a pronounced peak near zero followed by a sharp decline. In contrast, the ALS SIT distribution spans the full 0-1 m range more uniformly. In the spatial comparison (right panel), the ALS data suggest that thicker sea ice extends farther offshore than what is indicated by the SMOS SIT estimates, which appear to underestimate thickness in areas more distant from the coastline.

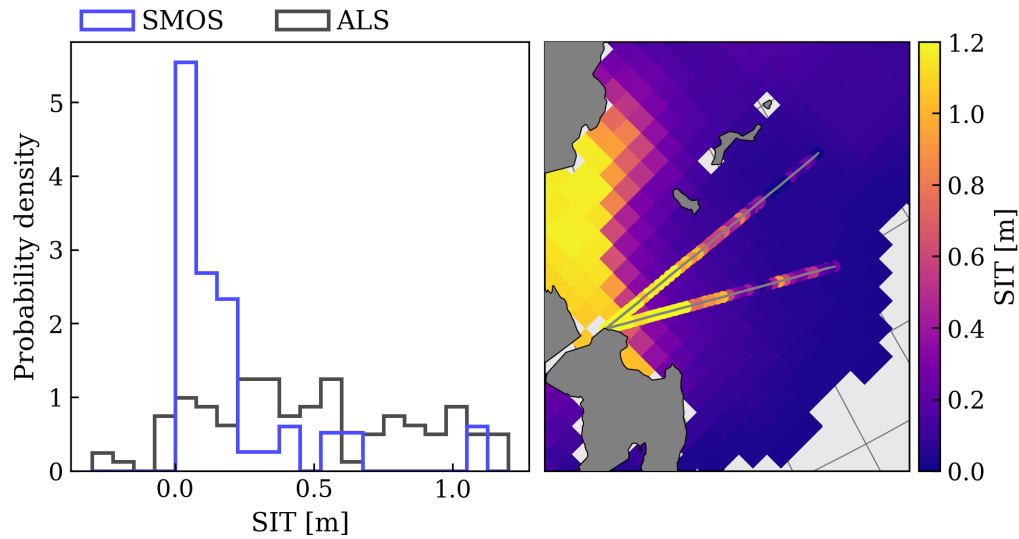


Figure 6.14: Left panel shows the sea ice thickness (SIT) distribution from ALS measurements compared with the SIT measurements from the daily SMOS AWI product. The right panel illustrates the SMOS AWI spatial distribution with the overlapping ALS flight path on 24 March 2014.

Images illustrating the varying sea ice conditions during the retrieval of ALS SIT measurements on 24 March are shown in Figure 6.15.

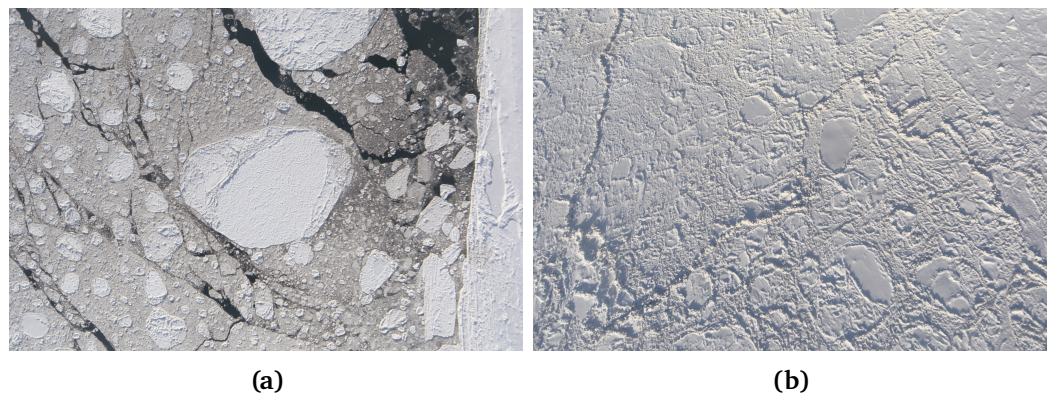


Figure 6.15: Photographs taken during the ALS flight on 24 March 2014, illustrating sea ice at various stages of development. Image credit: ESA

In Table 6.6, the statistical metrics is derived from the comparison between daily SMOS and ALS SIT distribution, as shown in Figure 6.14. The SMOS product retrieves a significantly lower mean SIT compared to the ALS estimates,

resulting in a relatively large negative bias and an RMSE of 0.458. Despite this, SMOS achieves a high CC of 0.782, suggesting a strong linear correlation. However, when combined, the overall DISO score remains high.

Table 6.6: Statistical metrics comparing daily SMOS AWI SIT to the ALS-derived SIT measurements. The table includes mean, bias, RMSE, CC, and DISO.

Product	Mean [m]	Bias	RMSE	CC	DISO
SMOS	0.077	-0.396	0.458	0.782	6.396
ALS	0.473				

/ 7

Summary & Discussion

The first analysis evaluated the UiT product against the CryoSat W99, AWI, and CPOM products, using the SMOS AWI product as the reference dataset. The comparison clearly demonstrates the impact of different waveform re-tracking algorithms and snow climatology models for the SIT retrieval. Among the products, the UiT dataset showed the most consistent alignment with the SMOS SIT estimates. Evident across multiple visual comparisons, including the map of mean difference, box scatter plot, and bar distribution plot (Figures 6.1, 6.4, and 6.2). However, the UiT product still exhibits high overestimation in the Greenland Sea region. In the box scatter, the UiT slightly overestimated SIT in the two lowest thickness bins but maintained strong correspondence with SMOS throughout. In the statistical metric, UIT achieved the best DISO score (0.683) in the 0.0-0.4 range, and the lowest bias (0.053) in the higher 0.4-1.0 bin, though AWI slightly outperformed it in overall DISO score (0.907) for the upper bin. From the mean difference (Figure 6.3), the UiT product slightly overestimates SIT compared to SMOS in the lowest thickness range, with bias decreasing from 0.24 m in the 0.0-0.2 m bin to 0.06 m in the 0.6-0.8 m bin. Beyond this range, the UiT begins to underestimate the SIT relative to SMOS. The W99 product, which shares the same retracking algorithm (LARM) as UiT but uses a modified Warren 1999 climatology, saw a stronger overestimation of SIT, evident by the higher count of thick ice in the bar distribution (Figure 6.2). Nonetheless, it outperformed AWI in the

thinner ice regime and showed improved alignment with SMOS SIT as the thickness increased. The CPOM product, as well as the AWI product, applies its version of the TFMRA retracking method along with a modified Warren 1999 climatology. The CPOM exhibited a consistent overestimation across the entire 0-1 m SIT range. This pattern suggests that the LARM algorithm, used in the UiT and W99, is more suitable for detecting thin sea ice and is further improved using the SnowModel-LG. In comparison, the use of a modified Warren 1999 climatology in AWI and CPOM introduces additional biases as expected, including the use of a modified TFMRA method. However, both AWI and CPOM tend to perform better as the SIT reaches and exceeds 1 m, with AWI showing the best agreement with SMOS SIT in the upper thickness range. For the validation of the UiT product against independent observations from the OIB, BGEP moorings, and the SMOSice campaign, alongside comparisons with SMOS retrieved SIT, provided insight into the UiT product capabilities of detecting thin SIT.

In the OIB validation, a limited number of observations around 410 within the thin SIT range constrained the analysis to some extent. The UiT product tended to overestimate SIT up to the 0.4-0.6 m bin, whereas the SMOS showed a slight but consistent overestimation in the first two bins. Both products significantly underestimated SIT in the higher thickness bins, due to the low amount of SIT observation from the OIB data, as seen in Figures 6.5 and 6.6. Notably, the UiT product showed a greater alignment with the overall OIB SIT distribution compared to SMOS. Despite this, both products returned high DISO scores, indicating limited agreement with the OIB measurements. The UiT product achieved the lowest bias and RMSE in the highest bin, while the SMOS showed a higher (though negative) CC value. Whereas in the lowest bin, the UiT product displayed a higher (negative) CC value than SMOS. It should be noted that in the more narrowly defined SIT intervals (0.2 m bins), as presented in Appendix Table A.2, the SMOS exhibits maximum negative CC value in the thinnest SIT bins.

In the comparison with BGEP mooring SID data, SMOS demonstrated a stronger linear correlation and overall better performance in the thinner SID regime, as reflected both in the raw and seasonal anomaly scatter plots (Figure 6.9). In the raw scatter plot, the UiT product tends to overestimate SID values up to 0.6 m, after which it begins to underestimate the mooring observations. This difference becomes more pronounced when the seasonal trend is removed, highlighting the UiT product's sensitivity to seasonal variability when compared to the SMOS product. This suggests potential limitations in the UiT product's ability to resolve interannual variability in thinner ice regimes fully. However, it is important to note that the SMOS data used in this analysis had data points exceeding 1 m filtered out. This filtering may limit

its ability to capture interannual variability and could enhance the agreement with the thin ice measured by the moorings. As the altimetry-based results can be contaminated by some thick overestimated samples. As such, any direct comparison in this context remains inconclusive. Nevertheless, both UiT and SMOS products capture the seasonal patterns observed in the mooring time series (Figure 6.8). Two notable patterns emerge, the first being the amount of saturation of SMOS estimates near 1 m, which is expected due to the upper limit of SMOS SIT retrieval. The second is that both products tend to systematically overestimate or underestimate the same SID values, indicating shared bias. Regarding the SID distribution, both datasets show general agreement with the mooring SID distribution. However, the UiT product appears to lack observation near 0 m, which may limit its ability to represent very thin ice. This limit could be related to the processing threshold, where altimetry data are excluded when SIC, obtained from an external reference product, falls below 15%. Such conditions often correspond to the presence of the thinnest, newly forming ice. From the derived statistical metric (Table 6.3), UiT and SMOS return comparable bias, RMSE, and CC values. The DISO score shows that SMOS performs better in the lower SID bin, while UiT outperforms SMOS in the upper SID bin, although SMOS retains a higher CC value in that range. The mean SID comparison (Figure 6.7) is constrained to values below 1 m to account for the SMOS retrieval limit. When this constraint is removed (Appendix Figure A.5), the SMOS product shows a greater overestimation, whereas UiT aligns more closely with the upper SID bins.

In the final validation using measurements from the SMOSice campaign, the UiT product showed good agreement with both the ALS and HEM datasets. The spatial distribution of HEM-derived tSIT in Figure 6.10 shows that the UiT product retrieved a more variable tSIT pattern, resembling that of the HEM measurements. In contrast, the SMOS product showed an increase in tSIT near the coastline, followed by a decrease towards values near 0 m further offshore. This behavior is reflected in the distribution plot (Figure 6.11), where both products exhibit a strong concentration of thin tSIT compared to the HEM measurements. The UiT product shows a broader distribution up to approximately 0.5 m, while the SMOS distribution peaks sharply near 0 m and rapidly decreases. From the distribution, it suggests that the UiT product aligns more closely with the HEM observations. The statistical metric confirms this to a degree, the UiT product achieved the lowest bias and RMSE, while SMOS returned a higher CC value. As a result, both products produced high DISO scores, with values of 1.142 for UiT and a slightly better 1.057 for SMOS. However, Appendix Table A.4 shows that the UiT product exhibits the lowest bias and RMSE within the 0.0-0.2 m tSIT range, and performs best in the 0.2-0.4 m range, where it achieves low bias, low RMSE, and a high

CC of 0.971. In the ALS tFB comparison, which aligned with the CryoSat ground track, the UiT tFB distribution closely matched the ALS (Figure 6.12), but slightly skewed toward higher values. This yielded a low bias (0.058 m) and low RMSE, although the CC value was unexpectedly low (-0.181), despite the visual alignment that suggested strong agreement, where in Appendix Table A.5 the UiT product only deviates by 0.7 cm from the mean ALS tFB. In contrast, the comparison between ALS-derived SIT and daily SMOS SIT revealed a more uniform ALS SIT distribution across the 0-1 m range, whereas the SMOS data showed a sharp peak near 0 m, decreasing rapidly upon 0.5 m. This resulted in relatively high bias and RMSE, but a strong CC of 0.782, indicating good linear alignment despite the underrepresentation of thicker ice. The obtained results and statistical metrics suggest that SMOS may exhibit over-sensitivity to thin ice within its footprint. For instance, if approximately 50% of the footprint consists of thin ice and the rest includes thicker, older floes, the measurements will be disproportionately weighted toward the thin sea ice. This can lead to systematic underestimation of the actual SIT. In the case of CryoSat, the results imply that the combination of LARM retracking and the SnowModel-LG produces a reasonable estimate of the mean and variability of ice thickness. However, the observed low correlation may stem from noise present in the along-track freeboard data. Before gridding, the radar altimeter signal is affected by speckle and other sources of noise, which introduce artificial variability in the freeboard measurements. This noise likely reduces the agreement with coincident ALS observation, leading to poor correlation despite otherwise consistent distribution.

The validation results raise important considerations regarding the applicability of altimetry-derived SIT products below 1 m, particularly for downstream applications such as data assimilation and forecasting. Based on the analysis, the CryoSat UiT product provides consistent and reasonable SIT estimates down to approximately 0.4-0.5 m. Below this threshold, the product exhibits growing bias and reduced correlation, suggesting decreased reliability. This indicates that. For applications requiring reliable detection of thin ice, a conservative threshold around 0.4 m may be appropriate for standalone use of the UiT product. However, as shown in Appendix Tables A.4 and A.5, and discussed previously, the UiT product performed better than SMOS in the 0.0-0.2 m and 0.2-0.4 m ranges in regards of tSIT and tFB. These results suggest that the UiT product may still hold the capability for retrieving very thin sea ice. In contrast, the SMOS product consistently performed well in the thinnest SIT intervals (particularly < 0.4 m), despite the seen saturation effects beyond approximately 0.5-0.6 m. The strong DISO scores and alignment with the independent observations in the lower SIT bins highlight SMOS strength in

detecting newly formed or FYI, especially under early freeze-up or rapid melt onset, where altimetry data may be sparse or noisy. However, the observed over-sensitivity of SMOS to thin ice within the footprints underscores the need for caution when interpreting its estimates in mixed sea ice conditions. In such cases, combining SMOS with CryoSat data with the proposed threshold, as in a blended product (e.g., CS2SMOS from Ricker et al. (2017)) or assimilation frameworks, may be the most robust approach. Ultimately, the decision to use SMOS, CryoSat, or both should depend on the expected ice regime and the tolerance of the application for error in different thickness bins. A different approach could involve using the SMOS data up to 0.4 m, the UiT product from 0.4 m to 1.0 m, and a product based on TFMRA with a modified Warren 1999 climatology for ice thicker than 1.0 m and MYI. The latter has demonstrated reliability over MYI, for which the climatology was originally developed. These findings support that altimetry-derived SIT products using the LARM algorithm and the SnowModel-LG can be useful below 1 m for data assimilation, with thresholding, and support from complementary datasets like SMOS, when operating in thin ice-dominated regions.

8

Conclusion & Future Work

The primary objective of this study was to assess whether the UiT CryoSat product, which employs the LARM physical retracking algorithm in combination with the SnowModel-LG climatology, is capable of reliably retrieving SIT measurements down to a few tens of centimeters. The initial analysis of the UiT product demonstrated good agreement with the SMOS AWI data, indicating that the use of the LARM algorithm is well suited for retrieving thin SIT estimates seen in the use of the W99 product. This performance was further enhanced by incorporating the SnowModel-LG, enabling the UiT product to outperform the other CryoSat products, where in the 0-1 m SIT range it achieved a total bias of just 0.061 m. The validation analysis aimed to establish a lower retrieval boundary of the UiT product, using the SMOS product as a comparative benchmark. In the comparison against OIB data, the UiT product showed the best agreement in the 0.4-0.6 m SIT range, yielding relatively low bias and RMSE, despite SMOS achieving a higher CC value. For thicker ice, the UiT product outperformed SMOS. In the validation against BGEP mooring SID data, the UiT product successfully captured the seasonal pattern, though it exhibits instances of both over- and underestimation. Across the full range, the UiT returned bias, RMSE, and DISO values comparable to SMOS. Notably, UiT achieved its highest CC for SID values up to 0.2 m, and showed its lowest bias, ranging from 0.065 to -0.001 m, in the 0.2-0.8 m range, along with an acceptable CC in the 0.4-0.6 m bin. Overall, the UiT

product showed its best performance in the 0.4-1.0 m thickness range, when compared to the SMOS product. However, it should be noted that the SID anomaly analysis revealed signs of reduced consistency in capturing seasonal variability. In the final analysis, the UiT product showed strong agreement with measurements from both the HEM system and ALS observations. In the HEM comparison, the UiT product achieved its lowest bias of -0.014 m in the 0.0-0.2 tSIT range, and an exceptionally high CC of 0.971 in the 0.2-0.4 range, outperforming SMOS. Similarly, in the comparison against ALS tFB measurements, the UiT product deviated only by 0.7 cm in the 0.0-0.2 m range and showed a good agreement with the ALS distribution.

These analysis displays that the CryoSat UiT product is capable of reliably retrieving SIT down to a few tens of centimeters. The first three validation efforts show that the UiT product can consistently detect and retrieve SIT down to approximately 0.4 m, while the final analysis demonstrated its ability to retrieve both tSIT and tFB below 0.4 m. Notably, the SMOS product consistently performed well below 0.4 m, maintaining strong sensitivity to very thin ice. This marks an important advancement, as CryoSat SIT retrievals have traditionally been considered unreliable for ice thinner than 1 m, and are often excluded from data assimilation or assigned error estimates of up to 100% in such regions. In the context of data assimilation, these results suggest that a threshold of around 0.4 m may be appropriate for use of the UiT product. In a blended approach, using SMOS data for thickness below 0.4 m, the UiT product from 0.4 m to 1.0 m, and a CryoSat product employing the TFMRA algorithm and a modified Warren 1999 climatology for SIT above 1m. These findings state the need to re-evaluate the role of CryoSat data in thin ice regimes, particularly in recognizing that intermediate and thin ice returns should be included in data assimilation and floe classification algorithms to improve model accuracy and sea ice monitoring.

For further work, an analysis to investigate the integration of the modified Warren 1999 climatology with the LARM algorithm, to assess whether this combination may be more suitable for thicker ice regimes. When compared to other CryoSat products. Additionally, the uncertainty estimates provided by the UiT product should be further examined, particularly in relation to their behavior across different thickness ranges. As observed in the initial comparisons analysis, the UiT product occasionally returned high SIT values within the lowest SIT bins. A targeted analysis should evaluate whether these outliers are associated with elevated uncertainty levels, and if so, whether they can be systematically identified and filtered to improve reliability in thin ice conditions.

/9

Data & Code Availability

The code and parts of the data that support the findings of this thesis are openly available in the FYS-3931 Master Thesis repository at <https://github.com/tva050/FYS-3931-Master-thesis>.

Some datasets used in this study are publicly available from third-party sources, including:

- The SMOS sea-ice thickness data (AWI) is from <https://www.meereisportal.de> portal (funded by REKLIM-2013-04)
- The CryoSat-2 sea-ice thickness data (AWI) is from <https://www.meereisportal.de> portal (funded by REKLIM-2013-04)
- The CryoSat-2 CPOM product from the Centre for Polar Observation and Modelling, accessed from https://www.cpom.ucl.ac.uk/csopr/seoice.php?thk_period=1.
- Operation IceBridge data from NASA's NSIDC portal.
- BGEP mooring data from the Woods Hole Oceanographic Institution.

- SMOSice campaign data from the European Space Agency.

Access to these datasets may require user registration or acceptance of license agreements from the respective providers. Proprietary or preprocessed datasets used internally (as the UiT product) are available upon reasonable request and with permission from the Earth Observation Group at UiT - The Arctic University of Norway.

Bibliography

- Awange, J. L., Kyalo Kiema, J. B., Awange, J. L., and Kyalo Kiema, J. B. (2013). Fundamentals of remote sensing. *Environmental Geoinformatics: Monitoring and Management*, pages 111–118.
- Barre, H. M. J. P., Duesmann, B., and Kerr, Y. H. (2008). Smos: The mission and the system. *IEEE Transactions on Geoscience and Remote Sensing*, 46(3):587–593.
- Bašić, T. (2023). Introductory chapter: Satellite altimetry – overview. In Bašić, T., editor, *Satellite Altimetry*, chapter 1. IntechOpen, Rijeka.
- Brown, G. (1977). The average impulse response of a rough surface and its applications. *IEEE Transactions on Antennas and Propagation*, 25(1):67–74.
- Chambers, D. (2007). 3.05 - gravimetric methods – spacecraft altimeter measurements. In Schubert, G., editor, *Treatise on Geophysics*, pages 123–161. Elsevier, Amsterdam.
- Corbella, I., Duffo, N., Vall-llossera, M., Camps, A., and Torres, F. (2004). The visibility function in interferometric aperture synthesis radiometry. *IEEE Transactions on Geoscience and Remote Sensing*, 42(8):1677–1682.
- Dawson, G., Landy, J., Tsamados, M., Komarov, A. S., Howell, S., Heorton, H., and Krumpen, T. (2022). A 10-year record of arctic summer sea ice freeboard from cryosat-2. *Remote Sensing of Environment*, 268:112744.
- Drinkwater, M. R., Francis, R., Ratier, G., and Wingham, D. J. (2004). The european space agency's earth explorer mission cryosat: measuring variability in the cryosphere. *Annals of Glaciology*, 39:313–320.
- Elachi, C. and Van Zyl, J. J. (2021). *Introduction to the physics and techniques*

- of remote sensing.* John Wiley & Sons.
- eoPortal (2025). Sea ice monitoring.
- ESA, M. (2013). Cryosat product handbook. *ESRIN, ESA and Mullard Space Science Laboratory/University College London, Frascati, Italy and Surrey, UK.*
- Fung, A. K. and Chen, K.-S. (2010). *Microwave scattering and emission models for users.* Artech house.
- Giles, K., Laxon, S., Wingham, D., Wallis, D., Krabill, W., Leuschen, C., McAdoo, D., Manizade, S., and Raney, R. (2007). Combined airborne laser and radar altimeter measurements over the fram strait in may 2002. *Remote Sensing of Environment*, 111(2):182–194. Remote Sensing of the Cryosphere Special Issue.
- Giles, K. A., Laxon, S. W., and Ridout, A. L. (2008). Circumpolar thinning of arctic sea ice following the 2007 record ice extent minimum. *Geophysical Research Letters*, 35(22).
- Haas, C. (1998). Evaluation of ship-based electromagnetic-inductive thickness measurements of summer sea-ice in the bellingshausen and amundsen seas, antarctica. *Cold Regions Science and Technology*, 27(1):1–16.
- Haas, C., Lobach, J., Hendricks, S., Rabenstein, L., and Pfaffling, A. (2009). Helicopter-borne measurements of sea ice thickness, using a small and lightweight, digital em system. *Journal of Applied Geophysics*, 67(3):234–241. Airborne Geophysics.
- Hendricks, S., Ricker, R., and Paul, S. (2021). Product user guide & algorithm specification: Awi cryosat-2 sea ice thickness (version 2.4).
- Hendricks, S., Steinhage, D., Helm, V., Birnbaum, G., Skou, N., Kristensen, S. S., Søbjærg, S. S., Gerland, S., Spreen, G., Bratrein, M., et al. (2015). Technical support for the 2014 smosice campaign in se svalbard-final report.
- Hersbach, H., Bell, B., Berrisford, P., Hirahara, S., Horányi, A., Muñoz-Sabater, J., Nicolas, J., Peubey, C., Radu, R., Schepers, D., Simmons, A., Soci, C., Abdalla, S., Abellan, X., Balsamo, G., Bechtold, P., Biavati, G., Bidlot, J., Bonavita, M., De Chiara, G., Dahlgren, P., Dee, D., Diamantakis, M., Dragani, R., Flemming, J., Forbes, R., Fuentes, M., Geer, A., Haimberger, L., Healy,

- S., Hogan, R. J., Hólm, E., Janisková, M., Keeley, S., Laloyaux, P., Lopez, P., Lupu, C., Radnoti, G., de Rosnay, P., Rozum, I., Vamborg, F., Villaume, S., and Thépaut, J.-N. (2020). The era5 global reanalysis. *Quarterly Journal of the Royal Meteorological Society*, 146(730):1999–2049.
- Hu, Z., Chen, D., Chen, X., Zhou, Q., Peng, Y., Li, J., and Sang, Y. (2022). Cchzdiso: A timely new assessment system for data quality or model performance from da dao zhi jian. *Geophysical Research Letters*, 49(23):e2022GL100681. e2022GL100681 2022GL100681.
- Huntemann, M., Heygster, G., Kaleschke, L., Krumpen, T., Mäkynen, M., and Drusch, M. (2014). Empirical sea ice thickness retrieval during the freeze-up period from smos high incident angle observations. *The Cryosphere*, 8(2):439–451.
- ICEYE (2020). Sar processing overview.
- Jaklin, K. (2025). Assessing the antarctic sea ice using satellite remote sensing - norce.
- Kaleschke, L., Maaß, N., Haas, C., Hendricks, S., Heygster, G., and Tonboe, R. T. (2010). A sea-ice thickness retrieval model for 1.4 ghz radiometry and application to airborne measurements over low salinity sea-ice. *The Cryosphere*, 4(4):583–592.
- Kaleschke, L., Tian-Kunze, X., Maaß, N., Mäkynen, M., and Drusch, M. (2012). Sea ice thickness retrieval from smos brightness temperatures during the arctic freeze-up period. *Geophysical Research Letters*, 39(5).
- King, J., Howell, S., Derksen, C., Rutter, N., Toose, P., Beckers, J. F., Haas, C., Kurtz, N., and Richter-Menge, J. (2015). Evaluation of operation icebridge quick-look snow depth estimates on sea ice. *Geophysical Research Letters*, 42(21):9302–9310.
- Knowles, K. W. (2001). *Points, Pixels, Grids and Cells: A Mapping and Gridding Primer*. National Snow and Ice Data Center.
- Krishfield, R. and Proshutinsky, A. (2006). Bgos uls data processing procedure.
- Kurtz, N. T., Farrell, S. L., Koenig, L. S., Studinger, M., Harbeck, J. P., et al. (2012). A sea-ice lead detection algorithm for use with high-resolution

- airborne visible imagery. *IEEE Transactions on Geoscience and Remote Sensing*, 51(1):38–56.
- Kurtz, N. T., Farrell, S. L., Studinger, M., Galin, N., Harbeck, J. P., Lindsay, R., Onana, V. D., Panzer, B., and Sonntag, J. G. (2013). Sea ice thickness, freeboard, and snow depth products from operation icebridge airborne data. *The Cryosphere*, 7(4):1035–1056.
- Kurtz, N. T., Galin, N., and Studinger, M. (2014). An improved cryosat-2 sea ice freeboard retrieval algorithm through the use of waveform fitting. *The Cryosphere*, 8(4):1217–1237.
- Kwok, R., Kurtz, N. T., Brucker, L., Ivanoff, A., Newman, T., Farrell, S. L., King, J., Howell, S., Webster, M. A., Paden, J., Leuschen, C., MacGregor, J. A., Richter-Menge, J., Harbeck, J., and Tschudi, M. (2017). Intercomparison of snow depth retrievals over arctic sea ice from radar data acquired by operation icebridge. *The Cryosphere*, 11(6):2571–2593.
- Landy, J. C., Petty, A. A., Tsamados, M., and Stroeve, J. C. (2020). Sea ice roughness overlooked as a key source of uncertainty in cryosat-2 ice freeboard retrievals. *Journal of Geophysical Research: Oceans*, 125(5):e2019JC015820. e2019JC015820 2019JC015820.
- Landy, J. C., Tsamados, M., and Scharien, R. K. (2019). A facet-based numerical model for simulating sar altimeter echoes from heterogeneous sea ice surfaces. *IEEE Transactions on Geoscience and Remote Sensing*, 57(7):4164–4180.
- Laxon, S. W., Giles, K. A., Ridout, A. L., Wingham, D. J., Willatt, R., Cullen, R., Kwok, R., Schweiger, A., Zhang, J., Haas, C., Hendricks, S., Krishfield, R., Kurtz, N., Farrell, S., and Davidson, M. (2013). Cryosat-2 estimates of arctic sea ice thickness and volume. *Geophysical Research Letters*, 40(4):732–737.
- Lee, J.-G. and Ham, Y.-G. (2022). Satellite-based data assimilation system for the initialization of arctic sea ice concentration and thickness using cice5. *Frontiers in Climate*, Volume 4 - 2022.
- Lee, J.-G. and Ham, Y.-G. (2023). Impact of satellite thickness data assimilation on bias reduction in arctic sea ice concentration. *npj Climate and Atmospheric Science*, 6(1):73.
- Lemmens, M. (2015). Operation icebridge. *GIM INTERNATIONAL-THE WORLD-*

- WIDE MAGAZINE FOR GEOMATICS, 29(2):27–31.
- Liston, G. E., Itkin, P., Stroeve, J., Tschudi, M., Stewart, J. S., Pedersen, S. H., Reinking, A. K., and Elder, K. (2020). A lagrangian snow-evolution system for sea-ice applications (snowmodel-lg): Part i—model description. *Journal of Geophysical Research: Oceans*, 125(10):e2019JCo15913. e2019JCo15913 2019JCo15913.
- MacGregor, J. A., Boisvert, L. N., Medley, B., Petty, A. A., Harbeck, J. P., Bell, R. E., Blair, J. B., Blanchard-Wrigglesworth, E., Buckley, E. M., Christoffersen, M. S., Cochran, J. R., Csathó, B. M., De Marco, E. L., Dominguez, R. T., Fahnestock, M. A., Farrell, S. L., Gogineni, S. P., Greenbaum, J. S., Hansen, C. M., Hofton, M. A., Holt, J. W., Jezek, K. C., Koenig, L. S., Kurtz, N. T., Kwok, R., Larsen, C. F., Leuschen, C. J., Locke, C. D., Manizade, S. S., Martin, S., Neumann, T. A., Nowicki, S. M., Paden, J. D., Richter-Menge, J. A., Rignot, E. J., Rodríguez-Morales, F., Siegfried, M. R., Smith, B. E., Sonntag, J. G., Studinger, M., Tinto, K. J., Truffer, M., Wagner, T. P., Woods, J. E., Young, D. A., and Yungel, J. K. (2021). The scientific legacy of nasa's operation icebridge. *Reviews of Geophysics*, 59(2):e2020RG000712. e2020RG000712 2020RG000712.
- Martín-Neira, M., Oliva, R., Corbella, I., Torres, F., Duffo, N., Durán, I., Kainulainen, J., Closa, J., Zurita, A., Cabot, F., Khazaal, A., Anterrieu, E., Barbosa, J., Lopes, G., Tenerelli, J., Díez-García, R., Fauste, J., Martín-Porqueras, F., González-Gambau, V., Turiel, A., Delwart, S., Crapolicchio, R., and Suess, M. (2016). Smos instrument performance and calibration after six years in orbit. *Remote Sensing of Environment*, 180:19–39. Special Issue: ESA's Soil Moisture and Ocean Salinity Mission - Achievements and Applications.
- Maykut, G. A. (1978). Energy exchange over young sea ice in the central arctic. *Journal of Geophysical Research: Oceans*, 83(C7):3646–3658.
- McCarty, W., Coy, L., Gelaro, R., Huang, A., Merkova, D., Smith, E. B., Sienkiewicz, M., and Wargan, K. (2016). Merra-2 input observations: Summary and assessment. *NASA Tech. Rep. NASA/TM-2016-104606*, 46:64.
- McMullan, K. D., Brown, M. A., Martin-Neira, M., Rits, W., Ekholm, S., Marti, J., and Lemanczyk, J. (2008). Smos: The payload. *IEEE Transactions on Geoscience and Remote Sensing*, 46(3):594–605.
- Mecklenburg, S., Drusch, M., Kaleschke, L., Rodriguez-Fernandez, N., Reul, N., Kerr, Y., Font, J., Martin-Neira, M., Oliva, R., Daganzo-Eusebio, E., Grant,

- J., Sabia, R., Macelloni, G., Rautiainen, K., Fauste, J., de Rosnay, P., Munoz-Sabater, J., Verhoest, N., Lievens, H., Delwart, S., Crapolicchio, R., de la Fuente, A., and Kornberg, M. (2016). Esa's soil moisture and ocean salinity mission: From science to operational applications. *Remote Sensing of Environment*, 180:3–18. Special Issue: ESA's Soil Moisture and Ocean Salinity Mission - Achievements and Applications.
- Mignac, D., Martin, M., Fiedler, E., Blockley, E., and Fournier, N. (2022). Improving the met office's forecast ocean assimilation model (foam) with the assimilation of satellite-derived sea-ice thickness data from cryosat-2 and smos in the arctic. *Quarterly Journal of the Royal Meteorological Society*, 148(744):1144–1167.
- Mu, L., Nerger, L., Tang, Q., Loza, S. N., Sidorenko, D., Wang, Q., Semmler, T., Zampieri, L., Losch, M., and Goessling, H. F. (2020). Toward a data assimilation system for seamless sea ice prediction based on the awi climate model. *Journal of Advances in Modeling Earth Systems*, 12(4):e2019MS001937. e2019MS001937 10.1029/2019MS001937.
- Müller, F. L., Paul, S., Hendricks, S., and Dettmering, D. (2023). Monitoring arctic thin ice: a comparison between cryosat-2 sar altimetry data and modis thermal-infrared imagery. *The Cryosphere*, 17(2):809–825.
- Mätzler, C. and Wiesmann, A. (1999). Extension of the microwave emission model of layered snowpacks to coarse-grained snow. *Remote Sensing of Environment*, 70(3):317–325.
- NASA (2021). Remote sensing | nasa earthdata. <https://www.earthdata.nasa.gov/learn/earth-observation-data-basics/remote-sensing>. [Accessed 06-05-2025].
- NISAR (2020). Sar overview.
- Odh, A. (2024). Antarctic ice shelf response to ocean tides and atmospheric pressure variations using satellite interferometry. Master's thesis, UiT The Arctic University of Norway.
- Papasaika-Hanusch, C. (2012). *Fusion of digital elevation models*. PhD thesis, ETH Zurich.
- Parrinello, T., Shepherd, A., Bouffard, J., Badessi, S., Casal, T., Davidson, M.,

- Fornari, M., Maestroni, E., and Scagliola, M. (2018). Cryosat: Esa's ice mission – eight years in space. *Advances in Space Research*, 62(6):1178–1190. The CryoSat Satellite Altimetry Mission: Eight Years of Scientific Exploitation.
- Polyak, L., Alley, R. B., Andrews, J. T., Brigham-Grette, J., Cronin, T. M., Darby, D. A., Dyke, A. S., Fitzpatrick, J. J., Funder, S., Holland, M., Jennings, A. E., Miller, G. H., O'Regan, M., Savelle, J., Serreze, M., St. John, K., White, J. W., and Wolff, E. (2010). History of sea ice in the arctic. *Quaternary Science Reviews*, 29(15):1757–1778. Special Theme: Arctic Palaeoclimate Synthesis (PP. 1674-1790).
- Quartly, G. D., Rinne, E., Passaro, M., Andersen, O. B., Dinardo, S., Fleury, S., Guillot, A., Hendricks, S., Kurekin, A. A., Müller, F. L., Ricker, R., Skourup, H., and Tsamados, M. (2019). Retrieving sea level and freeboard in the arctic: A review of current radar altimetry methodologies and future perspectives. *Remote Sensing*, 11(7).
- Quegan, S. and Atkinson, P. (2008). Radar remote sensing. *Geoinformatics*, 1:1–26.
- Rantanen, M., Karpechko, A. Y., Lipponen, A., Nordling, K., Hyvärinen, O., Ruosteenoja, K., Vihma, T., and Laaksonen, A. (2022). The arctic has warmed nearly four times faster than the globe since 1979. *Communications earth & environment*, 3(1):168.
- Ricker, R., Hendricks, S., Helm, V., Skourup, H., and Davidson, M. (2014). Sensitivity of cryosat-2 arctic sea-ice volume trends on radarwaveform interpretation. *Cryosphere Discuss*, 8:1831–1871.
- Ricker, R., Hendricks, S., Kaleschke, L., Tian-Kunze, X., King, J., and Haas, C. (2017). A weekly arctic sea-ice thickness data record from merged cryosat-2 and smos satellite data. *The Cryosphere*, 11(4):1607–1623.
- Rosmorduc, V., Benveniste, J., Bronner, E., Dinardo, S., Lauret, O., Maheu, C., Milagro-Pérez, M., and Picot, N. (2011). *Radar Altimetry Tutorial*.
- Rothrock, D. A., Percival, D. B., and Wensnahan, M. (2008). The decline in arctic sea-ice thickness: Separating the spatial, annual, and interannual variability in a quarter century of submarine data. *Journal of Geophysical Research: Oceans*, 113(C5).

- Sallila, H., Farrell, S. L., McCurry, J., and Rinne, E. (2019). Assessment of contemporary satellite sea ice thickness products for arctic sea ice. *The Cryosphere*, 13(4):1187–1213.
- Sandberg Sørensen, L., Simonsen, S. B., Forsberg, R., Khvorostovsky, K., Meister, R., and Engdahl, M. E. (2018). 25 years of elevation changes of the greenland ice sheet from ers, envisat, and cryosat-2 radar altimetry. *Earth and Planetary Science Letters*, 495:234–241.
- Sandven, S. and Johannessen, O. M. (2006). Sea ice monitoring by remote sensing. The American Society for Photogrammetry & Remote Sensing.
- Sandven, S., Spreen, G., Heygster, G., Girard-Ardhuin, F., Farrell, S. L., Dierking, W., and Allard, R. A. (2023). Sea ice remote sensing—recent developments in methods and climate data sets. *Surveys in Geophysics*, 44(5):1653–1689.
- SentiWiki (2025). Altimetry processing.
- Shi, H., Tonboe, R., Lee, S.-M., Dybkjær, G., Sohn, B.-J., Singha, S., and Baordo, F. (2024). A simple and robust cryosat-2 radar freeboard correction method dedicated to tfmra50 for the arctic winter snow depth and sea ice thickness retrieval. *Earth and Space Science*, 11(10):e2024EA003715.
- Sievers, I., Skourup, H., and Rasmussen, T. A. S. (2024). Impact assessment of snow thickness, sea ice density and water density in cryosat-2-derived sea ice thickness. *The Cryosphere*, 18(12):5985–6004.
- Tian-Kunze, L., Tian-Kunze, X., and Kaleschke (2023). Smos sea ice thickness product description document (pdd). *Issue*.
- Tian-Kunze, X., Kaleschke, L., Maaß, N., Mäkynen, M., Serra, N., Drusch, M., and Krumpen, T. (2014). Smos-derived thin sea ice thickness: algorithm baseline, product specifications and initial verification. *The Cryosphere*, 8(3):997–1018.
- Tilling, R. L., Ridout, A., and Shepherd, A. (2016). Near-real-time arctic sea ice thickness and volume from cryosat-2. *The Cryosphere*, 10(5):2003–2012.
- Tilling, R. L., Ridout, A., and Shepherd, A. (2018). Estimating arctic sea ice thickness and volume using cryosat-2 radar altimeter data. *Advances in Space Research*, 62(6):1203–1225. The CryoSat Satellite Altimetry Mission:

- Eight Years of Scientific Exploitation.
- Vihma, T. (2014). Effects of arctic sea ice decline on weather and climate: A review. *Surveys in Geophysics*, 35:1175–1214.
- Wang, X., Key, J., Kwok, R., and Zhang, J. (2016). Comparison of arctic sea ice thickness from satellites, aircraft, and piomas data. *Remote Sensing*, 8(9).
- Warren, S. G., Rigor, I. G., Untersteiner, N., Radionov, V. F., Bryazgin, N. N., Aleksandrov, Y. I., and Colony, R. (1999). Snow depth on arctic sea ice. *Journal of Climate*, 12(6):1814–1829.
- Wingham, D., Francis, C., Baker, S., Bouzinac, C., Brockley, D., Cullen, R., de Chateau-Thierry, P., Laxon, S., Mallow, U., Mavrocordatos, C., Phalippou, L., Ratier, G., Rey, L., Rostan, F., Viau, P., and Wallis, D. (2006). Cryosat: A mission to determine the fluctuations in earth's land and marine ice fields. *Advances in Space Research*, 37(4):841–871. Natural Hazards and Oceanographic Processes from Satellite Data.
- WMO (2025). Sea ice.
- Zhang, Y., Li, G., Li, H., Chen, C., Shao, W., Zhou, Y., and Wang, D. (2024). A spatiotemporal comparison and assessment of multisource satellite derived sea ice thickness in the arctic thinner ice region. *IEEE Journal of Selected Topics in Applied Earth Observations and Remote Sensing*, 17:8710–8723.
- Zhou, H., Chen, Y., Hyppä, J., and Li, S. (2017). An overview of the laser ranging method of space laser altimeter. *Infrared Physics Technology*, 86:147–158.
- Zygmuntowska, M. (2014). Arctic sea ice altimetry-advances and current uncertainties.

Appendix A: Complete Analysis Results and Supporting Data

A.1 Comparison of CryoSat Products Against SMOS AWI

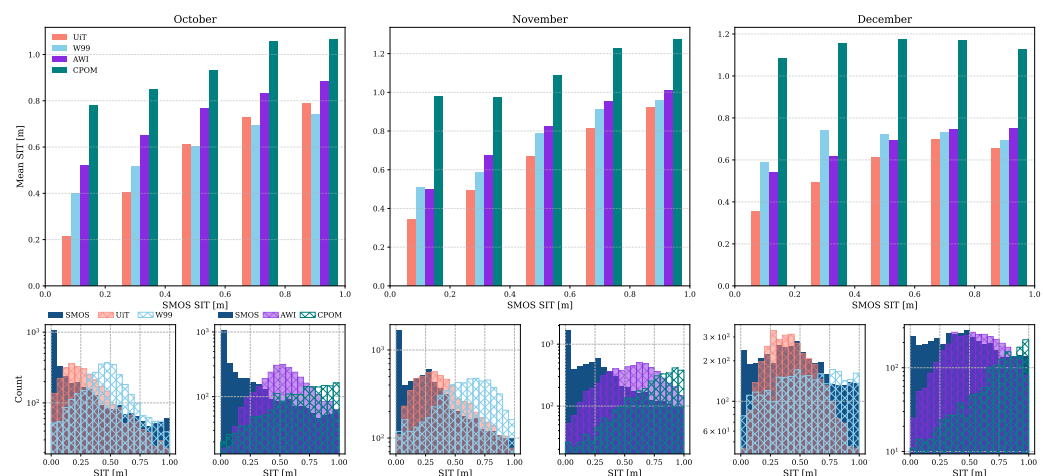


Figure A.1: Mean sea ice thickness (SIT) bar plot and corresponding distribution plots comparing CryoSat products with the SMOS AWI product. Comparing all months, October, November, and December.

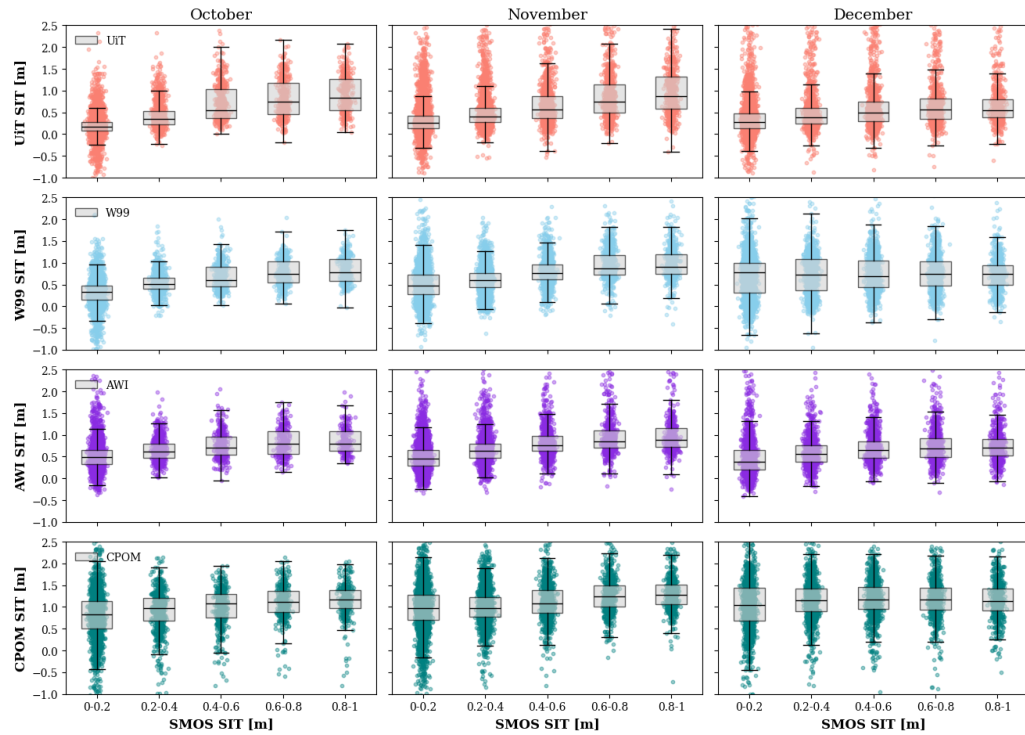


Figure A.2: Box scatter plot illustrating CryoSat product sea ice thickness (SIT) estimates as a function of SMOS SIT values, grouped into corresponding bins. Comparing all months, October, November, and December.

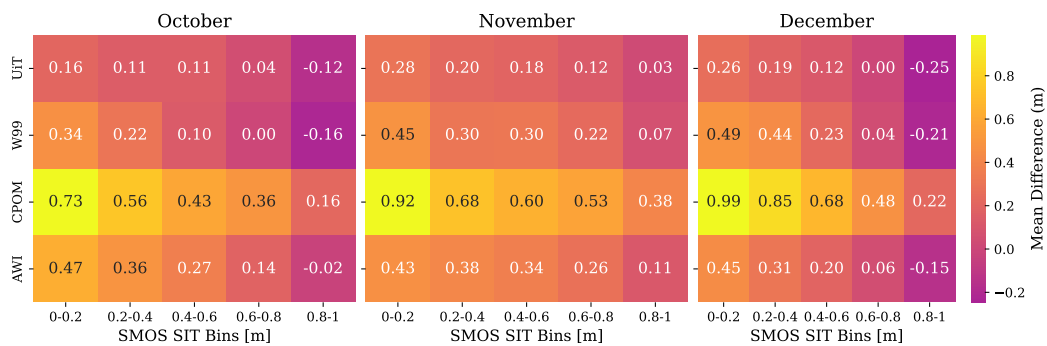


Figure A.3: Heat map displaying the mean sea ice thickness (SIT) differences between each CryoSat product. Comparing all months, October, November, and December.

Table A.1: Statistical metrics for CryoSat products against the SMOS AWI, presented by analysis month and categorized into distinct sea ice thickness intervals as [0.0 – 0.2, 0.2 – 0.4, 0.4 – 0.6, 0.6 – 0.8, 0.8 – 1.0] in meters.

Product	October				
	Bias	CC	RMSE	Total Bias	Total RMSE
UiT	[0.158, 0.113, 0.112, 0.036, -0.116]	[0.233, 0.142, 0.124, 0.148, 0.070]	[0.273, 0.301, 0.365, 0.394, 0.425]	0.061	0.352
W99	[0.342, 0.222, 0.103, 0.001, -0.164]	[0.158, 0.060, 0.072, 0.155, 0.041]	[0.429, 0.296, 0.269, 0.270, 0.312]	0.101	0.315
AWI	[0.465, 0.358, 0.268, 0.139, -0.020]	[0.189, 0.059, 0.100, 0.164, 0.019]	[0.532, 0.442, 0.405, 0.355, 0.364]	0.242	0.420
CPOM	[0.726, 0.555, 0.434, 0.364, 0.160]	[0.021, 0.018, 0.112, 0.027, 0.026]	[0.922, 0.775, 0.644, 0.586, 0.453]	0.448	0.676
November					
UiT	[0.281, 0.203, 0.183, 0.123, 0.028]	[0.25, 0.184, 0.078, 0.153, 0.056]	[0.397, 0.395, 0.446, 0.446, 0.489]	0.164	0.435
W99	[0.446, 0.295, 0.3, 0.219, 0.066]	[0.08, 0.179, 0.144, 0.103, 0.032]	[0.537, 0.414, 0.411, 0.371, 0.349]	0.265	0.416
AWI	[0.434, 0.382, 0.338, 0.262, 0.113]	[0.157, 0.18, 0.09, 0.105, 0.039]	[0.526, 0.526, 0.485, 0.492, 0.470]	0.306	0.500
CPOM	[0.918, 0.682, 0.601, 0.534, 0.377]	[0.039, 0.127, 0.041, 0.076, -0.032]	[1.097, 0.801, 0.722, 0.647, 0.533]	0.622	0.760
December					
UiT	[0.257, 0.187, 0.12, 0.005, -0.246]	[0.177, 0.043, 0.035, -0.002, 0.024]	[0.376, 0.485, 0.526, 0.791, 0.525]	0.064	0.541
W99	[0.49, 0.437, 0.228, 0.039, -0.210]	[0.022, 0.094, -0.029, -0.055, 0.067]	[0.666, 0.655, 0.460, 0.767, 0.415]	0.197	0.592
AWI	[0.445, 0.312, 0.200, 0.056, -0.152]	[0.063, 0.069, 0.010, 0.010, -0.005]	[0.859, 0.617, 0.399, 0.382, 0.415]	0.172	0.535
CPOM	[0.988, 0.851, 0.678, 0.476, 0.223]	[0.056, 0.037, -0.065, 0.07, 0.062]	[1.223, 1.023, 0.840, 0.682, 0.482]	0.643	0.850

A.2 Validation Against OIB Airborne Observations

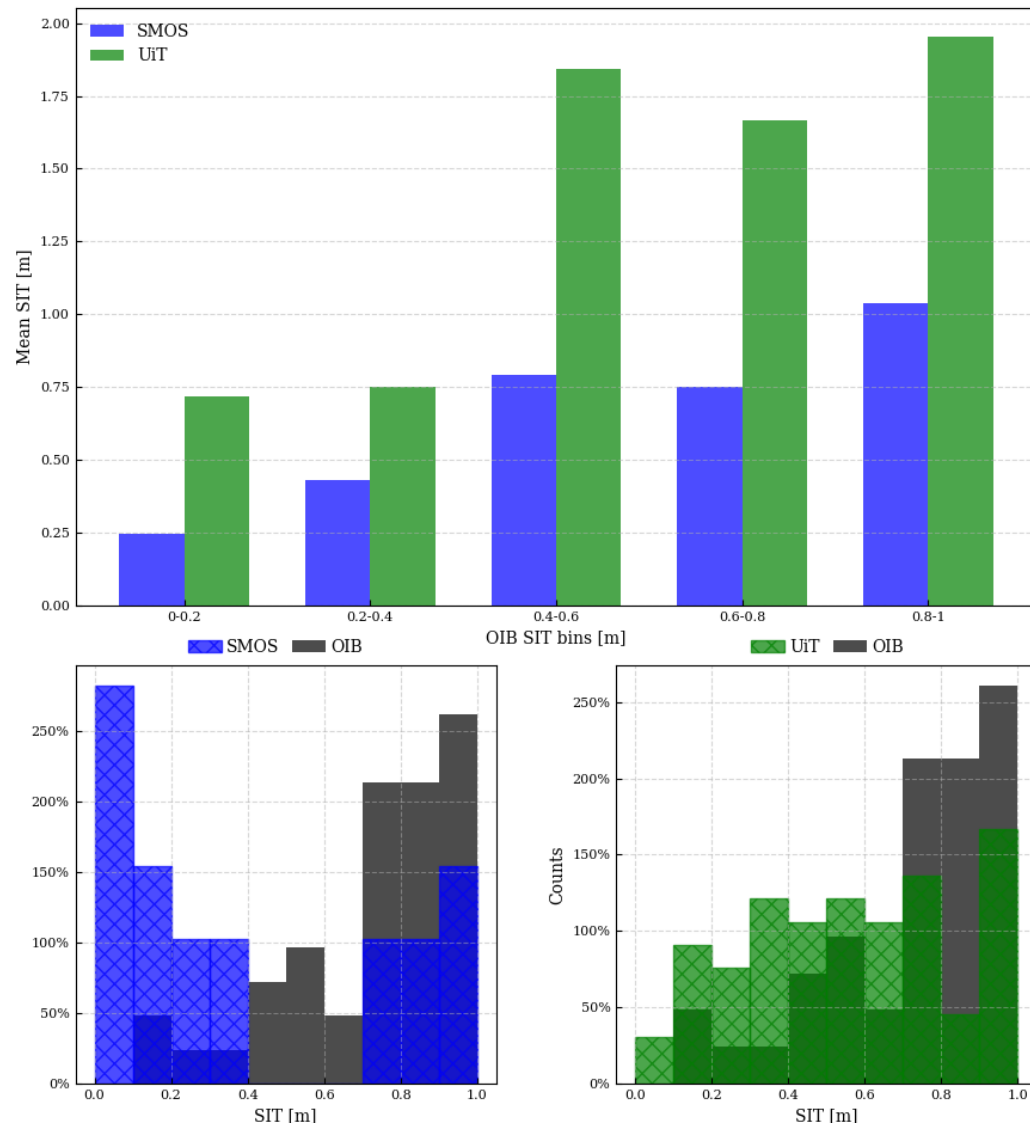


Figure A.4: Mean sea ice thickness (SIT) bar plot and corresponding distribution plot comparing CryoSat UiT and SMOS AWI products with the OIB measurements. Without the SIT range constrained to 1 m for all datasets, which is applied to the corresponding figure in Section 6.2.

Table A.2: Statistical metrics for CryoSat UiT and SMOS AWI against the OIB SIT measurements, categorized into distinct sea ice thickness intervals as [0.0 – 0.2, 0.2 – 0.4, 0.4 – 0.6, 0.6 – 0.8, 0.8 – 1.0] in meters.

Product	Thickness Range [m]	Bias	RMSE	CC	DISO
UiT	0.0-0.2	0.323	0.384	-0.728	2.233
	0.2-0.4	0.132	0.269	-0.420	1.737
	0.4-0.6	0.013	0.254	0.549	1.097
	0.6-0.8	-0.253	0.354	-0.301	1.641
	0.8-1.0	-0.352	0.442	-0.327	1.662
SMOS	0.0-0.2	0.038	0.094	-1.000	2.000
	0.2-0.4	-0.004	0.369	-1.000	2.236
	0.4-0.6	-0.111	0.289	0.998	1.000
	0.6-0.8	-0.563	0.618	-0.842	2.096
	0.8-1.0	-0.730	0.780	0.350	1.192

A.3 Validation Against BGEP Mooring Data

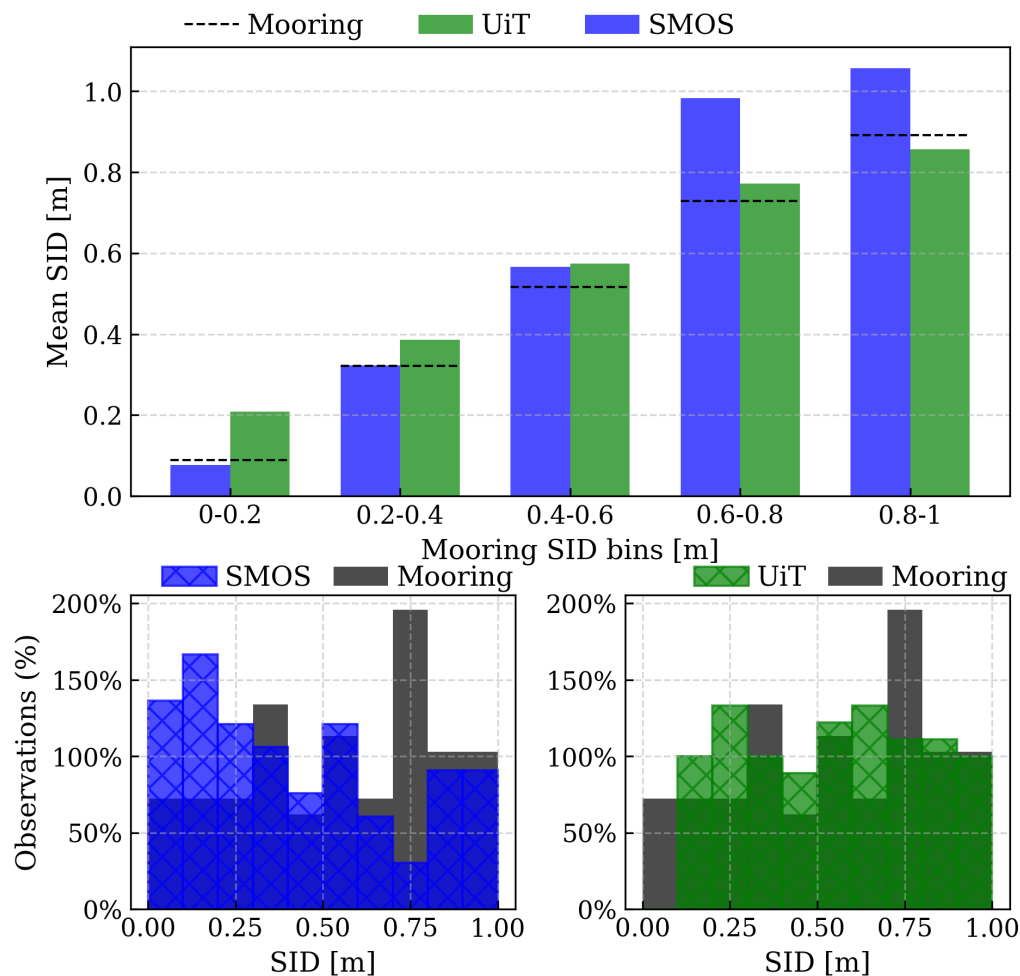


Figure A.5: Mean sea ice draft (SID) bar plot and corresponding distribution plot comparing CryoSat UiT and SMOS AWI products with the BGEP mooring measurements. Without the SID range constrained to 1 m for all datasets, which is applied to the corresponding figure in Section 6.3.

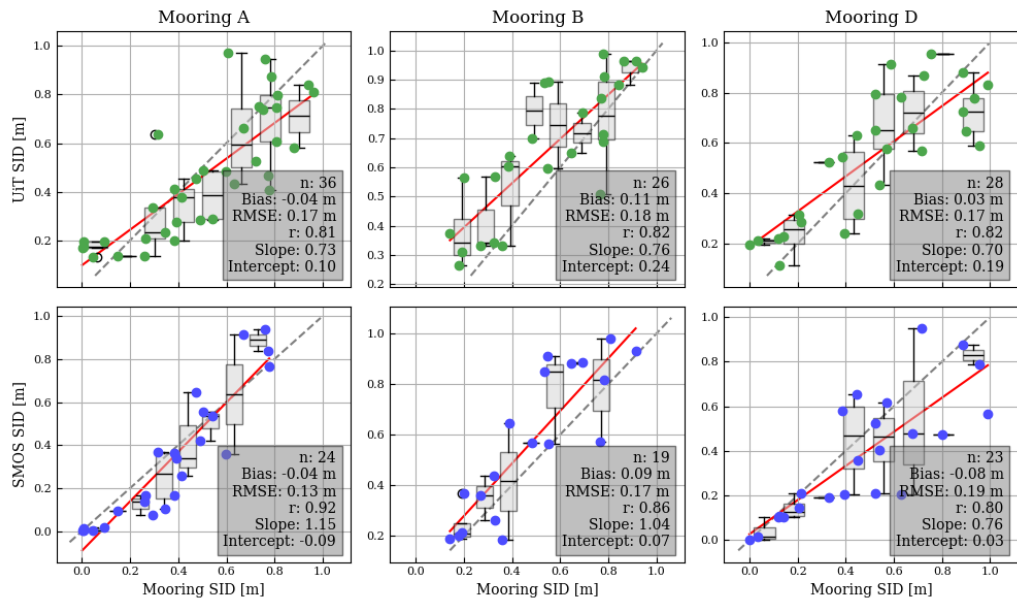


Figure A.6: Pair scatter plot of raw sea ice draft (SID) estimates from CryoSat UIIT and SMOS AWI products as a function of mooring A, B, and D SID observations

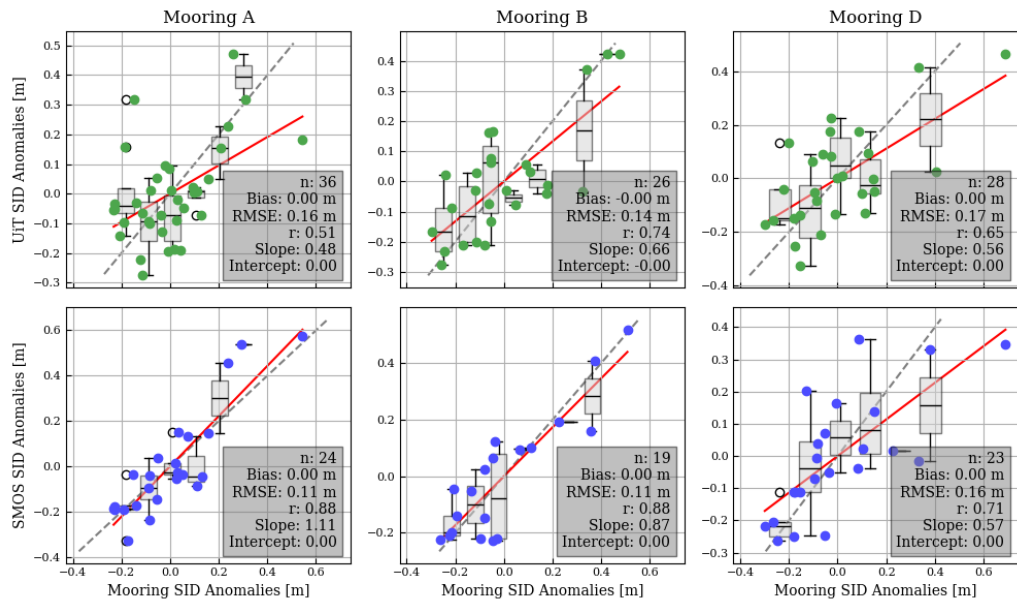


Figure A.7: Pair scatter plot of SID seasonal anomalies estimates from CryoSat UIIT and SMOS AWI products as a function of mooring A, B, and D SID observations

Table A.3: Statistical metrics for CryoSat UiT and SMOS AWI against the BGEP SID measurements, categorized into distinct sea ice thickness intervals as [0.0 – 0.2, 0.2 – 0.4, 0.4 – 0.6, 0.6 – 0.8, 0.8 – 1.0] in meters.

Product	Thickness Range [m]	Bias	RMSE	CC	DISO
UiT	0.0-0.2	0.120	0.139	0.470	1.510
	0.2-0.4	0.065	0.173	0.175	1.637
	0.4-0.6	0.058	0.199	0.403	1.535
	0.6-0.8	-0.001	0.180	0.086	0.914
	0.8-1.0	-0.108	0.168	0.154	1.310
SMOS	0.0-0.2	-0.012	0.033	0.915	0.085
	0.2-0.4	-0.038	0.150	0.330	0.670
	0.4-0.6	0.015	0.181	0.228	0.772
	0.6-0.8	0.032	0.213	0.364	1.551
	0.8-1.0	-0.124	0.240	-0.088	1.478

A.4 Validation Against SMOSice Campaign Measurements

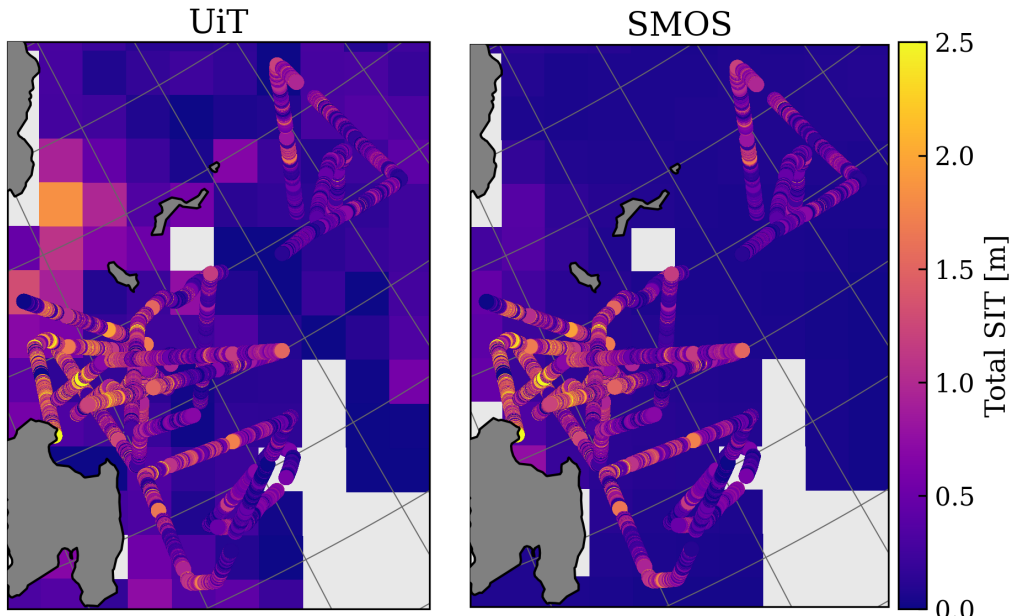


Figure A.8: Map showing total sea ice thickness (tSIT) unresampled estimates from CryoSat UiT (left figure) and SMOS AWI (right figure) products, with overlaid HEM tSIT estimates

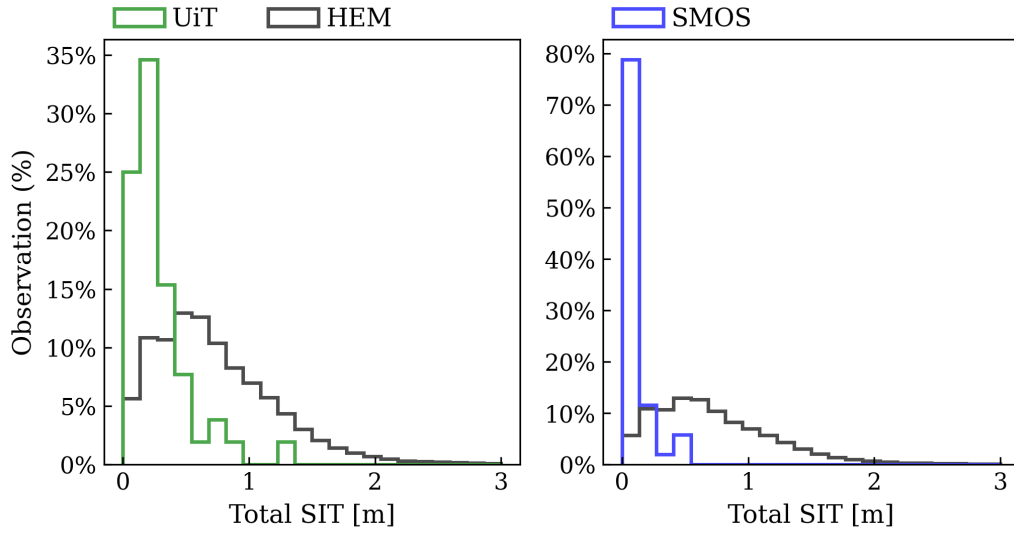


Figure A.9: Distribution of total sea ice thickness (tSIT) derived from unresampled HEM measurements, compared with corresponding tSIT distributions from the CryoSat UiT and SMOS AWI products.

Table A.4: Statistical metrics for CryoSat UiT and SMOS AWI against the HEM tSIT measurements, categorized into distinct sea ice thickness intervals as [0.0 – 0.2, 0.2 – 0.4, 0.4 – 0.6, 0.6 – 0.8, 0.8 – 1.0] in meters.

Product	Thickness Range [m]	Bias	RMSE	CC	DISO
UiT	0.0-0.2	-0.014	0.014	nan	nan
	0.2-0.4	-0.154	0.198	0.971	1.000
	0.4-0.6	-0.275	0.332	0.011	1.406
	0.6-0.8	-0.502	0.512	0.229	1.263
	0.8-1.0	-0.702	0.709	-0.306	1.645
SMOS	0.0-0.2	-0.099	0.099	nan	nan
	0.2-0.4	-0.284	0.286	0.061	1.372
	0.4-0.6	-0.410	0.413	0.566	1.090
	0.6-0.8	-0.604	0.606	0.506	1.115
	0.8-1.0	-0.821	0.824	-0.364	1.691

Table A.5: Statistical metrics for CryoSat UiT against the ALS tFB measurements, categorized into distinct sea ice thickness intervals as [0.0 – 0.2, 0.2 – 0.4, 0.4 – 0.6, 0.6 – 0.8, 0.8 – 1.0] in meters.

Product	Thickness Range [m]	Bias	RMSE	CC	DISO	Mean UiT	Mean ALS
UiT	0.0-0.2	0.007	0.055	0.137	0.909	0.082	0.075
	0.2-0.4	0.238	0.251	-0.295	3.260	0.292	0.054
	0.4-0.6	0.435	0.440	0.015	3.375	0.476	0.040
	0.6-0.8	0.662	0.663	0.231	8.517	0.695	0.033
	0.8-1.0	0.856	0.857	0.726	7.898	0.897	0.040

